



Fernanda Cristinna Alonso dos Santos

**Behavior of Textile Reinforced
Concrete (TRC) Slender Columns
Subject to Compression**

Dissertação de Mestrado

Dissertation presented to the Programa de Pós-graduação em Engenharia Civil of PUC-Rio in partial fulfillment of the requirements for the degree of Mestre em Engenharia Civil.

Advisor: Prof. Daniel Carlos Taissum Cardoso

Rio de Janeiro
February 2018



Fernanda Cristinna Alonso dos Santos

**Behavior of Textile Reinforced
Concrete (TRC) Slender Columns
Subject to Compression**

Dissertation presented to the Programa de Pós-graduação em Engenharia Civil of PUC-Rio in partial fulfillment of the requirements for the degree of Mestre em Engenharia Civil. Approved by the undersigned Examination Committee.

Prof. Daniel Carlos Taissum Cardoso

Advisor

Departamento de Engenharia Civil e Ambiental – PUC-Rio

Prof. Flávio de Andrade Silva

Departamento de Engenharia Civil e Ambiental – PUC-Rio

Prof^a. Lídia da Conceição Domingues Shehata

Universidade Federal Fluminense - UFF

Prof. Márcio da Silveira Carvalho

Vice Dean of Graduate Studies

Centro Técnico Científico – PUC-Rio

Rio de Janeiro, February 8th, 2018.

All rights reserved.

Fernanda Cristinna Alonso dos Santos

Bachelor in civil engineering at Universidade Federal Fluminense, in 2013. Worked with reinforced concrete structural designs and management of projects. Her area of interest encompasses the instability of structures, composite materials and experimental researches.

Bibliographic data

dos Santos, Fernanda Cristinna Alonso

Behavior of Textile Reinforced Concrete (TRC) Slender Columns Subject to Compression / Fernanda Cristinna Alonso dos Santos ; advisor: Daniel Carlos Taissum Cardoso – 2018.

122 f. : il. color. ; 30 cm

Dissertação (Mestrado) – Pontifícia Universidade Católica do Rio de Janeiro, Departamento de Engenharia Civil, 2018.

Inclui bibliografia

1. Engenharia civil – Teses. 2. Concreto Têxtil (CT). 3. Pilares. 4. Flambagem Global. I. Cardoso, Daniel Carlos Taissum. II. Pontifícia Universidade Católica do Rio de Janeiro. Departamento de Engenharia Civil. III. Título.

CDD: 624

Acknowledgment

To God, for giving me the strength to be able to carry out this work.

To CAPES, for the financial support.

To all the teachers and staff of the Department, for all the knowledge and help in the past two years.

To the staff of the Structures and Materials Laboratory (LEM/DEC) at PUC-Rio, who assisted me in the crucial moments of the experimental program: Marques, José Nilson, Rogério, Bruno, Carlos and especially Euclides. Thank you very much, I would not have done it without you.

To my advisor, Prof. Daniel Cardoso. Thank you for sharing your knowledge, for the daily motivation and especially for believing in me. Without your guidance, this work would not have been possible and I am really grateful to you.

To my wonderful friends, the old ones and all the friends I made during this journey on PUC. I thank you for understanding my absences, for helping me to face and overcome difficulties and making these days so much easier.

To my dear family, especially my parents Guillermina e Fernando, who celebrated and encouraged me every step of the way. Thank you for believing in me. All that I am today I owe to you.

Abstract

dos Santos, Fernanda Cristinna Alonso; Cardoso, Daniel Carlos Taissum (Advisor). **Behavior of Textile Reinforced Concrete (TRC) Slender Columns Subject to Compression.** Rio de Janeiro, 2018. 122 p. Dissertação de Mestrado – Departamento de Engenharia Civil e Ambiental. Pontifícia Universidade Católica do Rio de Janeiro.

This work aims to investigate the performance of Textile Reinforced Concrete (TRC) columns subject to compression. An experimental program including material characterization, four-point bending tests on plates and compression tests on rectangular and I-section columns with different lengths and end conditions was conducted. A one-degree of freedom axial force-moment-curvature model is proposed and the results using experimentally determined material properties are compared to those obtained for four-point bending tests, for validation. Load vs lateral deflection curves obtained experimentally are reported along with maximum loads and failure modes and the numerical model is used to determine imperfections as well as to support the analysis of results. The influences of imperfections and mechanical properties of concrete in the actual column behavior are discussed and it is shown that the tensile strength of concrete has a strong influence in the peak load of columns with greater slenderness. Erosions of capacity up to 53.6% were observed with respect to those expected for a perfect column and it is shown that the model can be accurately used for strength prediction. Concerning the textile, it is shown that the reinforcement contribution should not be neglected for members in compression.

Keywords

Textile Reinforced Concrete (TRC); columns; global buckling.

Resumo

dos Santos, Fernanda Cristinna Alonso; Cardoso, Daniel Carlos Taissum (Orientador). **Comportamento de Pilares Esbeltos de Concreto Têxtil (CT) Sujeitos a Compressão**. Rio de Janeiro, 2018. 122 p. Dissertação de Mestrado – Departamento de Engenharia Civil e Ambiental. Pontifícia Universidade Católica do Rio de Janeiro.

Este trabalho tem como objetivo investigar o desempenho de pilares de Concreto Têxtil (CT) sujeitos a compressão. Um programa experimental foi conduzido incluindo caracterização do material, ensaios de flexão de quatro pontos em placas e ensaios de compressão em pilares retangulares e de seção I com diferentes comprimentos e condições de contorno. Um modelo normal-momento-curvatura de um grau de liberdade foi proposto e seus resultados, utilizando propriedades do material determinadas experimentalmente, são comparados aos obtidos para os ensaios de flexão de quatro pontos, para validação. Curvas força-deslocamento obtidas experimentalmente são apresentadas juntamente com as cargas máximas e modos de falha e o modelo numérico é usado para determinar imperfeições, bem como para dar suporte à análise de resultados. As influências de imperfeições e propriedades mecânicas do concreto no comportamento do pilar real são discutidas e é mostrado que a resistência à tração do concreto tem uma forte influência na carga de pico de pilares com maior esbeltez. Foram observadas reduções de capacidade de até 53,6% em relação às esperadas para um pilar perfeito e é mostrado que o modelo pode ser usado com precisão para a previsão de carga. No que diz respeito ao tecido, é demonstrado que a contribuição do reforço em membros comprimidos não deve ser desconsiderada.

Palavras-chave

Concreto Têxtil (CT); pilares; flambagem global.

Table of Contents

1. Introduction	18
1.1. Overview	18
1.2. Motivation of Present Study	20
1.3. Objectives	20
1.4. Organization of the dissertation.....	21
2. Literature Review	22
2.1. Textile Reinforced Concrete (TRC)	22
2.1.1. Overview.....	22
2.1.2. Bond behavior.....	26
2.1.3. Mechanical behavior.....	26
2.2. Columns Behavior	28
2.2.1. Overview.....	28
2.2.2. Perfect Members	29
2.2.3. Real Columns	33
2.2.4. Numerical Models	39
2.2.5. Behavior of Reinforced Concrete Columns.....	44
3. Experimental Program	47
3.1. Overview	47
3.2. Material Description.....	47
3.3. Molding Processes	50
3.4. Material Characterization	54
3.4.1. Carbon Yarn Uniaxial Tension Test.....	54

3.4.2.	Matrix Compression Test.....	55
3.4.3.	Combined Loading Compression Test.....	56
3.4.4.	Four-point Bending Tests.....	57
3.5.	I-Section Column Tests	58
3.6.	Rectangular Column Tests	61
4.	Results Analysis	63
4.1.	Overview	63
4.2.	Material Characterization	63
4.2.1.	Carbon Yarn Uniaxial Tension Test.....	63
4.2.2.	Matrix Compression Test.....	64
4.2.3.	Combined Loading Compression Test.....	65
4.2.4.	Four-point Bending Tests.....	69
4.3.	Rectangular Column Tests.....	73
4.4.	I-Section Column Tests	84
5.	Conclusions	94
5.1.	Final Considerations.....	94
5.2.	Future Works.....	95
6.	References	97
7.	Appendix A – Four-point Bending Tests Reports.....	102
8.	Appendix B – Rectangular Column Tests Reports.....	105
9.	Appendix C – I-Section Column Tests Reports.....	113

List of Figures

Figure 1.1 – Roof structure consisting of four large precast TRC shells in RWTH Aachen University [2].	19
Figure 2.1 – Reinforcing systems of concrete [3].	22
Figure 2.2 – Different weaving patterns: (a) plain weave; (b) twill weave; (c) satin weave [19].	24
Figure 2.3 – Mechanical properties of selected high-performance filaments and yarns [19].	25
Figure 2.4 – Stress-strain diagram of textile reinforced concrete under uniaxial loading [3].	27
Figure 2.5 – Three states of equilibrium: (a) stable; (b) neutral; (c) unstable [30].	28
Figure 2.6 – Perfect columns behavior.	29
Figure 2.7 – Local buckling modes.	30
Figure 2.8 – Global buckling: (a) major axis flexural buckling; (b) minor axis flexural buckling; (c) torsional buckling.	31
Figure 2.9 - Effectives lengths of columns (adapted from [33]).	31
Figure 2.10 - Illustrative signature curve for a generic I-column.	32
Figure 2.11 – Perfect and real columns behavior.	33
Figure 2.12 – Southwell plot (adapted from [38]).	34
Figure 2.13 – Normalized strength curve for perfect and real columns.	35
Figure 2.14 – Forces applied in a deflected column [30].	36
Figure 2.15 – Interaction diagram of a reinforced concrete pin-ended column [30].	37
Figure 2.16 – Material and stability failures in the interaction diagram [30].	38
Figure 2.17 – Reduced interaction diagram: (a) curves for columns of the same length, L , and different eccentricities, e ; (b) diagrams for two different ratios of the end moments and for various values of the	

ratio L/h (adapted from [38]).	39
Figure 2.18 – Stress-strain curves: (a) concrete, (b) carbon fiber.	41
Figure 2.19 – Strain and stress distribution across the cross section of the beam.	42
Figure 2.20 – Strain distributions corresponding to points on the interaction diagram for a typical reinforced concrete column (adapted from [30]).	43
Figure 2.21 – Tested columns with 1.98% steel ratio: (a) axial force <i>versus</i> lateral deflection of columns a slenderness of 60; (b) interaction diagram of columns with a concrete strength of 63.5 MPa (adapted from [42]).	45
Figure 3.1 – Carbon fiber textile and its measures.	47
Figure 3.2 – Cross-sectional area of carbon yarn CY4 measured by image analysis.	48
Figure 3.3 – Carbon Textile: (a) no coating; (b) sand-coated.	49
Figure 3.4 – Flow table test for the matrix composition of plates.	50
Figure 3.5 – Molding process of plates for the four-point bending tests.	51
Figure 3.6 – Typical I-section with its nominal dimensions.	51
Figure 3.7 – Scheme of the acrylic formwork.	52
Figure 3.8 – Scheme of the position of the textile in the acrylic formwork.	52
Figure 3.9 – Molding process of the I-section columns in the acrylic formwork.	53
Figure 3.10 – Test specimens and their dimensions: (a) rectangular column; (b) CLC specimen.	53
Figure 3.11 – Carbon yarn uniaxial tension test scheme (adapted from [14]).	55
Figure 3.12 – Carbon yarn uniaxial tension test set-up.	55
Figure 3.13 – Matrix compression test fixture.	56
Figure 3.14 – CLC test scheme with dimensions in mm (adapted from [46]).	57
Figure 3.15 – Combined loading compression test fixture.	57
Figure 3.16 – Four-point bending test set-up.	58

Figure 3.17 - Signature curve for I-section columns: (a) local and global buckling modes; (b) chosen lengths.	59
Figure 3.18 – I-section columns test set-up: (a) square bar welded to a metal T-shape piece; (b) base plate with 35-mm thick steel plates welded to it.....	60
Figure 3.19 – Column being regularized with polyester-based body filler (<i>Iberê</i>).	60
Figure 3.20 – I-section test fixture with the displacement transducers.	61
Figure 3.21 – Signature curve for the rectangular columns and the chosen lengths.	62
Figure 3.22 – Rectangular column test fixture with the displacement transducers.....	62
Figure 4.1 – Stress-strain curves of the carbon yarn uniaxial tension test.	64
Figure 4.2 – Stress-strain curves of each specimen of the matrix compression test.	65
Figure 4.3 - Failure within the gage length: (a) CLC03; (b) CLC04.	66
Figure 4.4 – Stress-strain curves of the combined loading compression test.	67
Figure 4.5 – Stress-strain curve for CLC01 showing the fiber and matrix contribution.	68
Figure 4.6 – Textile position at the mid-length of plates: (a) FP2A; (b) FP2B; (c) FP3A.....	69
Figure 4.7 – Experimental load-displacement curves for each plate.	70
Figure 4.8 – Four-point bending test of FP2A: (a) before failure; (b) after failure.	71
Figure 4.9 – Experimental and theoretical moment-curvature curves for each plate.....	71
Figure 4.10 – Beginning of the experimental moment-curvature curves. .	72
Figure 4.11 – Overview of failure of columns: (a) PA.60.02; (b) PA.80.01; (c) PA.100.01; (d) PA.120.01.	74
Figure 4.12 – Cracks in columns PA.100.02: (a) close to the column's end; (b) mid-length.	74

Figure 4.13 – Load-deflections plots for the eight columns tested.....	75
Figure 4.14 – Rotation θ of column PA.80.02.....	75
Figure 4.15 – Displacement growth of column PA.120.01.....	76
Figure 4.16 – Representative plot of load <i>versus</i> shortening of column PA.80.01.....	77
Figure 4.17 – Southwell plot of column PA.60.01.....	77
Figure 4.18 – Experimental and theoretical plots for each length tested: (a) 60 cm; (b) 80 cm; (c) 100 cm; (d) 120 cm.	79
Figure 4.19 – $P\delta$ curves from PA.100.02 with δ_0 equal to 1.6mm: instability and tensile strength curves.....	80
Figure 4.20 – Strength curve and experimental points.	82
Figure 4.21 – Interaction diagram and experimental load-moment curves.....	82
Figure 4.22 – I-section scheme.	84
Figure 4.23 – Overview failure of columns: (a) PI.40.02; (b) PI.60.02; (c) PI.80.01; (d) PI.100.01; (e) PI.120.02.	85
Figure 4.24 – Load-deflections plots for all columns tested.....	85
Figure 4.25 – Displacement growth of column PI.120.01.	86
Figure 4.26 – Representative plot of load <i>versus</i> axial shortening of column PI.100.01.	86
Figure 4.27 – Representative Southwell plot of column PI.120.01.	87
Figure 4.28 – Experimental and theoretical plots for each length tested: (a) 40 cm; (b) 60 cm; (c) 80 cm; (d) 100 cm; (e) 120 cm.	88
Figure 4.29 – Load <i>versus</i> shortening of column PI.40.02.	89
Figure 4.30 – Column PI.60.02: (a) $P-\delta$ experimental curves for the two horizontal displacement transducers; (b) $P\delta$ curves presenting the theoretical plots for half-sections loaded with 50% to 80% of the total load considering an initial imperfection of 0.1 mm.	90
Figure 4.31 – Strength curve and experimental points.	92
Figure 4.32 – Interaction diagram and experimental load-moment curves.....	92

List of Tables

Table 3.1 – Cross-sectional area of carbon yarn test specimens.....	48
Table 3.2 – Matrix compositions: weights to produce one liter of concrete.....	49
Table 3.3 – Summary table of Characterization Tests.....	54
Table 4.1 – Tensile strength f_f and tensile moduli of elasticity E_f of the fiber yarn specimens.	64
Table 4.2 – Compressive strength f_c , compressive modulus E_c and strain of concrete at compressive stress peak ϵ_{c2} of the specimens.....	65
Table 4.3 – Dimensions and fiber percentage of CLC specimens.....	66
Table 4.4 – Compressive strength $f_{L,c}$ and longitudinal compressive modulus $E_{L,c}$ of the TRC specimens with 3.69% of fiber content.....	67
Table 4.5 – Compressive strength $f_{L,c}$ and longitudinal compressive modulus $E_{L,c}$ of the TRC specimens with 1.84% of fiber content.	68
Table 4.6 – Dimension of plates.	69
Table 4.7 – Flexural tensile strength f_{ctf} of concrete.	72
Table 4.8 – Lengths and average dimensions of each rectangular column.....	73
Table 4.9 – Initial imperfections of columns by Southwell plot, theoretical curve and the imperfection limits.....	81
Table 4.10 – Experimental and theoretical maximum loads.	81
Table 4.11 – Critical loads and relationship between experimental and theoretical non-dimensional slenderness obtained from the strength curve.	83
Table 4.12 – Lengths and average cross-section dimensions of each I-section column.	84
Table 4.13 – Initial imperfections of columns by Southwell plot, theoretical curves and the imperfection limits.....	91

Table 4.14 – Experimental and theoretical maximum loads.	91
Table 4.15 – Critical loads and relationship between experimental and theoretical non-dimensional slenderness obtained from the strength curve.	93

List of Symbols

Lowercase Roman Letters

b	width
b_f	flange width
d	depth
e	eccentricity
f_c	compressive strength of concrete
f_{ct}	tensile strength of concrete
f_{ctf}	flexural tensile strength of concrete
f_f	tensile strength of reinforcement
$f_{l,c}$	compressive strength of TRC
h	height
t	thickness
t_f	flange thickness
t_w	web thickness
x	distance of a certain fiber to the top of the cross-section
x_{NL}	neutral axis position
x_i	distance between top of the cross-section and reinforcement of the i^{th} layer
x_c	distance between top of the cross-section and the neutral axis

Uppercase Roman Letters

A_{fi}	area of reinforcement of the i^{th} layer
E_c	compressive modulus of elasticity of concrete
E_f	tensile modulus of elasticity of reinforcement
E_L	flexural modulus of elasticity
$E_{L,c}$	longitudinal compressive modulus of elasticity of TRC

I	moment of inertia about the minor axis
L	length
K_e	effective length factor
M	bending moment
M_c	bending moment at the end of column
M_e	bending moment at mid-length of column
M_u	ultimate bending moment
N	axial force
P	load
P_{cr}	critical load
$P_{L,c}$	compressive maximum load
P_{max}	maximum load
S	section modulus

Lowercase Greek Letters

δ	deflection
δ_s	shortening
δ_0	initial imperfection
δ_l	deflection at mid-length of the column
ε_c	strain of concrete
ε_{cu}	ultimate compressive strain of concrete
ε_{c2}	strain of concrete at compressive stress peak
ε_f	strain of reinforcement
θ	angle of rotation
λ	slenderness
$\overline{\lambda}$	non-dimensional slenderness
$\overline{\lambda}_{exp}$	experimental non-dimensional slenderness
$\overline{\lambda}_{theor}$	theoretical non-dimensional slenderness
σ_c	concrete stress
σ_f	reinforcement stress

χ relative ultimate strength

Uppercase Greek Letters

Φ curvature

1. Introduction

1.1. Overview

A composite material is obtained from the combination of two or more materials that work together to give the composite unique properties. One of the most important composite materials used for structural applications is reinforced concrete, in which concrete is responsible for carrying compressive stress while steel is responsible for carrying loads in tension zones. But some disadvantages such as the low strength-to-weight ratio and the low corrosion resistance of steel, are creating space for the development of new composite materials.

Textile Reinforced Concrete (TRC) is a composite material that combines a fine-grained concrete matrix and a textile reinforcement with a high strength-to-weight ratio, which allows the production of thin-walled and lightweight elements. Because of the flexible reinforcement, it is possible to create free forms and geometries. Moreover, the superior corrosion resistance of the textile if compared to conventional steel results in a final structure with enhanced durability even with small concrete cover [1].

The characteristics of the textile reinforced concrete are strongly influenced by the properties of the reinforcement, which can be natural or man-made fibers. In the present work, a bidirectional textile made of carbon fiber is studied. If compared to other man-made fibers like glass and aramid, carbon has higher modulus of elasticity and tensile strength, as well as better performance for corrosion, temperature and fatigue.

In aerospace and military industries, carbon is widely used in replacement of heavy metals to produce lighter and stronger aircrafts and military tanks. In Civil Engineering, the usual applications include strengthening and retrofitting of old structural elements.

Over the last few decades, intensive research has been carried out on the development of novel TRC for construction, especially on the flexural and tensile

behavior of the composite. Even though the use of TRC as primary load carrying members in structural systems is still very limited, a wide range of design possibilities arise as a result of the knowledge acquired on the material's behavior and modelling. An example of TRC application is shown in Figure 1.1.



Figure 1.1 – Roof structure consisting of four large precast TRC shells in RWTH Aachen University [2].

Although carbon fiber has a higher cost over steel and other fibers, cost-effective TRC structures can be obtained because of some reasons, such as: the reduced amount of reinforcement used due to its high strength; reduction in cross-section size due to small concrete cover; cost reduction with transportation and assembly in the case of precast elements. In addition, the overall cost in the service life may be smaller due to the maintenance cost reduction.

Up to the present time, there are no codes and standards providing guidance for the design of full-TRC structural members. However, many researches are underway worldwide to investigate properties and behavior of structures made of this material. Presently, a RILEM Technical Committee TC 201-TRC is dedicated to develop the first standard with provisions for structural use of TRC.

1.2. Motivation of Present Study

As previously stated, Textile Reinforced Concrete has many advantages over traditional construction materials. However, its use as the primary structural system is still very limited. One of the motivations of this work arises from the necessity of extending the investigation on the structural behavior of TRC members, contributing to the development of design guidelines to allow for the safe use of the material in structures.

The second motivation is to investigate the behavior of Textile Reinforced Concrete columns. The use of slender and lightweight TRC members leads to reduced stiffness with respect to traditional reinforced concrete members [3], resulting in important stability problems. Although the phenomenon of buckling of reinforced concrete members has been studied by several authors, no work on TRC columns was found in the database used in this study.

Finally, ACI 440.1R-15 [4] and some authors like Nanni [5] recommend disregarding the reinforcement contribution of fiber-reinforced polymer bars in compressed reinforced concrete elements, although recent works point to the opposite [6–9]. Therefore, the consideration of the contribution of textile in compressed TRC members constitutes the third motivation for this work.

1.3. Objectives

The main objective of the dissertation is to investigate the performance and strength of TRC columns under concentric compression. An experimental program was carried out with I-section and rectangular columns having different lengths. The program included concrete casting, material characterization, experimental determination of apparent imperfections and compressive strengths and discussions on the failure modes and factors affecting the overall behavior.

A secondary objective of this work consists on validating an analytical model developed to predict non-linear axial-force-moment-curvature relationships (N-M- Φ), comparing the theoretical results with experimental results for four-point bending tests conducted in carbon-TRC plates.

Finally, from these relations, a numerical model was developed to predict the load-displacement behavior of columns subjected to compression. The numerical results were then compared to those obtained experimentally. An interaction diagram for TRC columns was also developed.

All tests were conducted at the Structures and Materials Laboratory of Civil and Environmental Engineering Department (LEM/DEC) at Pontifical Catholic University of Rio de Janeiro (PUC-Rio) during the year of 2017.

1.4. Organization of the dissertation

This dissertation is organized as follows.

In Chapter 2, a literature review is divided in two parts. The first one contains the main properties and characteristics of Textile Reinforced Concrete and its constituents (matrix and textile). The second part presents a literature review about the behavior of a column subjected to axial compression. Topics as failure modes, behavior of perfect and real columns and signature curve are discussed. As no works on TRC columns were found in the database, aspects on the behavior of conventional reinforced concrete are also reviewed.

In Chapter 3, the experimental program is described including material description and molding processes adopted. The testing set-ups, instruments and equipment necessary to perform the material characterization and compression tests in I-section and rectangular columns are detailed.

In Chapter 4, the results of the experimental program are presented including cross-section measurements, stress-strain curve for materials, load-deflection curves for plates and columns, initial imperfections, strengths and failure modes. Results for plates and columns are compared to those obtained using numerical techniques and comparisons and discussions related to the behavior of the tested columns are presented.

In Chapter 5, conclusions and suggestions for future works are presented.

2. Literature Review

2.1. Textile Reinforced Concrete (TRC)

2.1.1. Overview

In the last few decades, different methods have been developed to substitute the steel reinforcement in concrete, in order to obtain a high strength, high durability and lighter element [10]. Natural and man-made fibers stood out, leading to the development of Fiber Reinforced Concrete (FRC), which combines a cementitious matrix with randomly distributed short fibers (e.g. steel, glass, or polymeric) [11].

The first research efforts to combine continuous fibers and inorganic binders were made in the 1990s in Germany, enabling the creation of Textile Reinforced Concrete (TRC) [10], which is a composite material made of a fine-grained concrete matrix with a textile as reinforcement. This allows the production of thinner and lightweight elements with high load-bearing capacities [12–14]. Figure 2.1 presents the different reinforcing systems of concrete.

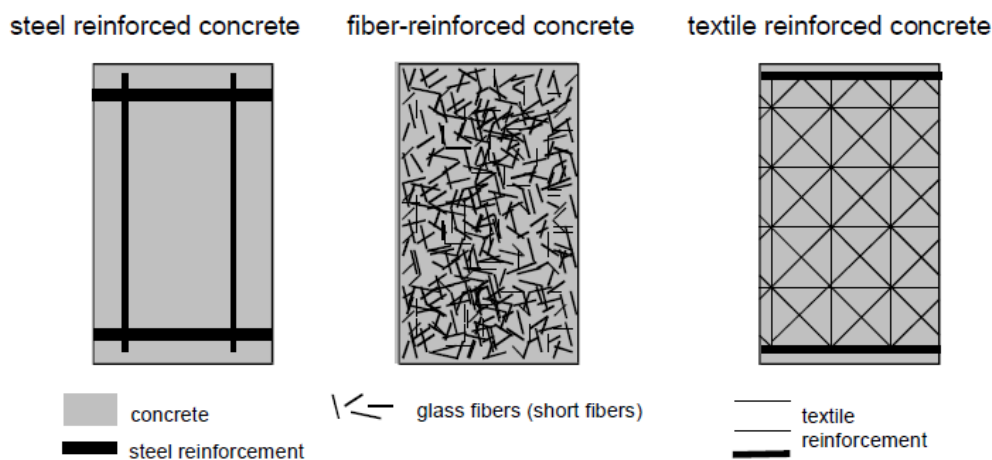


Figure 2.1 – Reinforcing systems of concrete [3].

TRC offers viable alternative solutions to conventional materials such as reinforced concrete, which are prone to corrosion. It has also advantages over FRC because in TRC the filaments can be oriented parallel to the direction of the forces, increasing the load-carrying capacity. It is also called “Textile Reinforced Mortar” (TRM) in Europe and “Fabric Reinforced Cementitious Matrix Systems” (FRCM) in the USA.

2.1.1.1. Concrete Matrix

In a composite material, the matrix has three main functions: bind the reinforcement together, transfer loads to the reinforcement and protect the fibers from environmental and physical damage [15].

The matrix used for TRC is a concrete with a maximum grain size ranging between 1 and 2 mm, depending on the distance between the yarns of the textile, the thickness of the textile layers and the dimensions of the structural element [16].

The design of the matrix composition must consider three important aspects: production processes, durability of the textile and desired mechanical properties of TRC. Typically, the matrix is very fluid in order to penetrate into the meshes of the textile and to obtain a good bonding behavior [17]. This flowable consistency can be achieved with the use of high performance plasticizers.

According to Triantafillou [10], the most often used fine-grained for TRC production has a water/binder ratio of 0.3 with a binder content of 40 to 50% by volume. A high content of binder is crucial for a good bonding behavior between matrix and textile reinforcement. This high binder content and the addition of different pozzolanic additives (*e.g.* fly ash or silica fume) leads to a densification of the concrete structure and may provide a considerable enhancement of the strength development [17].

2.1.1.2. Textile

Textiles consist on an arrangement of continuous fiber yarns which are oriented and connected. A yarn is the reunion of several hundred to several

thousand of individual filaments, which are elementary fibers. The linear density of the yarn, indicated as tex (weight in grams of 1000 meters of yarn), depends on the number of filaments, the fiber density and the average filament diameter [18].

The manufacture process is one of the parameters which influence the properties of the yarns. The most common textile fabrics for reinforcing concrete are: plane and circular scrims; plane, circular and three-dimensional spacer warp knits; and woven fabrics [19]. Figure 2.2 shows different weaving patterns of textiles.

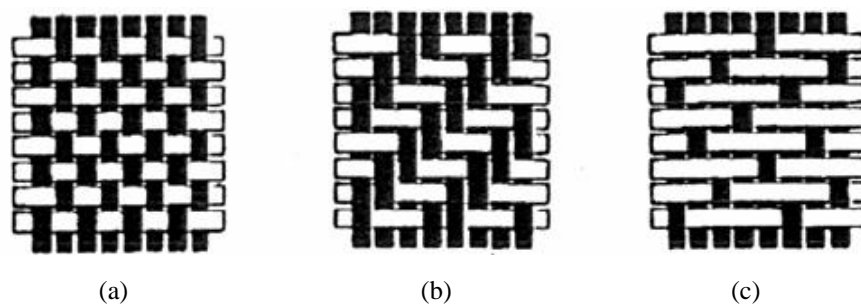


Figure 2.2 – Different weaving patterns: (a) plain weave; (b) twill weave; (c) satin weave [19].

The characteristics of TRC are decisively influenced by the amount and the arrangement of the fiber materials. To work as an effective reinforcement, the fiber material must have high fiber tenacity, high failure elongation and a modulus of elasticity much higher than that of the concrete. In addition, the textile has to exhibit good durability in alkaline environment of matrix and maintain its properties. Some other desirable requirements are: low creep under permanent load, low cost and good adhesion between textile and concrete [19].

Fiber materials are classified into natural and man-made fibers. Natural fibers (*e.g.* cotton, jute and sisal) are a sustainable choice, but they are not suitable for high performance TRC. Even though they have low cost and low density, they also have poor adhesion, variability of properties, low temperature resistance and hydrophilic behavior [20]. In the other hand, man-made fibers (*e.g.* carbon, glass and aramid) meet the requirements for efficient reinforcement of high performance TRC.

Figure 2.3 compares mechanical properties of some man-made fibers, showing the difference between filament and yarn. The yarn is obtained by gluing

the filaments with polymeric resin (mainly epoxy), which is important to protect and bond the filaments together, eliminating the slippage between them.

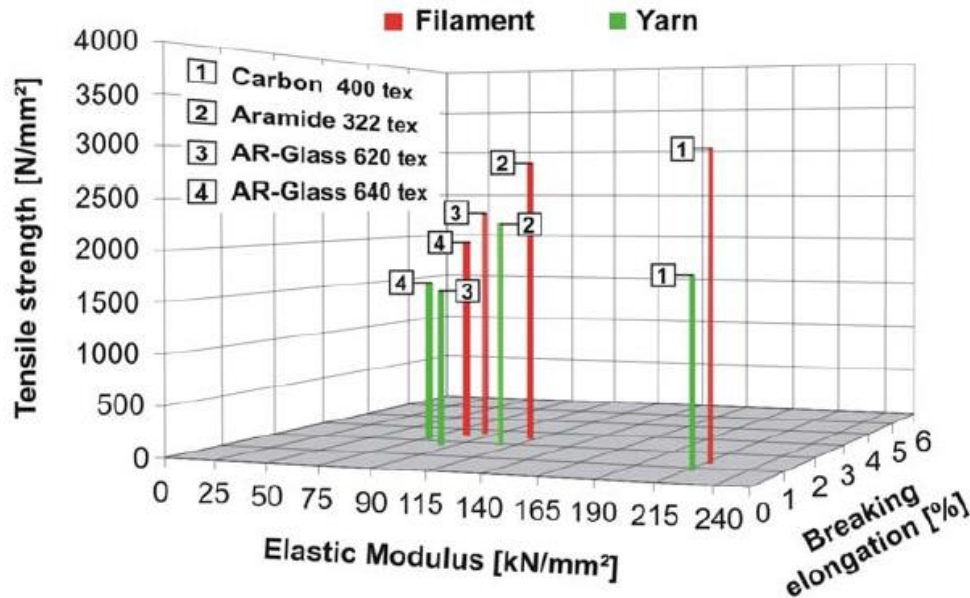


Figure 2.3 – Mechanical properties of selected high-performance filaments and yarns [19].

In this study, a bidirectional textile made of carbon fiber was used. Carbon fiber was chosen due to its high modulus of elasticity and strength. As this fiber is an anisotropic material, its modulus of elasticity is different in the two principal directions. It ranges from 250 to 390 GPa in longitudinal direction and from 12 to 20 GPa in transverse direction [15]. Depending on the type of treatment of the basic fiber - which includes carbonization, graphitization and oxidation - it is possible to make carbon fibers with different values of resistance and modulus of elasticity.

According to Gries *et al.* [19], carbon fiber offers some other good properties, such as: low density, very little creep behavior, low heat expansion and conductivity, good electric conductivity, low X-ray absorption, high resistance to acid, alkaline and organic solvents.

Even though carbon fiber has great properties to be an efficient reinforcement for TRC, it has two disadvantages. The first one is its poor adhesion to concrete. To improve the bond behavior between textile and matrix, special coatings may be used. The second, and main disadvantage, is its cost.

However, considering the several advantages offered by the material, carbon fibers can be more cost effective than other man-made fibers.

2.1.2. Bond behavior

In Textile Reinforced Concrete, the bond between matrix and reinforcement is very important. An adequate bonding behavior is required for stress transfer from the concrete to the textile. It depends on friction between the two components and is affected by coating, matrix composition and textile properties such as material, geometry and volume fraction.

Concerning the textile geometry, the bond of a woven fabric to the cement matrix is significantly better than the bond of a single yarn [21,22]. The weft yarns function to anchor the textile in the cementitious matrix, improving the bond between them [23,24].

Donnini *et al.* [25] investigated the effect of different types and amounts of coatings applied to a flexible carbon textile on the bond behavior between fabric and mortar. Experimental results showed improvement of the bond between materials even with the use of low percentages of resin, although the best results occurred with a surface coating with high level of epoxy impregnation and sand.

Bahr [26] studied the influence of sand-coated and plain-coated test specimens in a tensile test. The sand-coated specimens presented better results since its tensile strength was higher and its average crack spacing was smaller (27.3 mm) when compared to the plain-coated specimens (70 mm).

2.1.3. Mechanical behavior

The mechanical behavior of TRC is usually described by means of bending or tension tests. Figure 2.4 presents a typical average stress-strain curve for a member subject to uniaxial tensile loading. It shows a similar behavior to conventionally reinforced concrete and can be divided in four states: state I (uncracked concrete), state IIa (cracking formation), state IIb (stabilized crack pattern) and state III (failure).

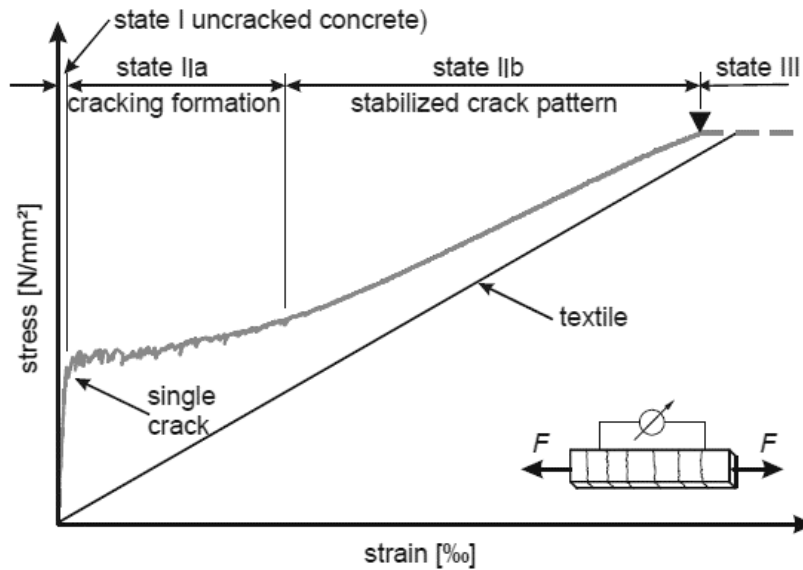


Figure 2.4 – Stress-strain diagram of textile reinforced concrete under uniaxial loading [3].

According to Hegger *et al.* [3], the linear elastic range observed from the beginning of loading until the first crack formation on the concrete matrix is defined as State I. At this point, the modulus of elasticity of the matrix is the same as the Young's modulus of the composite. State IIa consists on the formation of multiple cracking of the composite and the load transfer from matrix to textile due to the bond between both materials. Stronger bond produces closely spaced small cracks. When the crack formation stabilizes, the State IIb is initiated. In this stage, the composite curve is approximately parallel to the stress-strain curve of the equivalent curve for the 'pure' reinforcement, indicating a certain contribution of the concrete between cracks that becomes less significant with load increase. Finally, the failure of the composite occurs when the tensile failure of the textile is reached (state III).

Many parameters are important to the analysis of the mechanical behavior such as the effect of different fiber materials, fabric geometries, reinforcement ratio and coatings which are examined in tension and bending tests, performed by many authors.

Uniaxial tensile tests were performed by Hegger & Voss [27] and Jesse [28] (*apud* [3]). They tested thin flat TRC specimens made of different types of fibers, including carbon fiber, and different fiber orientations (angle between fibers and loading direction). Jesse [28] (*apud* [3]) showed that, for angles between 0 and 10°, there is a small reduction of the load-carrying capacity and,

from 10° to 30° , the strength remains approximately constant and gradually reduces until reaching less than 50% in 45° . Hegger & Voss [27] also have shown that a slope of 45° caused a 50% reduction in strength.

Hegger & Voss [29] performed four-point bending tests on TRC I-section profiles varying the reinforcing ratio, showing a linear increase in load-carrying capacity with ratio increase. Additionally, they showed that textiles having yarns with greater cross-sections presented a lower load-bearing capacity compared to smaller ones. In fact, specific superficial area is greater for smaller cross-section yarns, therefore resulting in a better load-transfer between matrix and reinforcement and in a more effective composite behavior.

As previously stated, no work of compression on TRC elements was found in the database consulted.

2.2. Columns Behavior

2.2.1. Overview

Buckling can be defined as the loss of original shape of a structural member subject to compressive stress associated with the change in the state of equilibrium. Because of buckling, stability analysis is very important in slender structures, such as slender columns and thin plates.

The stability concept, can be easily illustrated using the analogy of a ball displaced laterally and released on different types of surfaces, as shown in Figure 2.5. In the stable equilibrium, the ball will return to its original position, whereas in the unstable equilibrium, it will roll off the hill. The transition between stable and unstable equilibrium is neutral equilibrium, in which the ball rests on a flat plane.

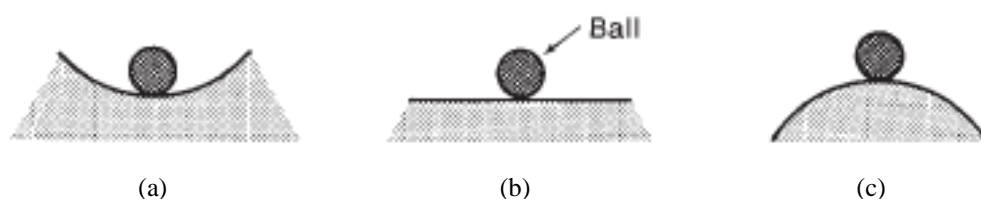


Figure 2.5 – Three states of equilibrium: (a) stable; (b) neutral; (c) unstable [30].

Similar states of equilibrium exist for columns subject to axial compression. For example, if a pin-ended column is slightly disturbed laterally at mid-length and returns to its original configuration after disturbance ceases, it is in a state of stable equilibrium. Whereas, in the state of unstable equilibrium it does not return to its original position.

2.2.2. Perfect Members

Perfect columns are defined as initially perfectly straight members subject to a concentric compression force P [31] and its behavior is shown in Figure 2.6. The structural member is in a stable equilibrium until the load P increases from zero to the critical load P_{cr} . After this point, called bifurcation point, the column may continue the fundamental path in an unstable state of equilibrium or may follow the post-critical path in a stable configuration, in which the column exhibits buckling – large deflections changing its original shape. Unlike the case of plates, columns are characterized by a flatter post-critical path with a negligible post-buckling resistance gain.

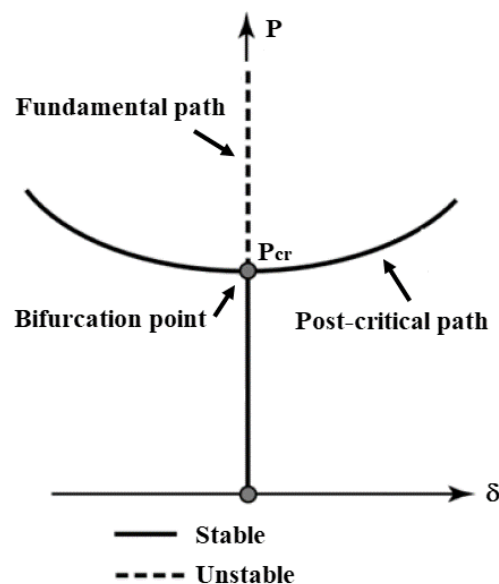


Figure 2.6 – Perfect columns behavior.

A perfect column under axial compressive loads may exhibit the following failure modes: crushing, local buckling and global buckling (Euler buckling). Each behavior is discussed in the following sections.

2.2.2.1. Crushing

Crushing is a type of failure which occurs to a structural member subjected to compression due to material failure, without any lateral deformation. The stress limit to prevent crushing is obtained by multiplying the compression strength of composite material by its cross-sectional area.

2.2.2.2. Local Buckling

Local buckling is defined as the mode which the axis of the member is not distorted but there is a loss of the original cross-section shape. It normally occurs in short columns and is shown in Figure 2.7.

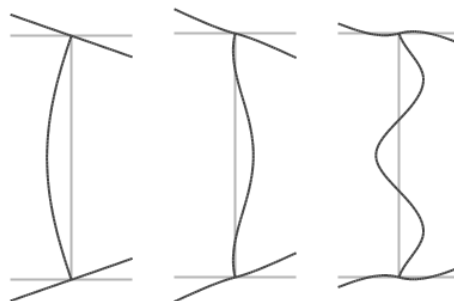


Figure 2.7 – Local buckling modes.

2.2.2.3. Global Buckling

Global buckling is characterized by a distorted longitudinal axis of the member, with a single half-wavelength overall mode shape and with no deformation in its cross-section. This kind of failure is more likely to occur for long columns and, for symmetric members, two different buckling modes may be observed: flexural and torsional buckling, as shown in Figure 2.8.

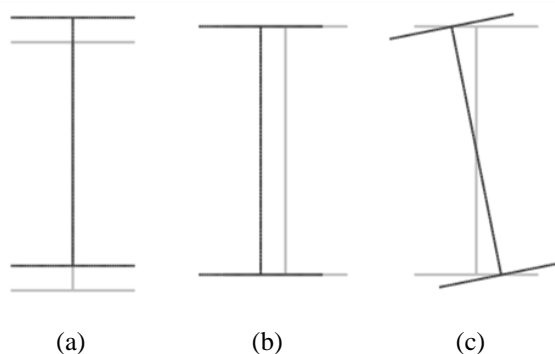


Figure 2.8 – Global buckling: (a) major axis flexural buckling; (b) minor axis flexural buckling; (c) torsional buckling.

The dominant mode experienced in a doubly symmetric section, which is the subject of this work, is the flexural buckling mode [32]. For this mode, the critical load P_{cr} , also called Euler's buckling load, defined as the maximum load supported by the perfect column, is given by Euler's formula according to Eq. (2.1).

$$P_{cr} = \frac{\pi^2 E_L I}{(K_e L)^2} \quad (2.1)$$

where E_L is the flexural modulus of elasticity, I is the moment of inertia about the minor axis, L is the column length and K_e is the effective length factor, depending on the end conditions, as presented in Figure 2.9.

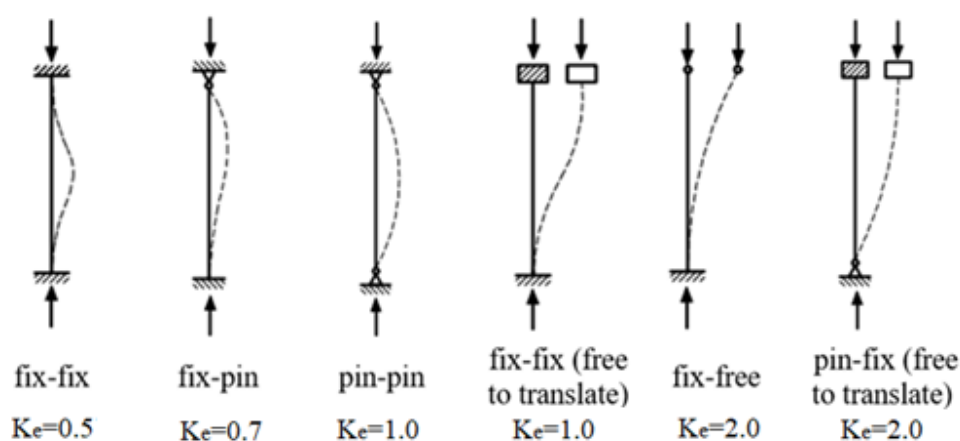


Figure 2.9 - Effectives lengths of columns (adapted from [33]).

2.2.2.4. Signature Curve

Signature curve is a curve that correlates the critical load of a column with its length. It is used on the identification of the buckling modes that influence a structural element. Figure 2.10 presents an example of the signature curve of a pin-ended generic I-section column, with the horizontal axis in logarithmic scale. It can be noticed that global buckling is the governing buckling mode for longer columns whereas for shorter columns the local buckling mode is the one that governs.

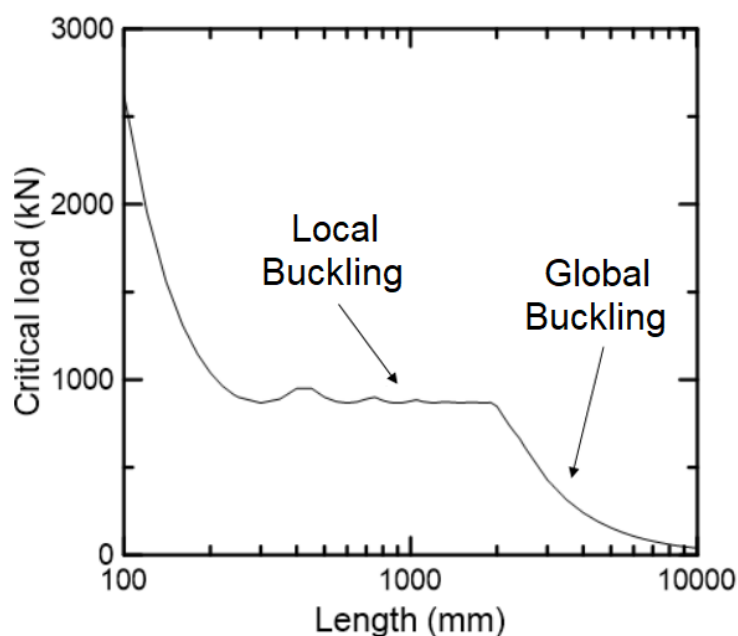


Figure 2.10 - Illustrative signature curve for a generic I-column.

A signature curve accounting for the various buckling modes can be obtained using Generalized Beam Theory (GBT) [34], which considers the contribution of the plate deformations in the geometric stiffness matrix of the element, making it possible to determine the contribution of each mode to the critical load. With a computational implementation of this method, through *GBTul software* [35], it is possible to predict critical loads for each length and evaluate the occurrence of several instability modes in columns.

2.2.3. Real Columns

Real columns exhibit imperfections such as geometric (*e.g.* lack of straightness) and associated to the materials (*e.g.* nonlinear stress-strain relationship). When a real column is subject to a compression force P , the deflections grow quickly as the load approaches the critical load, but there is no bifurcation point in this case. In addition, second-order effects amplify the lateral deflections and produce additional bending moments, reducing member capacity when compared to perfect columns. Lower initial imperfections lead to a behavior closer from the perfect column behavior. The behavior of perfect and real columns is presented in Figure 2.11, in which δ_0 and δ are the initial out-of-straightness and total lateral deflection, respectively.

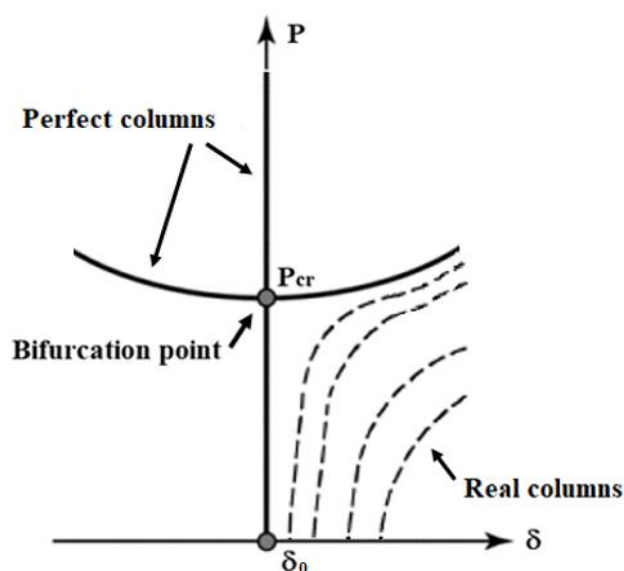


Figure 2.11 – Perfect and real columns behavior.

On a buckling test, the imperfections will have a considerable influence on the results. They are very difficult to control and can occur in any production process, especially in the molding processes of cementitious matrix elements. These imperfections can be associated to overall out-of-straightness, as well as thickness variation and misalignment of the reinforcement, causing a shift in the geometric center. It also can be related to a loading eccentricity in the test. The geometric imperfections of columns may be associated to the member length and estimated as a fraction of the column length L (*e.g.* $\delta_0 < L/500$). On the other

hand, loading eccentricities are more related to the cross-section size, *i.e.* deeper sections may be subject to greater loading eccentricity due to difficulties in ensuring uniform loading distribution throughout cross-section at the members ends [36].

Real members are subject to coupling between local and buckling modes. In order to study only one mode, it is important to maintain a ‘distance’ between local and global critical loads, which can be given by the signature curve.

2.2.3.1. Southwell Plot

The Southwell plot is the most used method for the evaluation of critical loads of imperfect columns. Southwell [37] presents Eq. (2.2) which correlates the load P , the critical load P_{cr} , the displacement δ and the initial imperfection δ_0 .

$$\delta = \frac{\delta_0}{\frac{P_{cr}}{P} - 1} \quad (2.2)$$

Eq. (2.2) may be transformed in an equation of a straight line, given by Eq. (2.3), in which δ/P and δ are plotted along the horizontal and vertical axis.

$$\delta = P_{cr} \frac{\delta}{P} - \delta_0 \quad (2.3)$$

Therefore, the Southwell plot is obtained by linearizing the plot P versus δ into a plot δ versus δ/P , as shown in Figure 2.12. The critical load is obtained as the slope of the regression line used through the middle portion of the data points, while the intercept of the vertical axis gives the magnitude of the imperfection of the column.

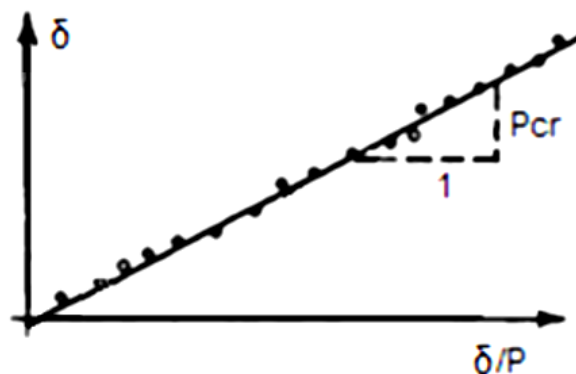


Figure 2.12 – Southwell plot (adapted from [38]).

The critical load obtained by the Southwell plot can be only applied on the analysis of structures with a well-defined yield strength level. Columns made of cementitious materials do not exhibit this yield level because of its nonlinearity and cracking behavior. Hence, in this case, care must be exercised to use Southwell plot, as it is only valid while the material behaves in a linear elastic manner.

2.2.3.2. Strength Curve

The strength curve, presented in Figure 2.13, consists in a plot of the member non-dimensional slenderness $\bar{\lambda}$ versus relative ultimate strength χ , expressed by Eqs. (2.4) and (2.5).

$$\bar{\lambda} = \sqrt{\frac{P_{L,c}}{P_{cr}}} \quad (2.4)$$

$$\chi = \frac{P_{u,e}}{P_{L,c}} \quad (2.5)$$

where $P_{L,c}$ is the compressive maximum load in the longitudinal direction, P_{cr} is the critical load and P_{max} is the maximum load.

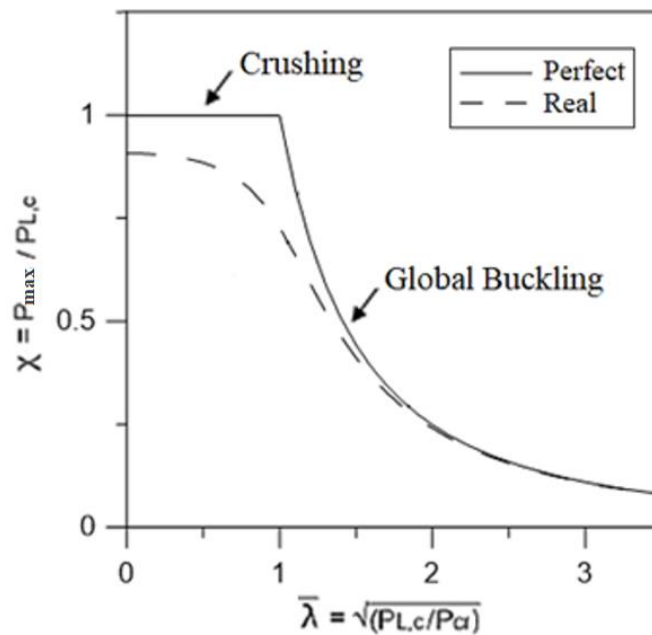


Figure 2.13 – Normalized strength curve for perfect and real columns.

For perfect columns with lower slenderness ($\lambda < 1$), failure occurs by crushing, whereas for greater slenderness ($\lambda > 1$), failure is governed by global buckling, since the critical load is smaller than the limit of the material strength. For real columns, interaction between crushing and buckling occurs, reducing the capacity with respect to perfect behavior. The slenderness $\lambda = 1$ corresponds to the maximum interaction between the two modes, for which maximum erosion of capacity is expected.

2.2.3.3. Interaction Diagram for Reinforced Concrete Columns

The most important parameters that influence the load at which the structure becomes unstable are the material and geometry properties that affects its slenderness (equal to L/r , where r is the radius of gyration). MacGregor and Wight [30] define a slender column as “a column that has a significant reduction in its axial-load capacity due to moments resulting from lateral deflections of the column”. If the ratio of the column length to its cross-section dimensions is sufficiently large, the column is considered slender [38].

Considering a reinforced concrete pin-ended symmetrical column subject to compression loads P applied with an eccentricity e , showed in Figure 2.14, the moments at the ends of the column M_e can be expressed by Eq. (2.6). When the loads P are applied, the column deflects laterally by an amount of δ , increasing the value of the maximum moment at mid-length, M_c , as presented in Eq. (2.7).

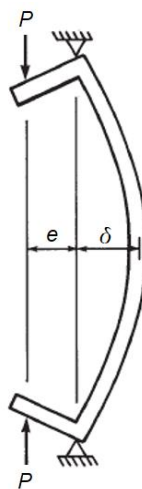


Figure 2.14 – Forces applied in a deflected column [30].

$$M_e = Pe \quad (2.6)$$

$$M_c = P(e + \delta) \quad (2.7)$$

The possible combinations of axial load and moment required to cause failure in a reinforced concrete member are represented by an interaction diagram, as shown in Figure 2.15. This diagram, also called failure envelope, can be obtained from balance of forces and moments in the cross-section, considering all possible failure configurations (curvatures and positions of neutral axis) [38]. The dashed line $O-A$ is a plot of Eq. (2.6) in which M_e is a linear function of P , whereas the curved line $O-B$ is a plot of Eq. (2.7) where the moment M_c is the sum of the end moment, Pe , and the moment due to the deflections, $P\delta$.

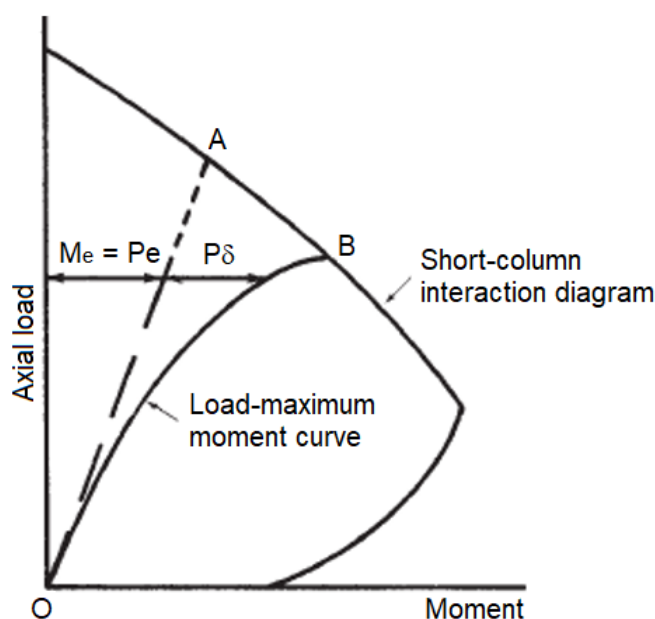


Figure 2.15 – Interaction diagram of a reinforced concrete pin-ended column [30].

Failure occurs when the load-moment curve $O-B$ intersects the interaction diagram, in other words, at point B. The axial-load capacity is reduced from A to B because of the slenderness effects, *i.e.*, increase in maximum moment due to deflections [30]. Figure 2.16 presents the load-moment curves for columns with the same configuration and three different lengths.

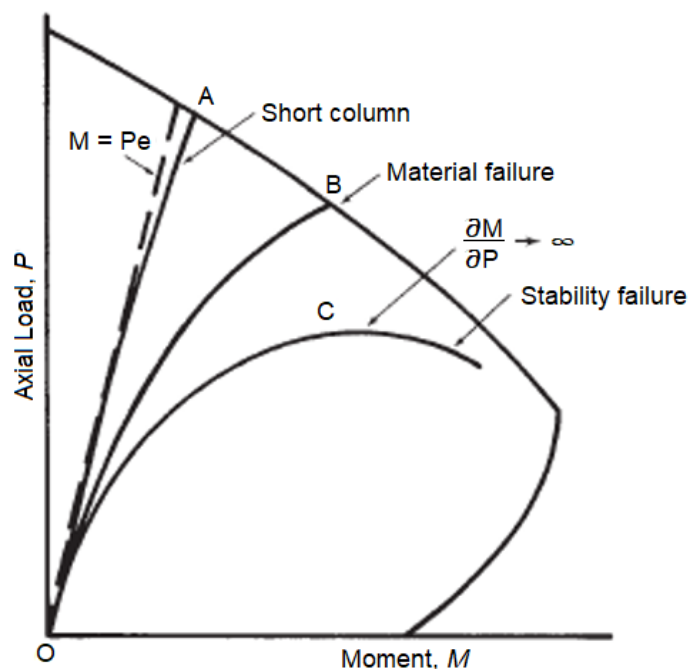


Figure 2.16 – Material and stability failures in the interaction diagram [30].

The curve O-A represents a short column and is similar to the dashed line $M = Pe$, due to the occurrence of small deflections and negligible second order effects. For an intermediate column, represented by curve O-B, considerable second order effects due to moderate deflections occur, increasing the bending moment and reducing the capacity to axial load. This type of failure is known as a material failure. Meanwhile, for a very slender column, the behavior is represented by line O-C, in which the column may reach a deflection where the value of the $\partial M / \partial P$ approaches infinity or becomes negative. This kind of failure is called stability failure because the column becomes unstable due to the drop at the load capacity after further deflections [30].

Figure 2.17(a) compares the curves for columns having same length, L , and different eccentricities, e . Connecting the projection of each failure point horizontally on the radial line of slope, the reduced interaction diagram is obtained, which incorporates the second-order effects as a function of the column slenderness. Figure 2.17(b) shows the reduced interaction diagrams for two different ratios of the end moments and for various values of the ratio L/h (where h is the height of rectangular cross section) [38].

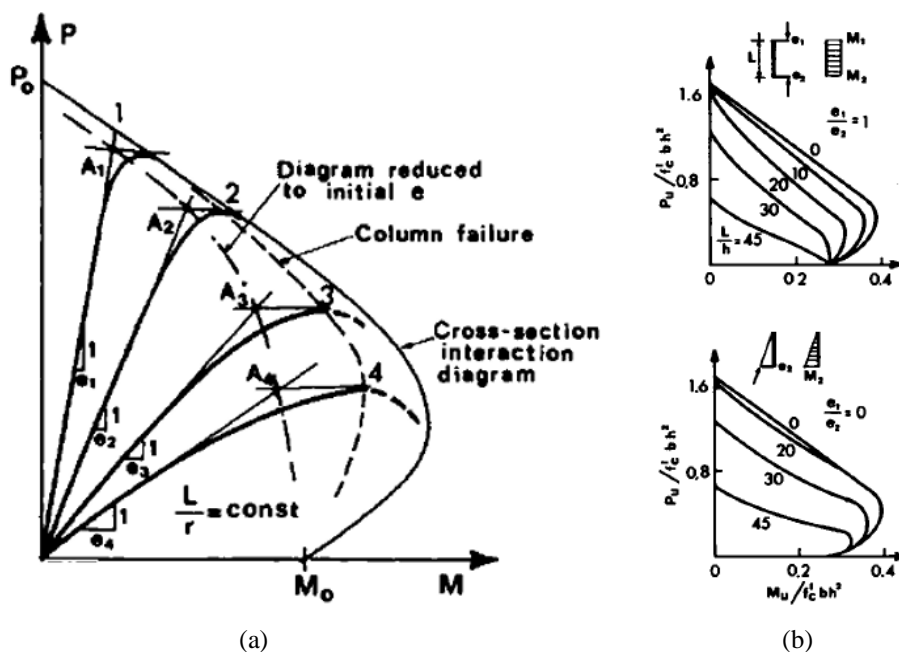


Figure 2.17 – Reduced interaction diagram: (a) curves for columns of the same length, L , and different eccentricities, e ; (b) diagrams for two different ratios of the end moments and for various values of the ratio L/h (adapted from [38]).

2.2.4. Numerical Models

Columns made of cementitious materials exhibit inelastic behavior and its material non-linearity needs to be taken in account. Hence, they require non-linear analysis in order to evaluate the effects of the imperfections on the member strength and behavior.

To study the behavior of reinforced concrete columns, three different types of analysis are usually carried out:

- 1) Axial force-moment-curvature;
- 2) Failure envelope;
- 3) Beam-column.

These analyses may be adapted to the case of TRC columns, replacing the properties of the steel for those of the fiber. The description, background and particularities of each analysis are discussed in the following sections.

2.2.4.1. Axial Force-Moment-Curvature Relationship (N-M- Φ)

The axial force-moment-curvature relationship (N-M- Φ) provides correlation between these three parameters considering a cross-section equilibrium analysis. In a column analysis, for example, the bending moment can be obtained if the applied axial force and the curvature – 2nd derivative of deflection – are known.

The following assumptions are usually made to obtain N-M- Φ relationships: i) sections remain plane after bending; ii) perfect bond between concrete and reinforcement; and iii) stresses can be obtained from the stress-strain relationships for each material comprising the cross-section.

Many idealized stress-strain diagrams are proposed in literature for concrete. The model proposed by Hognestad [39], which consists in approximating the stress-strain relationship by a parabolic curve, is still one of the most used in concrete modeling, as defined in Eq. (2.8). For the reinforcement, a linear stress-strain diagram with similar tensile and compressive behavior is usually assumed [3,9], as shown in Eq. (2.9). A graphical representation for each of these stress-strain relationships is presented in Figure 2.18.

$$\sigma_c = \begin{cases} 0, & \text{when } \varepsilon_c < \varepsilon_{cu} \\ f_c \left(1 - \left(1 - \frac{\varepsilon_c}{\varepsilon_{c2}} \right)^n \right), & \text{when } \varepsilon_{cu} \leq \varepsilon_c \leq 0 \\ E_c \varepsilon_c, & \text{when } 0 < \varepsilon_c \leq \frac{f_{ct}}{E_c} \\ 0, & \text{when } \varepsilon_c > \frac{f_{ct}}{E_c} \end{cases} \quad (2.8)$$

where σ_c is the stress, ε_c is the strain of concrete, ε_{cu} is the ultimate compressive strain of concrete, ε_{c2} is the strain of concrete at compressive stress peak, f_c and f_{ct} are the compressive and tensile strengths of concrete, respectively, E_c is the modulus of elasticity of concrete and n is the empirical parameter which depends on the concrete strength. In this work, the value adopted is 2 because it represented well the stress-strain experimental curve.

$$\sigma_f = \begin{cases} 0, & \text{when } \varepsilon_f < \frac{-f_f}{E_f} \\ E_f \varepsilon_f, & \text{when } \frac{-f_f}{E_f} \leq \varepsilon_f \leq \frac{f_f}{E_f} \\ 0, & \text{when } \varepsilon_f > \frac{f_f}{E_f} \end{cases} \quad (2.9)$$

where σ_f is the stress, ε_f is the strain, f_f is the strength and E_f is the modulus of elasticity of reinforcement.

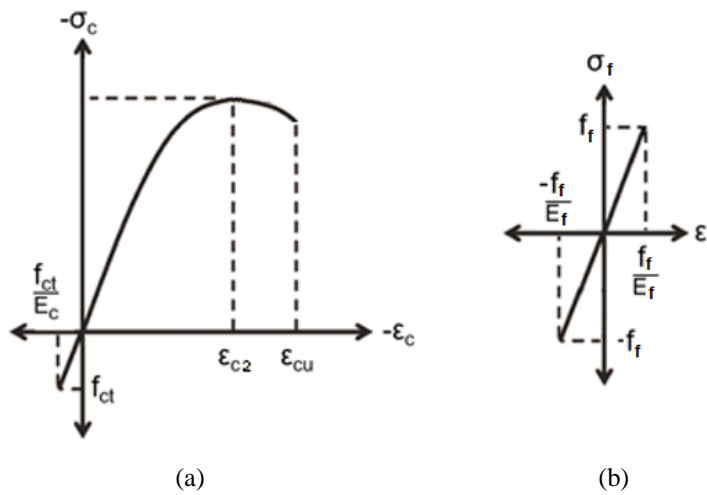


Figure 2.18 – Stress-strain curves: (a) concrete, (b) carbon fiber.

Assuming a monosymmetric cross-section with a certain geometry and reinforcement distribution subject to an axial force, N , and a bending moment about the non-symmetry axis, M , shown in Figure 2.19, equilibrium of forces and moments in a cross-section gives the following relationships between internal stresses and applied forces:

$$N = \int_0^h \sigma_c(x)b(x)dx + \sum_{i=1}^n \sigma_f(x_i)A_{fi} \quad (2.10)$$

$$M = \int_0^h \sigma_c(x)b(x)xdx + \sum_{i=1}^n \sigma_f(x_i)x_iA_{fi} - Nx_c \quad (2.11)$$

where x is the distance of a certain fiber to the top of the cross-section, h is the depth of the beam, $b(x)$ is the variable width of the beam, A_{fi} and x_i are the area of reinforcement of the i^{th} layer and its position, respectively, and x_c is the distance between top of cross-section and the neutral axis.

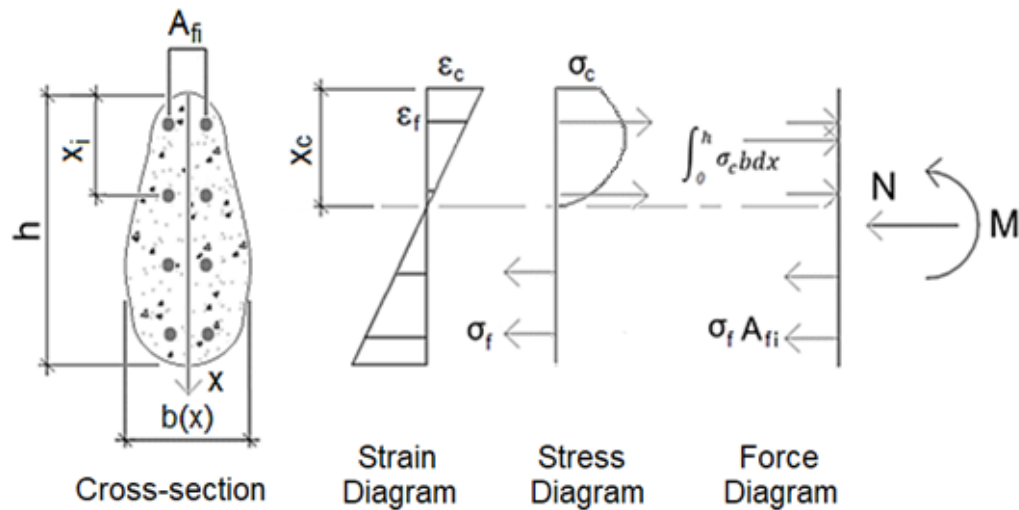


Figure 2.19 – Strain and stress distribution across the cross section of the beam.

It is important to mention that the concrete and fiber stresses depend on the strains distribution in the cross section, which depends on the curvature, Φ , and the neutral axis position, x_{NL} .

For each chosen value of curvature, Eqs. (2.10) and (2.11) can be solved to determine the neutral axis position and the corresponding bending moment. Therefore, it is possible to obtain the relation N - M - Φ for beams. It can be developed iteratively implementing a routine in a mathematical software.

2.2.4.2. Failure Envelope (Interaction Diagram)

The TRC failure envelope can be obtained from the following steps:

- 1) Assume a certain linear strain distribution corresponding to failure, *i.e.* in which either fiber or concrete limit strain are assumed;
- 2) Determine the tensile and compressive stresses in tension and compression using concrete and reinforcement stress-strain relationships – Eqs. (2.8) and (2.9). In this case, the tensile strength of the concrete is neglected in the analysis.
- 3) Determine axial load N and the bending moment M that fulfill balance conditions to the assumed strain distribution, Eqs. (2.10) and (2.11).

Steps 1 through 3 are repeated until all possible failure configurations (curvatures and positions of neutral axis) are considered. The failure envelope

corresponds to the curve containing all these N , M pairs. It can be developed iteratively implementing a routine in a mathematical software. Figure 2.20 illustrate a series of strain distributions and the corresponding points on an interaction diagram for a typical reinforced concrete column.

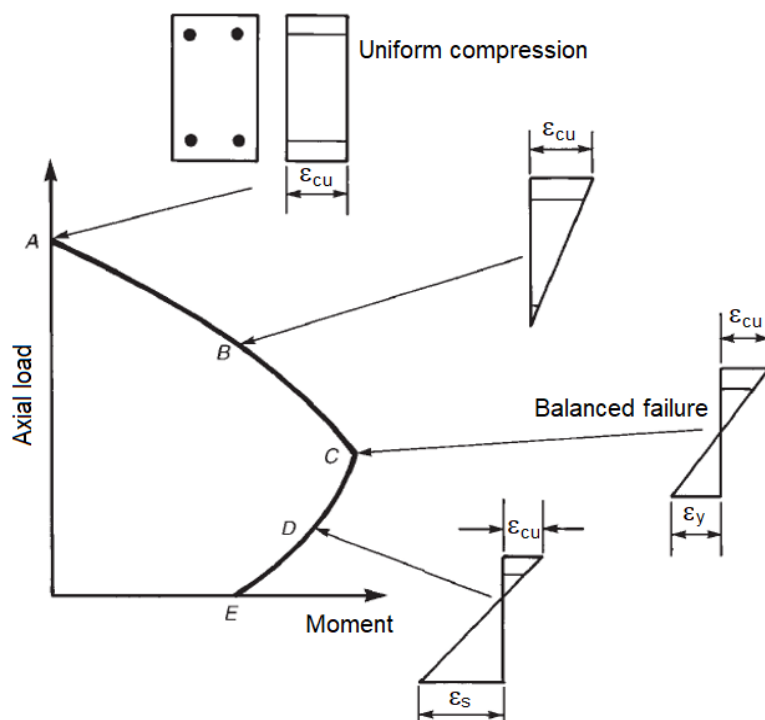


Figure 2.20 – Strain distributions corresponding to points on the interaction diagram for a typical reinforced concrete column (adapted from [30]).

2.2.4.3. Beam-column Model

In a column analysis, a beam-column model is necessary to calculate the lateral deflections and second-order effects in the column. This task is relatively complicated for reinforced concrete members due to non-linear behavior of material and beam-column analysis usually involves iterative methods. ‘Exact’ approaches to obtain load-lateral deflection curve are reported in literature [9,40,41] and usually consist in dividing member length into small discrete intervals, therefore leading to systems with multiple degrees of freedom (DOF) that require greater calculation effort. A simpler alternative is described by Bazant and Cedolin [38], consisting in approximating the deflection, δ , by a sinusoidal

function, resulting in a single DOF model. For a pin-ended column, the function presented in Eq. (2.12) is suggested.

$$\delta = -\delta_1 \sin(\pi x / L) \quad (2.12)$$

where δ_1 is the deflection at the mid-length ($x=L/2$) of the column, L is the length of the column and x is the position along the longitudinal axis of a column.

By definition, the curvature Φ is the 2nd derivative of the deflection and is given in Eq. (2.13).

$$\Phi = \left(\frac{\pi}{L} \right)^2 \delta_1 \sin(\pi x / L) \quad (2.13)$$

Combining Eqs. (2.12) and (2.13), it is possible to correlate the deflection at the mid-length ($x=L/2$) of the column, δ_1 , with the curvature at the same point, as shown in Eq. (2.14).

$$\delta_1 = -\Phi \left(\frac{L}{\pi} \right)^2 \quad (2.14)$$

For a pin-ended column with an initial out-of-straightness, δ_0 , the equilibrium at a cross-section located at the column mid-length is given by Eq. (2.15).

$$\delta_1 + \delta_0 = \frac{M}{N} \quad (2.15)$$

From the equations defining N and M (Eqs. (2.10) and (2.11)) and the established correlation between δ_1 and Φ (Eq. (2.14)), it is possible to find, for a given arbitrary curvature, which position of the neutral line satisfies the condition given in Eq. (2.15). Therefore, the corresponding axial force can be determined. The numerical process for obtaining the P - δ curve consists of varying the curvature and obtaining the corresponding values of P and δ .

2.2.5. Behavior of Reinforced Concrete Columns

As no works on TRC columns were found in the database consulted, this section summarizes some studies on slender reinforced concrete columns and concrete columns reinforced with Fiber-Reinforced Polymer (FRP) Bars. These

studies may vary on concrete strength, reinforcement type and ratio, cross-sectional geometry, slenderness ratios, boundary conditions and eccentricities.

Kim and Yang [42] investigated the effects of concrete strength and longitudinal steel ratio on the ultimate load and axial force-moment relation of columns by experimental and numerical analysis. They tested thirty reinforced concrete columns with a square section with 80 mm width, pinned at both ends and with an eccentricity of 24 mm, using three different concrete strengths (25.5, 63.5 and 86.2 MPa), two different longitudinal steel ratios (1.98 and 3.95%) and three slenderness ratios (10, 60 and 100). As a result, the ultimate load has significantly increased for a high strength short column but not for a slender one. The stability failure in slender columns is more likely to happen for higher concrete strengths. The results also showed that the increase in the longitudinal steel ratio contributed more effectively to the increase in the ultimate load for slender columns than for the shorter ones. Figure 2.21(a) presents the axial force *versus* lateral deflection of the columns with a steel ratio of 1.98% and a slenderness of 60. The interaction diagram presenting the axial force versus bending moment of columns with a steel ratio of 1.98% and a concrete strength of 63.5 MPa is shown in Figure 2.21(b).

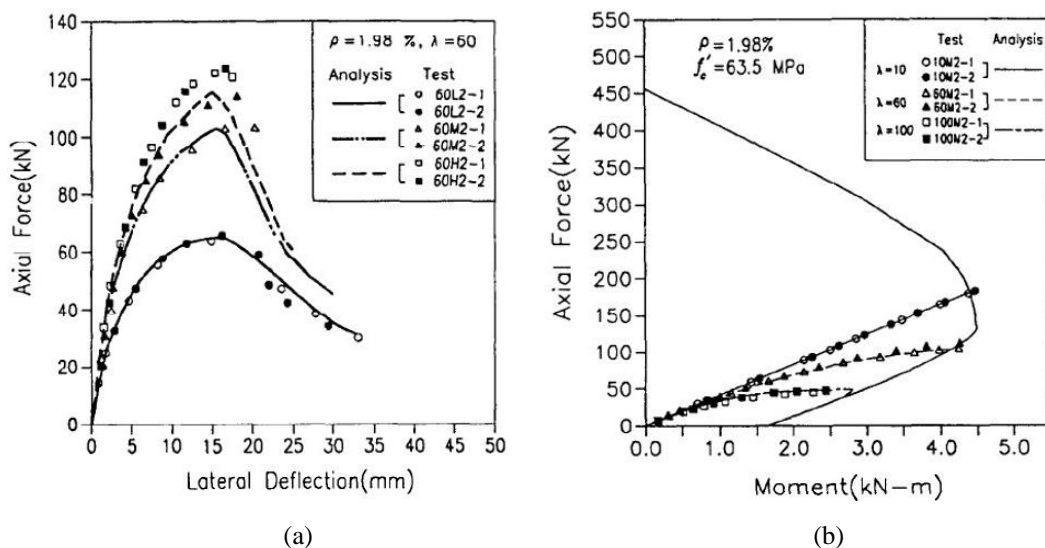


Figure 2.21 – Tested columns with 1.98% steel ratio: (a) axial force *versus* lateral deflection of columns a slenderness of 60; (b) interaction diagram of columns with a concrete strength of 63.5 MPa (adapted from [42]).

Pallares *et al* [43] studied the behavior of reinforced concrete columns subjected to axial force and biaxial bending. Fifty-six high strength concrete slender columns with a cross-section of 200 x 100 mm and lengths of 1, 2 and 3 m were tested. The experimental results revealed that less slender columns and columns with higher eccentricities present a material failure and more slender columns and with small eccentricities fail due to instability. For intermediate cases, columns can present both types of failures. It also showed that greater slenderness and eccentricity values decrease the ultimate load.

Afifi *et al.* [6] investigated the axial capacity of circular columns reinforced with Glass Fiber Reinforced Polymer (GFRP) bars. The experimental results showed that concrete columns reinforced with steel and GFRP bars have similar behavior, although the axial capacities of the GFRP reinforced concrete columns were 7.0% lower.

Paramanantham [7] tested fourteen concrete columns reinforced with GFRP bars with 200 mm width, 200 mm thick and 1800 mm long. The author showed that the reinforcing bars would only be stressed up to 20 to 30% of the respective ultimate strength in compression.

Kawaguchi [8] subjected to eccentric tension and compression twelve concrete columns reinforced with aramid fiber-reinforced polymer (AFRP) bars with 150 mm width, 200 mm thick and 1400 mm long. He reported that concrete columns reinforced with AFRP bars can be analyzed using the same procedure as for steel-reinforced concrete columns.

Choo *et al.* [9] investigated the behavior of short and slender rectangular concrete columns reinforced with FRP bars through axial load-moment and moment–curvature relationships, developed using the assumptions for conventional steel reinforcement. They compared the theoretical results with the experimental results obtained from some authors like Paramanantham [7] and Kawaguchi [8]. As expected, an increase in the slenderness ratios led to an overall decrease in the reduced interaction diagram of the slender concrete columns. Choo *et al.* [9] concluded that ignoring the reinforcement contribution of FRP in compressed members, as recommended by ACI 440.1R-15 [4] and Nanni [5], may be conservative.

3. Experimental Program

3.1. Overview

In this chapter, an experimental program addressing the behavior of carbon-TRC columns conducted at the Structures and Materials Laboratory of Civil and Environmental Engineering Department at PUC-Rio (LEM/DEC) is described. These elements were manufactured at the laboratory and the relevant material properties for reinforcement and matrix were determined experimentally. Simply-supported plates were tested under flexure and columns with different lengths were tested under concentric compression. Column tests included pinned-ended I-section members and fixed-ended rectangular plates. Details concerning molding processes, testing equipments and set-ups used are provided in following sections.

3.2. Material Description

The textile used in the present work was the *SITgrid017*, a bidirectional carbon fiber mesh manufactured by *V.Fraas*. Figure 3.1 presents the textile and its measures.

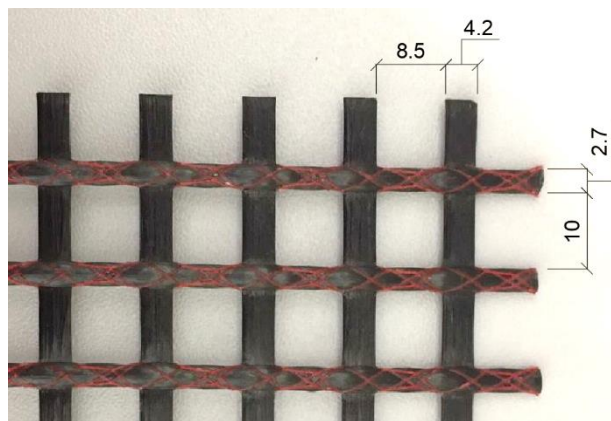


Figure 3.1 – Carbon fiber textile and its measures.

Cross-sectional area of carbon yarns was measured by image analysis. Four test specimens were used and the average result was 3.32 mm^2 , as shown in Table 3.1. Figure 3.2 presents the image analysis from test specimen CY4.

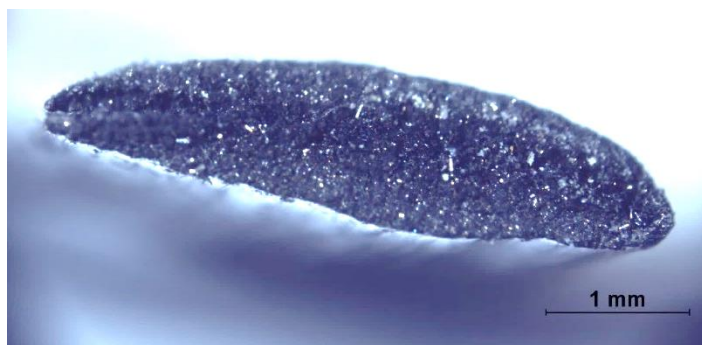


Figure 3.2 – Cross-sectional area of carbon yarn CY4 measured by image analysis.

Table 3.1 – Cross-sectional area of carbon yarn test specimens.

Specimen	Area (mm^2)
CY1	3.39
CY2	3.21
CY3	3.19
CY4	3.47
Average	3.32 ± 0.392
cov ⁽¹⁾	0.118

⁽¹⁾ Coefficient of variation

To improve bonding between textile and concrete, the textile (580 g/m^2) was impregnated with epoxy resin (Sikadur 32) and quartz sand. The impregnation was made using a sponge to spread the resin all over the fabric. Additionally, a layer of sand (with a maximum grain size of 1.18 mm) was applied above the resin. Both materials were weighed before the application. However, as the coating was manually applied, some variability was expected. After the impregnation, the textile weighed approximately 1786 g/m^2 . The carbon textile, with and without the impregnation, is presented in Figure 3.3.

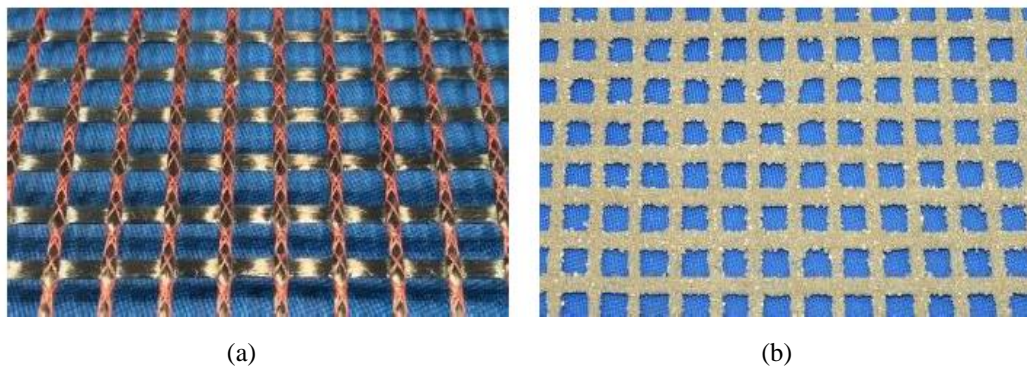


Figure 3.3 – Carbon Textile: (a) no coating; (b) sand-coated.

The fine-grained concrete used in the manufacturing of TRC is described in the work of Silva *et al.* [44]. Even though the matrix was the same in all molding processes, the fluidity had to be higher for the columns when compared to plates. In order to increase the fluidity of the matrix maintaining the water-to-binder ratio of 0.30, an adjustment was made increasing the quantity of super plasticizer and reducing the amount of water. The materials and their respective weights for the molding processes of plates and columns are presented in Table 3.2. This matrix is characterized by high fluidity and fine granulation, grains smaller than 2 mm, in order to penetrate the meshes of the fabric and obtain a good bond behavior.

Table 3.2 – Matrix compositions: weights to produce one liter of concrete.

Material	Weight (g)	
	Plates	Columns
Sand (1.18 mm)	947	947
CP2 cement	632	632
Fly ash	265	265
Micro silica	50.5	50.5
Water	280	266
Super plasticizer (Glenium)	6.31	25.0

The concrete was mixed in a planetary mixer (Amadio, model 20LA). At the beginning, all dry materials were added in the bowl and the powder was mixed for one minute at low speed (125 RPM). Then, the water was added and the

concrete was stirred for four minutes at medium speed (220 RPM). Finally, the super plasticizer was added and the matrix was mixed for four minutes at high speed (450 RPM).

In order to determine the consistency of the fresh concrete, a flow table test [45] was carried out. A cone with 65 mm high, 80 mm top diameter and 125 mm base diameter was used. Slumps of 365 and 390 mm in diameter were measured for the matrix composition of plates and columns, respectively. Figure 3.4 presents the flow table test for the matrix composition of plates.



Figure 3.4 – Flow table test for the matrix composition of plates.

3.3. Molding Processes

Different geometries and molding processes were used for each type of test.

A cylindric steel formwork of Ø100x200 mm was used to produce three test specimens for concrete compression tests. The concrete used was the same used for plates and it rested inside the formwork for 24 hours at room temperature. After removed, the test specimens were placed in a curing chamber.

TRC plates for the four-point bending tests were manufactured in a steel formwork in order to produce three rectangular plates with 120 mm width, 12 mm thick and 1000 mm long, with 2.08% of textile volume fraction. The concrete was poured in a 3 mm layer, as this was the dimension of the spacers positioned on

both ends of the formwork. After that, the textile was placed above the concrete layer. Then, three spacers were put in place and the concrete was added until it reached approximately 12 mm, as shown in Figure 3.5. A plastic film was used to seal the system for the next 24 hours. Afterwards, TRC test specimens were removed from the mold and placed in a curing chamber, where they would cure for 27 days.

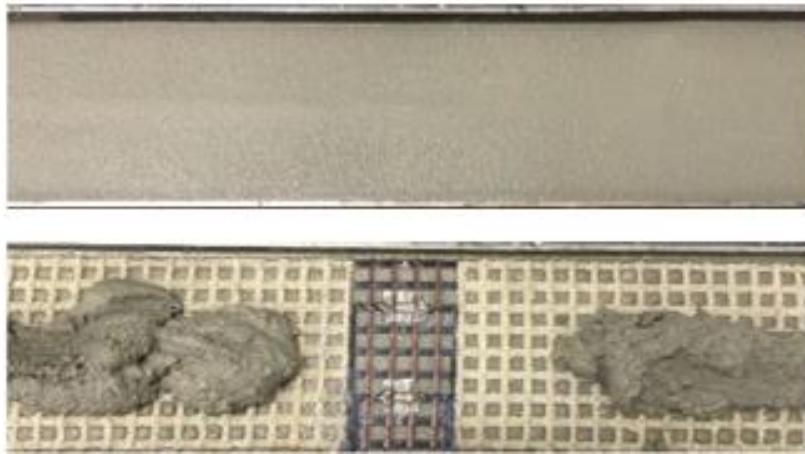


Figure 3.5 – Molding process of plates for the four-point bending tests.

The I-section columns were produced in a formwork formed by five acrylic pieces (four for the laterals and one for the bottom) attached with screws. This formwork was able to produce columns with the following dimensions: 100 mm web, 50 mm flanges, 12 mm thick and variable lengths (up to 1500 mm), as shown in Figure 3.6. Figure 3.7 presents the scheme of the acrylic formwork.

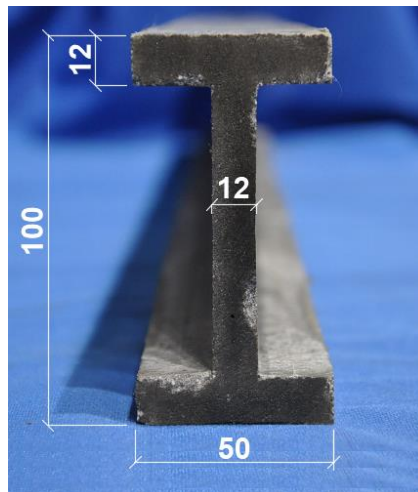


Figure 3.6 – Typical I-section with its nominal dimensions.

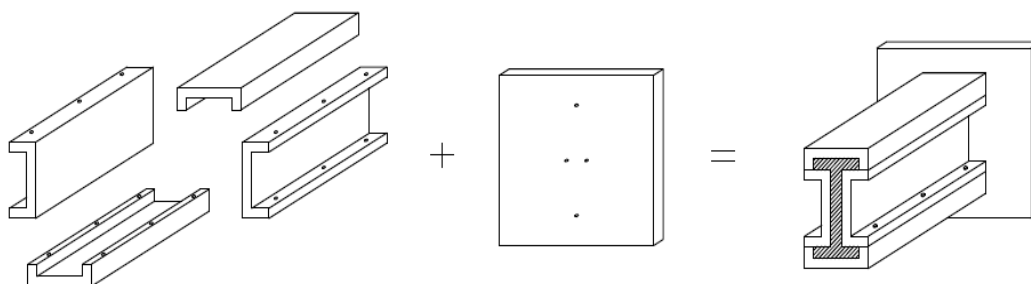


Figure 3.7 – Scheme of the acrylic formwork.

The molding process of the I-sections columns began with spreading a thin layer of grease inside the acrylic parts with a sponge. After that, the textiles of the web and flanges – putted together in order to form an I-shaped reinforcement, as shown in Figure 3.8 – were placed in the middle of the section with 4 mm spacers glued on both sides to ensure correct positioning of the reinforcement. Then, all pieces were positioned and attached by screws and the formwork was placed vertically. To prevent the concrete from leaking, a sealing tape was used along formwork junctions and plastic clamps were positioned all over the height. Afterwards, the concrete was poured from the top into two funnels until it reached the desired height. The concrete rested inside the formwork for 72 hours at room temperature and, after removed, the columns were placed in a curing chamber until the day of the test (from 28 to 34 days, depending on the specimen). Ten columns were produced with a textile volume fraction of 1.94%. Figure 3.9 shows the molding process of the I-section columns in the acrylic formwork.

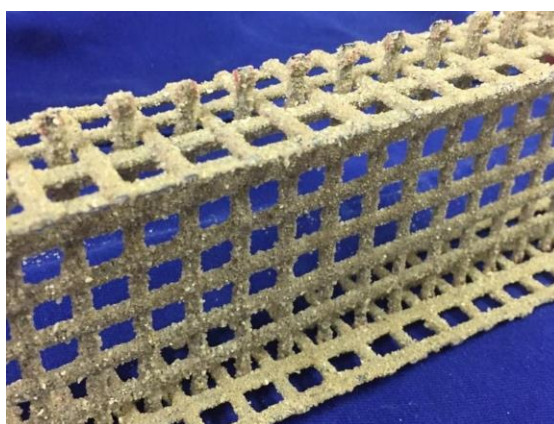


Figure 3.8 – Scheme of the position of the textile in the acrylic formwork.

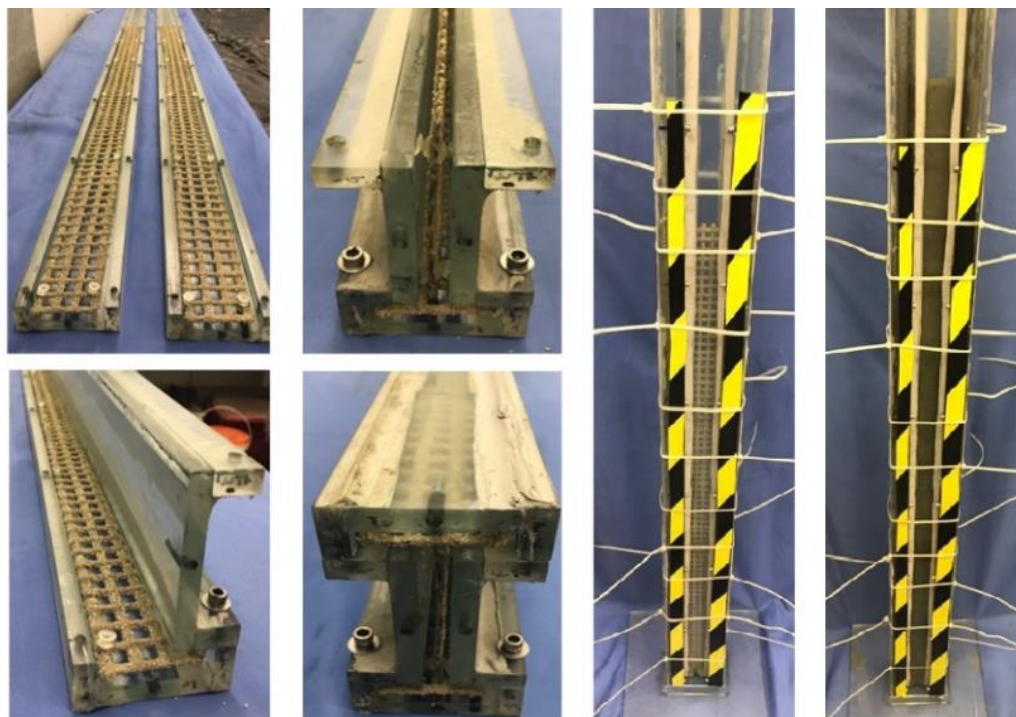


Figure 3.9 – Molding process of the I-section columns in the acrylic formwork.

The rectangular columns for the compression tests were obtained from cutting the flanges from the I-section columns in a table saw with water lubricated diamond blade. After cut, eight columns of approximately 70 mm wide and 12 mm thick were produced with a textile volume fraction of 2.37%, as shown in Figure 3.10(a). The same saw was used to produce six specimens for the combined loading compression (CLC) tests, measuring 15x12x155 mm, as shown in Figure 3.10(b).

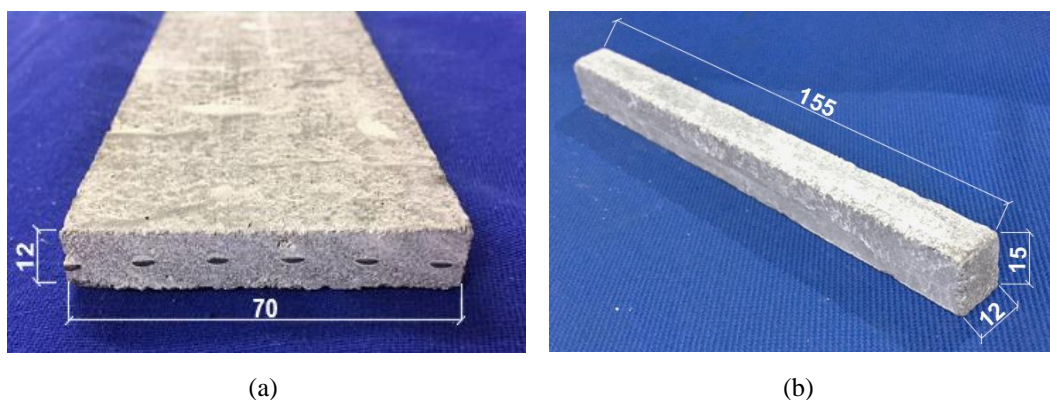


Figure 3.10 – Test specimens and their dimensions: (a) rectangular column; (b) CLC specimen.

3.4. Material Characterization

The material properties were determined experimentally through four characterization tests, listed in Table 3.3.

Table 3.3 – Summary table of Characterization Tests.

Characterization Tests	Number of specimens	Properties Obtained
Carbon yarn uniaxial tension test	2	Tensile strength and modulus of the reinforcement (f_f and E_f)
Matrix compression test	3	Compressive strength, modulus and strain at compressive stress peak of concrete (f_c , E_c and ε_{c2})
Combined loading compression test	6	Compressive strength and longitudinal modulus of TRC ($f_{L,c}$ and $E_{L,c}$)
Four-point bending test	3	Flexural tensile strength of concrete (f_{ctf})

3.4.1. Carbon Yarn Uniaxial Tension Test

Carbon yarn uniaxial tension tests were carried out to obtain the tensile strength and modulus of elasticity of the textile. Two carbon yarns with 1.80 m long were tested.

The set-up adopted was similar to that used by Gries *et al.* [19], who performed this test on alkali-resistant glass filament yarns. The modified set-up consisted of two steel cylinders, measuring 115 mm in diameter and 20 mm thick. Test specimen ends contoured each cylinder two times, which were pressed by clamps in the machine. A strain gage was positioned in one side of the middle-span of the specimen to provide an accurate strain measurement. The tests were conducted up to failure under a displacement rate of 1 mm/min on a universal testing machine *MTS frame model 311.11*, with load capacity of 1000 kN. Figure 3.11 presents the test scheme and Figure 3.12 presents the set-up.

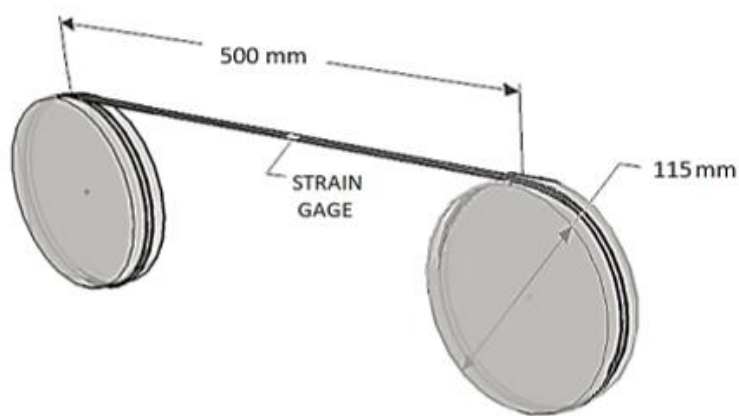


Figure 3.11 – Carbon yarn uniaxial tension test scheme (adapted from [14]).



Figure 3.12 – Carbon yarn uniaxial tension test set-up.

3.4.2. Matrix Compression Test

In order to determine the compressive strength and stress-strain curve for matrix, compression tests were conducted. Three cylindric specimens $\varnothing 100 \times 200$ mm were tested using a testing machine *Controls 50-C46Z00*, with load capacity of 2000 kN. To obtain the strains, two vertical displacement transducers, coupled to acrylic rings, were positioned around the specimen. The compressive axial load was applied at a rate of 0.25 MPa/s until failure of the specimen. The matrix compression test fixture is presented in Figure 3.13.



Figure 3.13 – Matrix compression test fixture.

3.4.3. Combined Loading Compression Test

A combined loading compression (CLC) test [46] was conducted on six TRC specimens 15 mm wide, 12 mm thick and 155 mm long. In this test, shear and end loading are combined with the objective of achieve sufficient shear loading in order to eliminate end crushing [47].

The main objective of this test was to evaluate the influence of the fiber on the compressive strength, since a porous interface is created between matrix and textile. Therefore, the compressive strength and the stress-strain curve for the TRC composite were obtained.

Two strain gages were positioned back-to-back on the middle of the specimen's face. As in this test the only kind of failure accepted is the one that occurs within the gage length, the test specimens were glued between aluminum plates of 2 mm, with an epoxy resin (Sikadur 32) in order to prevent end crushing.

The specimen was positioned on the test apparatus, showed in Figure 3.14, and a torque of 10 Nm was applied in the screws. The test consisted of loading the specimen under a displacement rate of 0.3 mm/min on a *MTS model 810* universal testing machine with load capacity of 500 kN. The test set-up is presented in Figure 3.15.

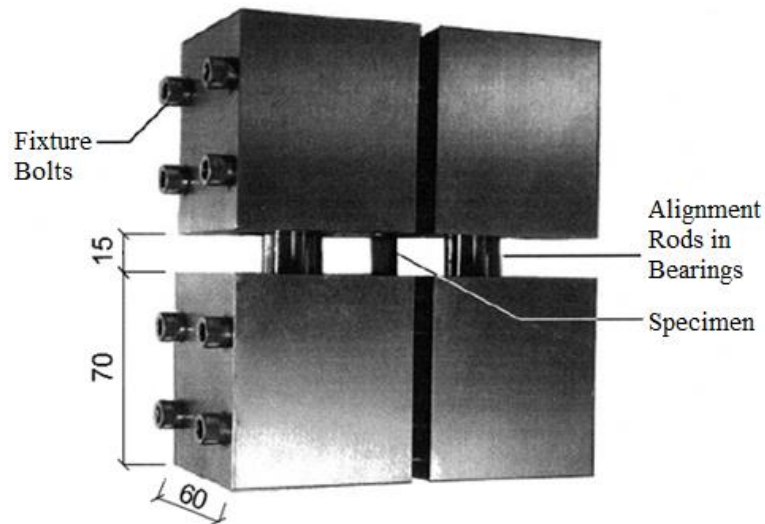


Figure 3.14 – CLC test scheme with dimensions in mm (adapted from [46]).



Figure 3.15 – Combined loading compression test fixture.

3.4.4. Four-point Bending Tests

Four-point bending tests were conducted in carbon-TRC plates in order to validate an analytical model able to predict non-linear moment-curvature relationships ($M-\Phi$).

The supports were positioned at 50 cm from each other and the load application points were positioned at 16.7 cm from each support. The test was performed on a servo-hydraulic machine with displacement control at a rate of 1.5

mm/min until failure. In order to measure the textile's deformations, four strain-gages were glued to the surface of the textile, two in the upper face of the textile and two in the lower one, in the mid-length of the plate. This region was not impregnated with resin and sand, as shown in Figure 3.5. Another strain-gage was glued on the upper face of the composite plate to measure the deformations in this region. An aluminum plate was glued to the bottom of the plate to position a displacement transducer capable of measuring the deflections of the plate at mid-span. The test set-up is presented in Figure 3.16.

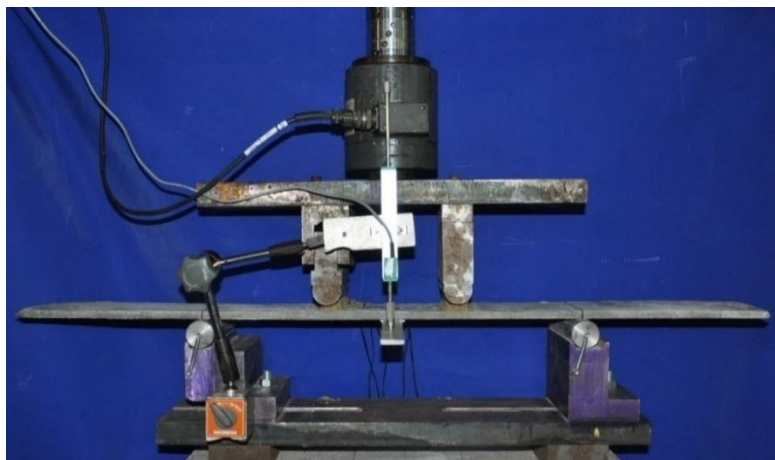
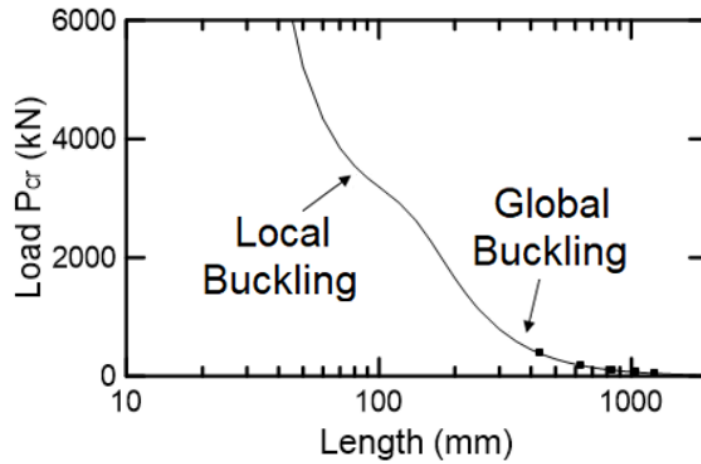


Figure 3.16 – Four-point bending test set-up.

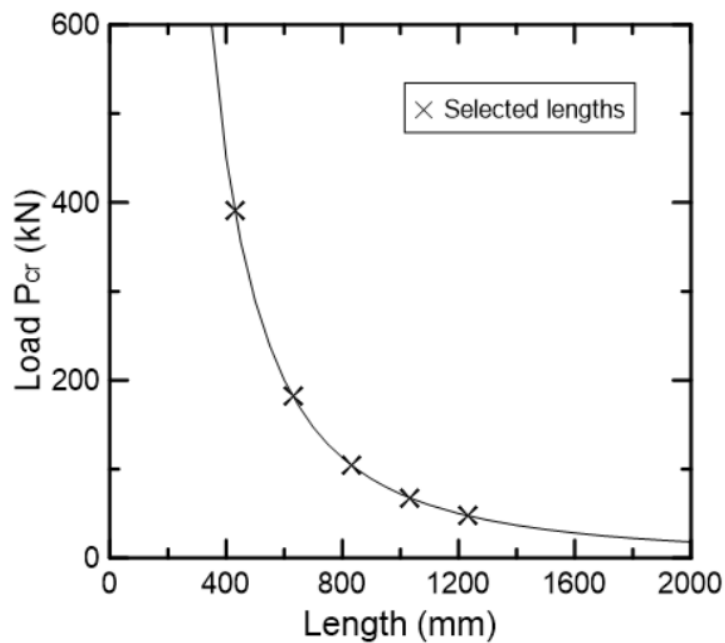
3.5. I-Section Column Tests

TRC I-section columns having different lengths were tested in compression to study the influence of slenderness on the global buckling behavior. All columns were considered as pinned about minor axis. Testing lengths were selected in order to ensure ‘pure’ global buckling, based on a signature curve analysis obtained using the software *GBTul 2.0*. The parameters adopted were: elastic modulus of 27.6 GPa (determined from the matrix compression test), poisson’s ratio of 0.2 and shear modulus of 11.5 GPa. Figure 3.17(a) presents the signature curve showing the local and global buckling modes and Figure 3.17(b) presents the curve with the chosen lengths. As can be seen, the selected lengths have global buckling critical loads much lower than local ones,

ensuring no interaction between the two buckling modes. Ten columns were tested, being two of each length: 40, 60, 80, 100 and 120 cm.



(a)



(b)

Figure 3.17 - Signature curve for I-section columns: (a) local and global buckling modes; (b) chosen lengths.

To reproduce the desired end conditions, each end was constituted by two components, presented in Figure 3.18. The first part consists in a square bar welded to a metal T-shape piece. The second is a base plate with a V-notch on one side and with 35-mm thick steel plates welded to it on the other side, these later used to allow centering the specimen as well as to avoid the uplifting or end

crushing. After clamping the T-shape stem to the machine grips, the second plate is positioned over the square bar in a way to fit it in the V-notch. The end fixtures were developed to allow rotation about minor axis of column. With both ends positioned, a polyester-based body filler (*Iberê*) was applied between the base plates and the column to ensure uniform loading and to fill in the gap of 3 mm between column and steel plates, as shown in Figure 3.19. The test was only started after the hardening of the material, approximately one hour after its application.

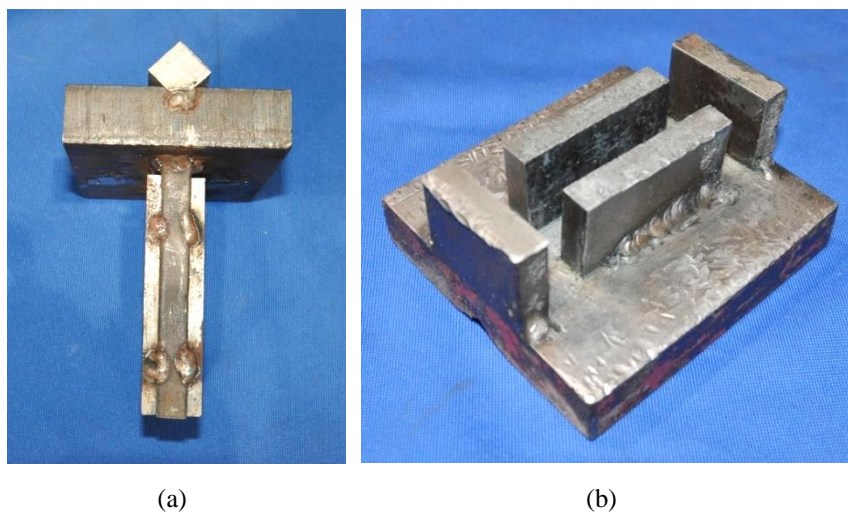


Figure 3.18 – I-section columns test set-up: (a) square bar welded to a metal T-shape piece; (b) base plate with 35-mm thick steel plates welded to it.



Figure 3.19 – Column being regularized with polyester-based body filler (*Iberê*).

The columns were instrumented with three displacement transducers, identified in Figure 3.20. Two of them were positioned at the mid-span of the flanges (maximum deflections expected) and the third transducer was positioned on the base plate in order to measure the axial shortening of column. All tests were conducted under displacement control at a rate of 0.3 mm/min until failure using a universal testing machine *MTS frame model 311.11*, with a load capacity of 1000 kN.

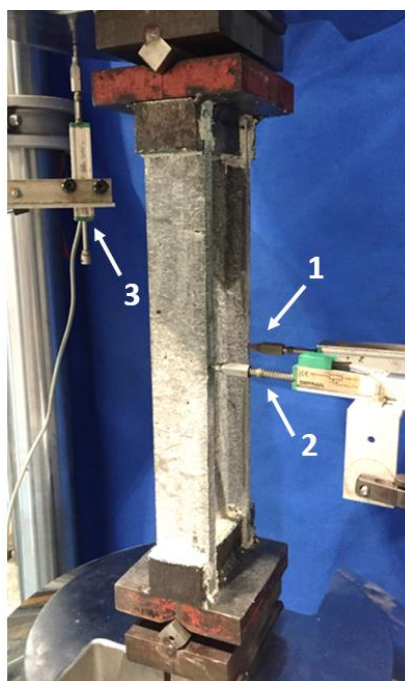


Figure 3.20 – I-section test fixture with the displacement transducers.

3.6. Rectangular Column Tests

Eight TRC rectangular columns were tested in compression to study the global buckling behavior, two of each length: 60, 80, 100 and 120 cm. These lengths were also determined based on the signature curve provided by *GBTul 2.0*, as shown in Figure 3.21.

In this case, all the columns were clamped at both ends. The test set-up was constituted only by the base plate with 35-mm thick steel plates welded to it, used for the I-section columns. The tests were performed on the *MTS frame model 311.11* with a displacement control at a rate of 0.1 mm/min until the composite

failure. The columns were instrumented with two displacement transducers, one positioned horizontally in the mid-length of the column, to measure lateral deflections, while another was disposed vertically to measure the shortening of the column. Figure 3.22 presents the test fixture showing the displacement transducers.

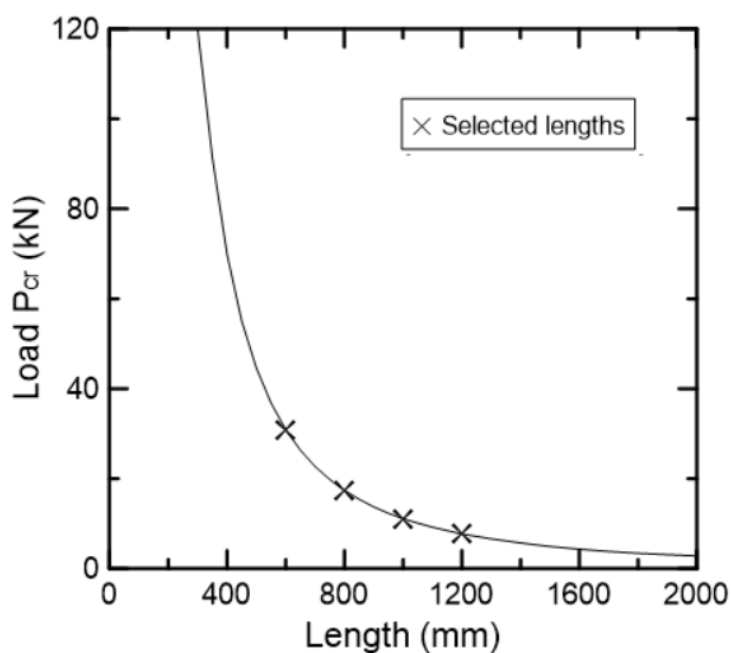


Figure 3.21 – Signature curve for the rectangular columns and the chosen lengths.

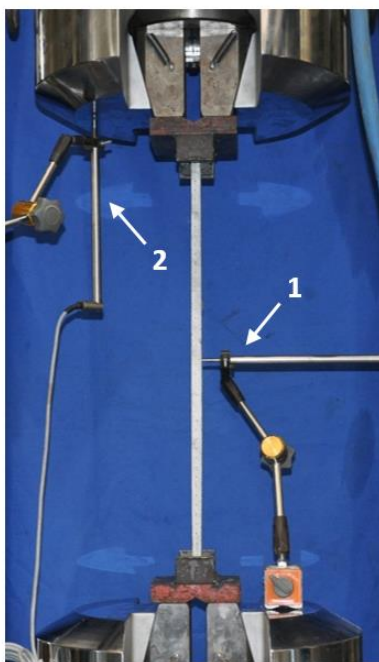


Figure 3.22 – Rectangular column test fixture with the displacement transducers.

4. Results Analysis

4.1. Overview

In this Chapter, the results from all the experimental tests are reported and discussed. With the material properties obtained from the mechanical characterization tests, axial force-moment-curvature models are proposed and compared to the results obtained from four-point bending tests, for validation. Then, a beam-column model using the method reported by Bazant and Cedolin [38] is developed and the results are compared to the load-deflection plots for rectangular and I-section columns tests. The theoretical and experimental results are compared and discussed.

4.2. Material Characterization

4.2.1. Carbon Yarn Uniaxial Tension Test

Stress-strain curves for both specimens are presented in Figure 4.1, along with the theoretical curve proposed by Eq. (2.9) presented in section 2.2.4.1. The tensile modulus of the fiber E_f was obtained as the slope of the linear portion between strains 0 and 3‰ of the stress-strain curve. Table 4.1 presents the tensile strength, f_f , and tensile modulus of elasticity of the fiber, E_f , for both yarns tested.

The negative values of strain at the beginning of the plot can be explained due to some flexure that occurred because of the adjustment of the fiber around the cylinder, since the strain gage was positioned in only one side of the specimen.

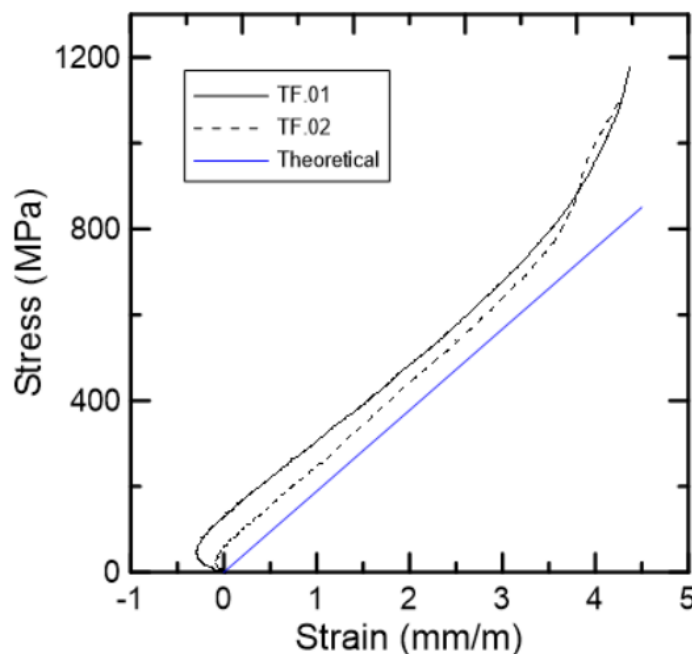


Figure 4.1 – Stress-strain curves of the carbon yarn uniaxial tension test.

Table 4.1 – Tensile strength f_f and tensile moduli of elasticity E_f of the fiber yarn specimens.

Specimen	f_f (MPa)	E_f (GPa)
TF01	1180	184
TF02	1100	194
Average	1140	189

4.2.2. Matrix Compression Test

The compressive strength of concrete f_c was calculated by dividing the maximum load attained during the test by the cross-sectional area of the specimen and the compressive modulus of elasticity of concrete E_c was obtained as the slope of the linear portion of the stress-strain curve. Stress-strain curves are presented in Figure 4.2, along with the theoretical curve proposed by Eq. (2.8) presented in section 2.2.4.1, and the results are given in Table 4.2.

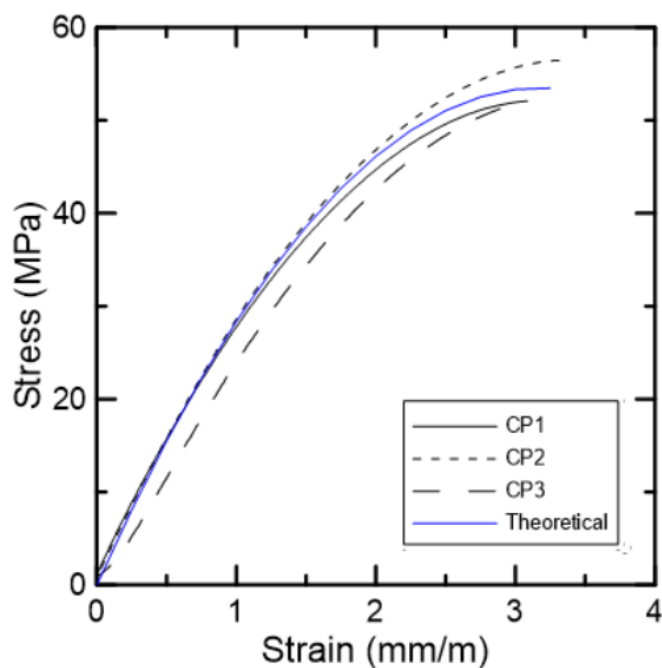


Figure 4.2 – Stress-strain curves of each specimen of the matrix compression test.

Table 4.2 – Compressive strength f_c , compressive modulus E_c and strain of concrete at compressive stress peak ϵ_{c2} of the specimens.

Specimen	f_c (MPa)	E_c (GPa)	ϵ_{c2} (‰)
CP1	52.1	29.9	3.09
CP2	56.5	29.8	3.32
CP3	51.8	23.0	3.13
Average	53.5 ± 2.63	27.6 ± 3.96	3.18 ± 0.123
cov ⁽¹⁾	0.0492	0.143	0.0387

⁽¹⁾ Coefficient of variation

4.2.3. Combined Loading Compression Test

Six specimens were tested to study the influence of fiber in the compressive strength of the composite. Their external dimensions – thickness t , width b and length L – were measured with a digital caliper and cataloged. Three measures of each specimen were obtained for t and b . The average dimensions (\pm one standard deviation) of each specimen are presented in Table 4.3, along with the respective percentage of fiber – obtained from the number of yarns in the mid-span of each specimen (1.84% and 3.69% for one and two yarns, respectively).

Table 4.3 – Dimensions and fiber percentage of CLC specimens.

Specimen	t (mm)	b (mm)	L (mm)	Fiber (%)
CLC01	11.9 ± 0.361	16.4 ± 0.122	155.2	3.69
CLC02	11.9 ± 0.500	14.4 ± 0.0707	155.6	1.84
CLC03	11.9 ± 0.361	15.4 ± 0.604	153.8	3.69
CLC04	11.6 ± 0.141	15.0 ± 0.803	155.8	1.84
CLC05	12.0 ± 0.100	14.7 ± 0.552	155.1	1.84
CLC06	11.8 ± 0.224	16.1 ± 0.557	154.3	3.69

According to the adopted standard, failure is acceptable if it occurs within the gage length, which occurred in all the tested specimens. Figure 4.3 shows the failure within the gage length for specimens CLC03 and CLC04.

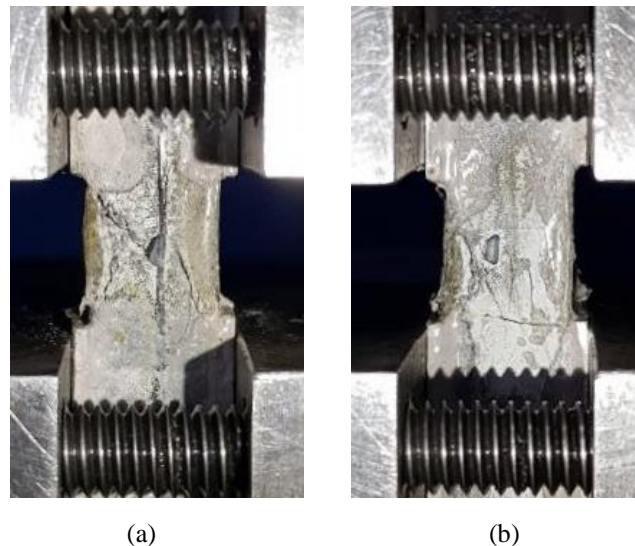


Figure 4.3 - Failure within the gage length: (a) CLC03; (b) CLC04.

The longitudinal compressive modulus of elasticity of TRC $E_{L,c}$ for each specimen was obtained as the slope of the plot of axial stress *versus* measured average strain. The compressive strength of TRC $f_{L,c}$ was determined by dividing the maximum load attained by the cross-sectional area of the specimen.

No work on CLC tests made of cementitious matrix was found in the database consulted. It is extremely hard to perform CLC tests on this material because significant variations in thickness may result in damage during the application of torque. Presence of damage, as well as inherent inhomogeneity of concrete material may result in non-uniform stress distribution and, therefore, in

different readings for strain gages. This problem was, in fact, observed in three specimens (CLC02, CLC04 and CLC05). For these samples, only strength values are reported.

Figure 4.4 presents the stress-strain curves for specimens CLC01, CLC03 and CLC06. The compressive modulus and compressive strength of TRC for the specimens with 3.69 and 1.84% of fiber content are presented in Table 4.4 and Table 4.5, respectively.

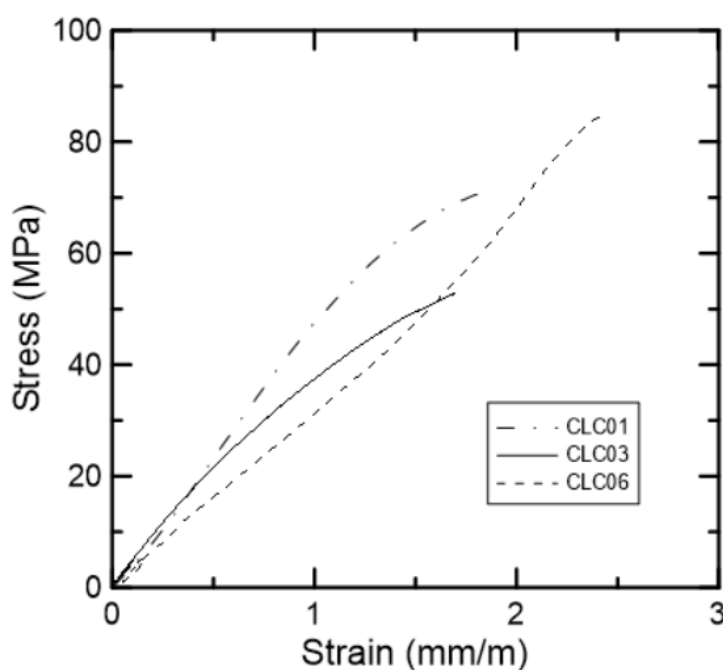


Figure 4.4 – Stress-strain curves of the combined loading compression test.

Table 4.4 – Compressive strength $f_{L,c}$ and longitudinal compressive modulus $E_{L,c}$ of the TRC specimens with 3.69% of fiber content.

Specimen	$f_{L,c}$ (MPa)	$E_{L,c}$ (GPa)
CLC01	76.1	42.4
CLC03	53.6	29.6
CLC06	84.5	31.8
Average	71.4 ± 16.0	34.6 ± 6.84
cov ⁽¹⁾	0.224	0.198

⁽¹⁾ Coefficient of variation

Table 4.5 – Compressive strength $f_{L,c}$ and longitudinal compressive modulus $E_{L,c}$ of the TRC specimens with 1.84% of fiber content.

Specimen	$f_{L,c}$ (MPa)	$E_{L,c}$ (GPa)
CLC02	63.1	-
CLC04	66.4	-
CLC05	48.5	-
Average	59.3 ± 9.53	-
cov ⁽¹⁾	0.161	-

⁽¹⁾ Coefficient of variation

Even though the values obtained for the TRC compressive strength were higher than the one obtained for the compressive strength of concrete, more tests must be done in order to guarantee the consideration of the contribution of the fiber in compressed TRC members. Nevertheless, it is possible to estimate the fiber contribution on the compressive strength of TRC considering a perfect bond between matrix and reinforcement. It is important to notice that no textile buckling was observed during test. This contribution is obtained by multiplying the strain by the fiber modulus of elasticity and fiber percentage. Figure 4.5 presents the stress-strain curve for CLC01 showing the fiber and matrix contribution.

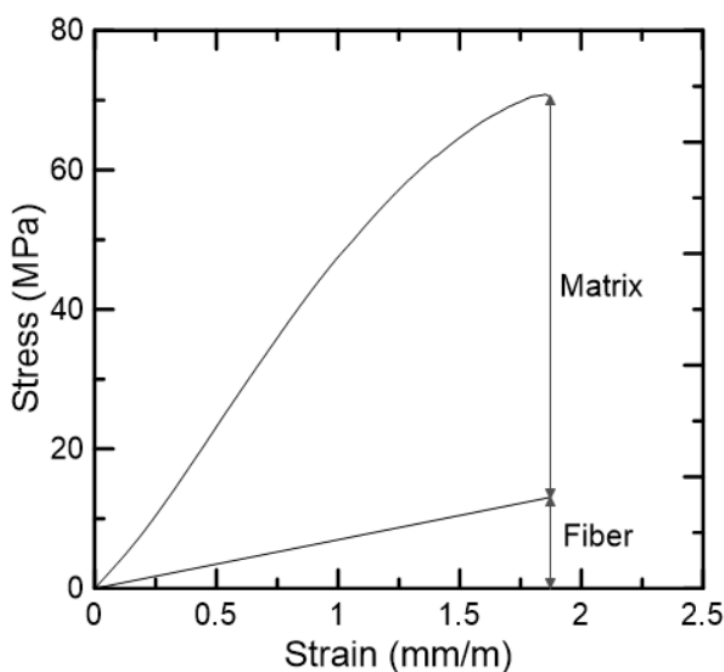


Figure 4.5 – Stress-strain curve for CLC01 showing the fiber and matrix contribution.

4.2.4. Four-point Bending Tests

Due to the molding process adopted for the plates, it was very difficult to keep the textile in place, despite all the efforts in this direction. It was intended to place the textile closer to the tensioned face, respecting a 3 mm concrete cover. However, the concrete used was fluid and the fiber is flexible, resulting in the uplift of textile. Since the plates are very thin, small variation on the textile position can contribute to large changes on the experimental results. To determine the actual conditions, plates were cut at mid-length after the end of the tests and average dimensions (\pm one standard deviation) and position of yarns were measured with a digital caliper, as presented in Table 4.6. Four measures of each specimen thickness t were obtained. The positions reported in the Table correspond to an arithmetic average between distances measured for each yarn across the cut section, as shown in Figure 4.6.

Table 4.6 – Dimension of plates.

Plate	b (mm)	t (mm)	L (mm)	Distance from the bottom to the textile axis (mm)
FP2A	120	10.5 ± 0.424	1000	5.80 ± 0.681
FP2B	120	13.6 ± 0.588	1000	8.20 ± 1.39
FP3A	120	11.5 ± 0.802	1000	6.20 ± 0.598

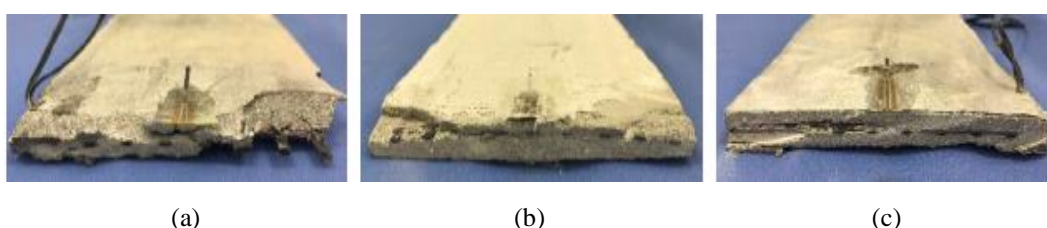


Figure 4.6 – Textile position at the mid-length of plates: (a) FP2A; (b) FP2B; (c) FP3A.

As stated before, an analytical model able to predict non-linear axial force-moment-curvature relationships was implemented in *Maple 2015 software* [48]. The routine included the equations presented in section 2.2.4.1, using the material properties obtained experimentally from the characterization tests and cross-section parameters presented in Table 4.6.

The force-displacement plot for the three plates tested is presented in Figure 4.7 and was obtained from the displacement measured by the displacement transducer. Despite the similar setup configuration adopted, the results between the plates were slightly different due to differences in the thickness and position of the fibers along length. The failure loads were 879, 1105 and 968 N, respectively for the FP2A, FP2B and FP3A plates.

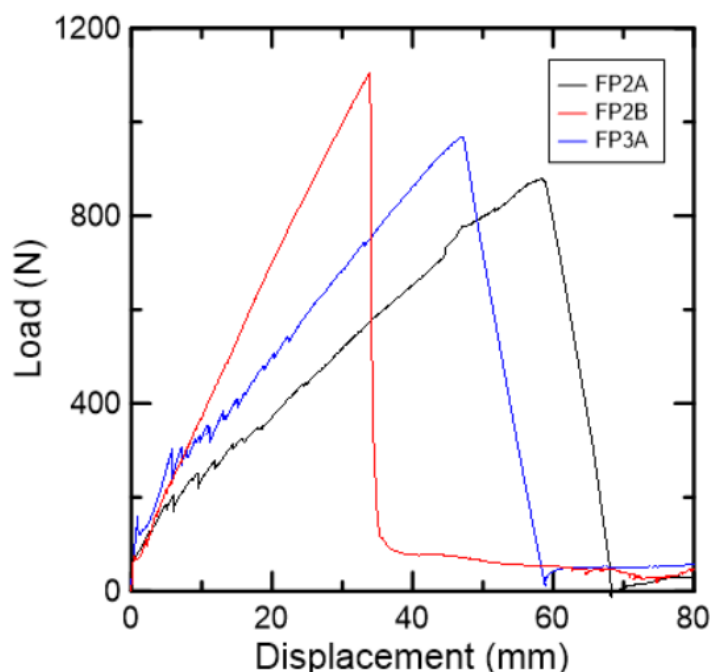
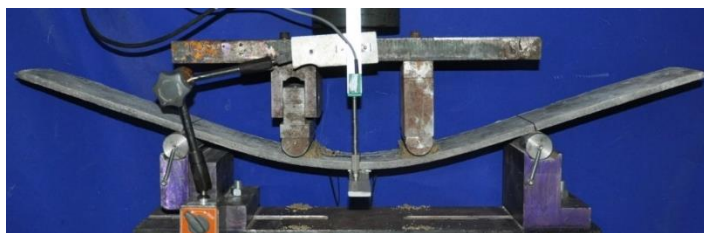


Figure 4.7 – Experimental load-displacement curves for each plate.

The typical failure mode observed on the tested plates is shown in Figure 4.8, which presents the exact moment before (a) and after (b) the failure of FP2A.

The experimental and theoretical moment-curvature plots are presented in Figure 4.9, up to a curvature equal to 1.0 m^{-1} , corresponding to a displacement of 26.6 mm. The experimental curves were obtained using the equations of the elastic line, since the deformations obtained by the strain gages positioned on the fiber indicated small deformations, which may be associated to the stiffening effect due to the concrete contribution, *i.e.*, tension stiffening [18]. Meanwhile, the theoretical moment-curvature diagrams, also presented in Figure 4.9, were obtained using the analytical model described previously.



(a)



(b)

Figure 4.8 – Four-point bending test of FP2A: (a) before failure; (b) after failure.

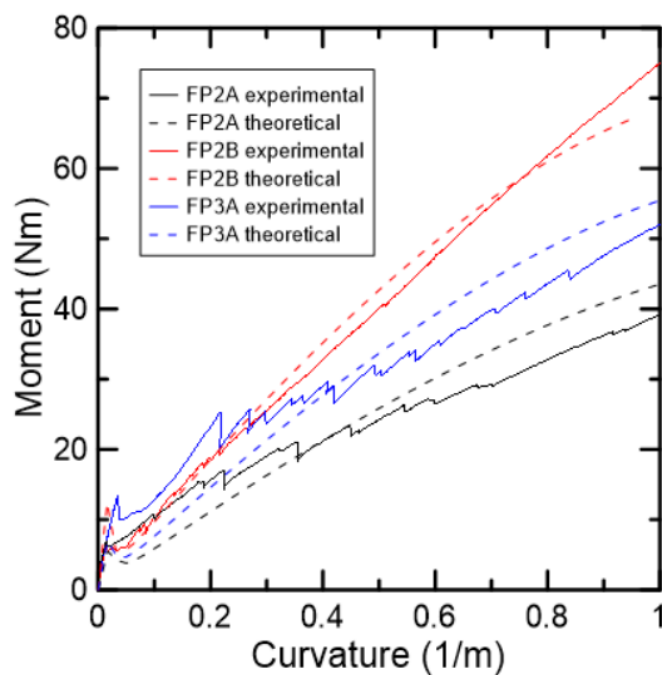


Figure 4.9 – Experimental and theoretical moment-curvature curves for each plate.

The theoretical curves present a similar behavior of a reinforced concrete element, with an initial peak moment and then a sudden fall when the first crack appears. The experimental curves present the already expected behavior of the formation of multiple cracking, which is not represented by the analytical model. Despite these differences between the theoretical and experimental curves, they presented a resembling behavior reaching similar moments for the corresponding

curvatures. Therefore, the proposed analytical model can be considerate satisfactory.

Flexural tensile strength f_{ctf} of matrix was estimated from the experimental curve peak, which corresponds to the first crack, shown in Figure 4.10. It is given by Eq. (4.1), assuming neutral axis at mid-depth of cross section.

$$f_{ctf} = \frac{My}{I} = M \frac{h}{2} \frac{12}{bh^3} = \frac{6M}{bh^2} \quad (4.1)$$

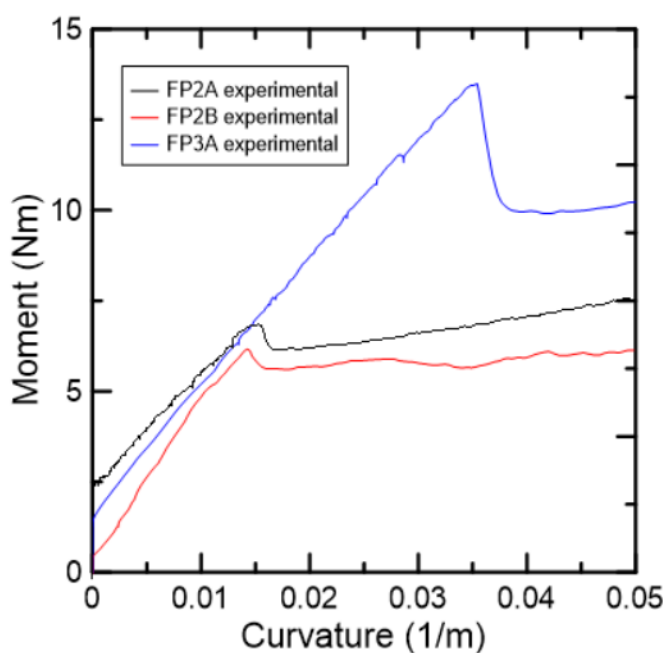


Figure 4.10 – Beginning of the experimental moment-curvature curves.

Table 4.7 presents the moment values and flexural tensile strengths of each plate tested. The measured average flexural tensile strength was 3.29 MPa, with a coefficient of variation greater than 50%.

Table 4.7 – Flexural tensile strength f_{ctf} of concrete.

Specimen	M (Nm)	f_{ctf} (MPa)
FP2A	6.83	3.10
FP2B	6.17	1.66
FP3A	13.5	5.10
Average	-	3.29 ± 1.73
cov ⁽¹⁾	-	0.526

(1) Coefficient of variation

Even though the tensile strength of concrete f_{ct} depends on the cross-sectional geometry and the type of test performed [49], the value of f_{ct} considered in this study for the axial force-moment-curvature and beam-column models was the flexural tensile strength f_{ctf} .

4.3. Rectangular Column Tests

Three measurements of each column thickness t and width b were obtained with a digital caliper. The average dimensions (\pm one standard deviation) are presented in Table 4.8, along with the column lengths.

Table 4.8 – Lengths and average dimensions of each rectangular column.

Column	L (cm)	b (mm)	t (mm)
PA.60.01	60.0	68.9 ± 0.587	13.4 ± 0.889
PA.60.02	60.1	68.8 ± 1.79	11.9 ± 0.711
PA.80.01	80.0	70.0 ± 0.0707	12.3 ± 0.851
PA.80.02	80.1	69.0 ± 0.711	12.3 ± 0.800
PA.100.01	100.0	69.9 ± 2.06	11.8 ± 1.27
PA.100.02	100.1	69.4 ± 1.00	12.0 ± 0.579
PA.120.01	120.1	69.8 ± 0.608	11.8 ± 0.794
PA.120.02	120.1	69.1 ± 0.265	11.6 ± 0.682

An overview of all column lengths tested is shown in Figure 4.11. It can be observed that the fixture adopted satisfactorily restrained the rotation at ends.

After the removal of the columns from the machine, the cracks were observed with the aid of a magnifying glass. One of the main characteristics of carbon TRC subjected to bending is the formation of multiple cracking along the length [50], which are difficult to see when the specimen returns to its initial state. Therefore, in the 60 and 80 cm columns, no cracks were observed as they had presented smaller deflections. In the 100 and 120 cm columns, a crack was observed in the mid-length and some cracks were observed close to the column's ends. Figure 4.12 shows the cracks observed in columns PA.100.02.

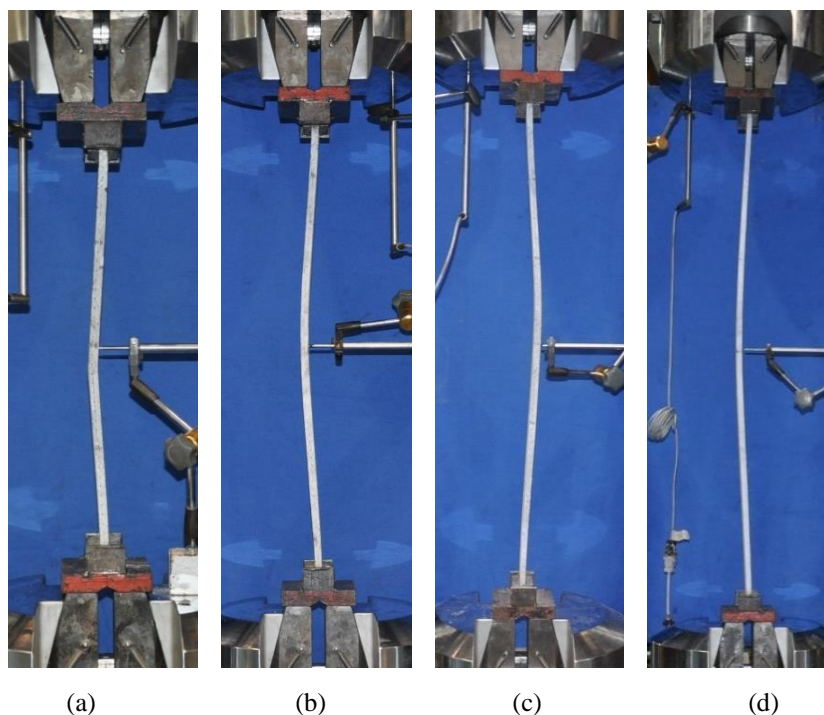


Figure 4.11 – Overview of failure of columns: (a) PA.60.02; (b) PA.80.01; (c) PA.100.01; (d) PA.120.01.



Figure 4.12 – Cracks in columns PA.100.02: (a) close to the column's end; (b) mid-length.

Figure 4.13 presents the experimental curves for the compression load P versus lateral deflections δ . According to theory, the largest loads occur for the smallest lengths and the largest displacements occur for the greatest lengths, which is coherent with the results obtained in Figure 4.13, except for PA.80.02. This column was not perfectly clamped, probably because test was carried out before the polyester-based body filler had set, resulting in a soft mixture that was not able to restrain the rotation, as shown in Figure 4.14, reaching lower loads and higher deflections than expected. It can be seen in Figure 4.13 that columns PA.60.01, PA.60.02, PA.80.01 and PA.100.01 had smaller imperfections, due to

the greater slope in the initial part of the curve, showing a behavior closer from the perfect column behavior.

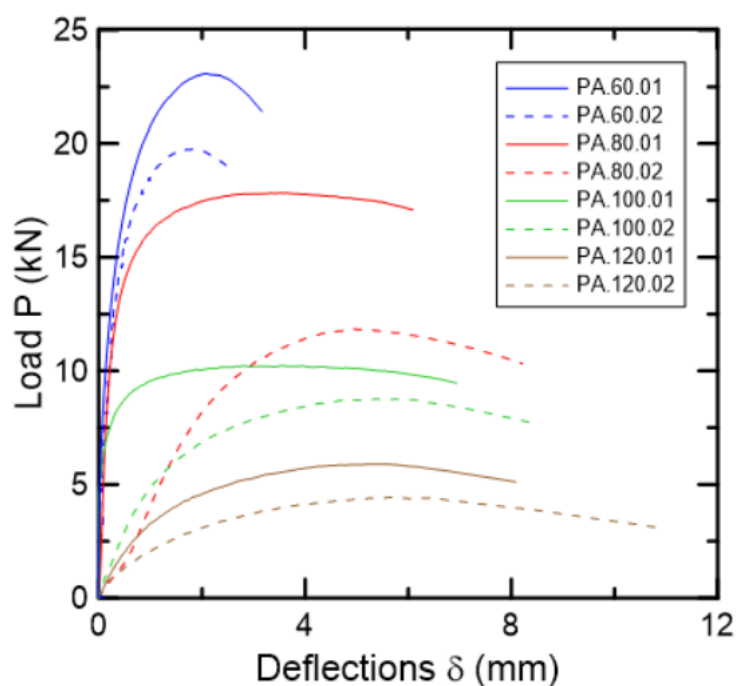


Figure 4.13 – Load-deflections plots for the eight columns tested.

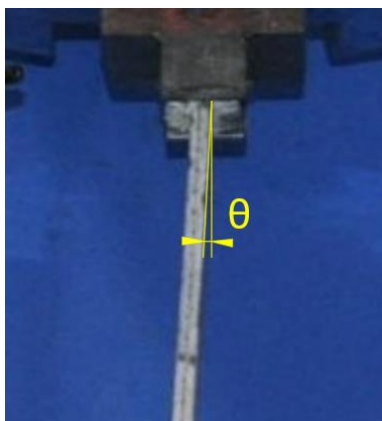


Figure 4.14 – Rotation θ of column PA.80.02.

Figure 4.15 presents a plot of applied load P versus out-of-plane deflections δ for column PA.120.01, showing its displacement growth. A 120-cm column was chosen in this case because its deflections were higher (approximately 1 cm) compared to the ones of other columns lengths and easier to notice in a photo sequence.

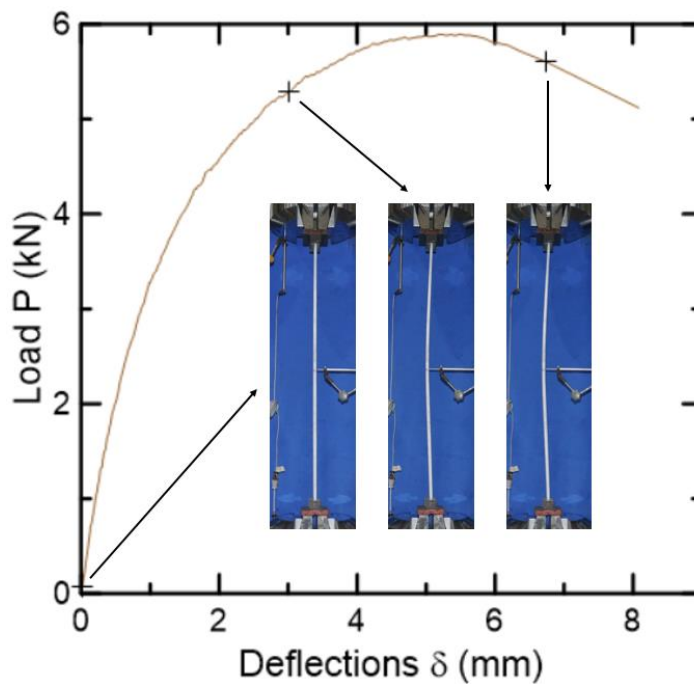


Figure 4.15 – Displacement growth of column PA.120.01.

Figure 4.16 illustrates a representative plot of the experimental curve for the compression load P versus shortening δ_s of column PA.80.01. As can be seen, the plot can be divided in three states. In the first state, state I, there is an accommodation of the column on the setup, represented by this curved portion of curve at the beginning. State II consists on the straight line of the plot, for which load increased linearly with shortening. Finally, state III is characterized by the curved line at the end of the plot. At this stage, significant lateral deflections occur associated with the beginning of the change in the state of equilibrium. Appendix B presents the plots for all tested columns.

Although the external dimensions of the columns were measured, it is very difficult to measure the total imperfection of each column, which included loading eccentricity, misalignment of fiber, variation of thickness and out-of-straightness. Therefore, the apparent initial imperfection of each column was obtained using Southwell plot and the results are presented in Table 4.9 (page 80). Figure 4.17 presents the Southwell plot of column PA.60.01. Southwell plot is nonlinear and fitting a straight line is a difficult task. The plots for the eight tested columns are shown in Appendix B.

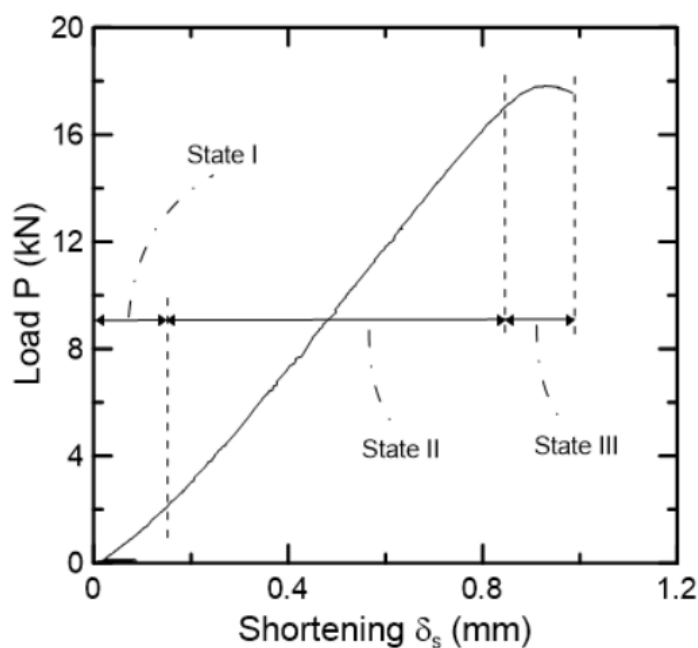


Figure 4.16 – Representative plot of load *versus* shortening of column PA.80.01.

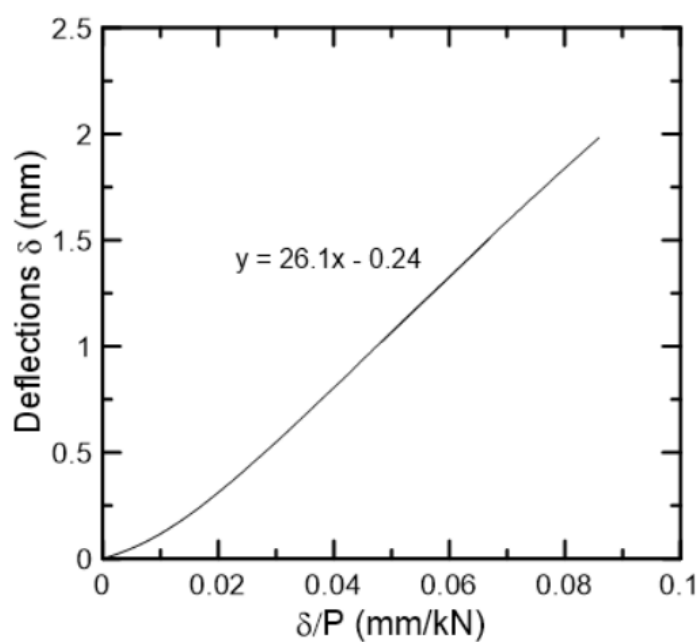


Figure 4.17 – Southwell plot of column PA.60.01.

In order to compare the values obtained from the Southwell plots, a beam-column analytical model was developed in *Maple* software using the method described by Bazant and Cedolin [38] and theoretical force-displacement plots were obtained for each length tested. As these tests were made with clamped columns, the equations presented in section 2.2.4.3 were slightly modified and are given in Eqs (4.2) to (4.5).

$$\delta = \delta_1 \sin^2(\pi x / L) \quad (4.2)$$

$$\Phi = 2\delta_1 (\pi / L)^2 (1 - 2\sin^2(\pi x / L)) \quad (4.3)$$

$$\delta_1 = \Phi \left(\frac{L}{\sqrt{2\pi}} \right)^2 \quad (4.4)$$

$$\delta_1 + \delta_0 = \frac{2M}{N} \quad (4.5)$$

Each experimental column behavior was represented by one theoretical curve. To develop this curve, an initial imperfection was selected in order to obtain a plot that best suited the initial part of the experimental curve, ranging from zero until 40% of the experimental maximum load.

On the theoretical model, the peak load is highly influenced by the tensile strength of concrete. The column maximum load occurs when the strain in the most tensioned fiber exceeds the value of f_{ct}/E_c , *i.e.* when the first concrete crack is formed. Therefore, the lowest and highest values of tensile strength of concrete obtained from the four-point bending tests were used as failure limits, represented in Figure 4.18 as “inf” (1.66 MPa) and “sup” (5.10 MPa). Figure 4.18 presents the experimental and theoretical plots for each length tested.

All theoretical curves represented well the behavior of the experimental curves until the value of 40% of the experimental maximum load. Columns PA.60.01, PA.100.02, PA.120.01 and PA.120.02 showed a good agreement with the theoretical curves until the theoretical failure of columns. PA.60.02 and PA.100.01 reached a maximum load lower than expected, which may be explained by premature cracking associated to variations in concrete tensile strength as well as by deviations in modulus of elasticity. PA.80.01 reached a higher load and, once more, it may be explained by deviations in modulus of elasticity. Although column PA.80.02 exhibited rotation at the supports (Figure 4.14), a parallel theoretical curve was developed with a similar behavior. In addition, except for the 60-cm long columns, all columns failed after the theoretical prediction, indicating a greater apparent tensile strength of concrete.

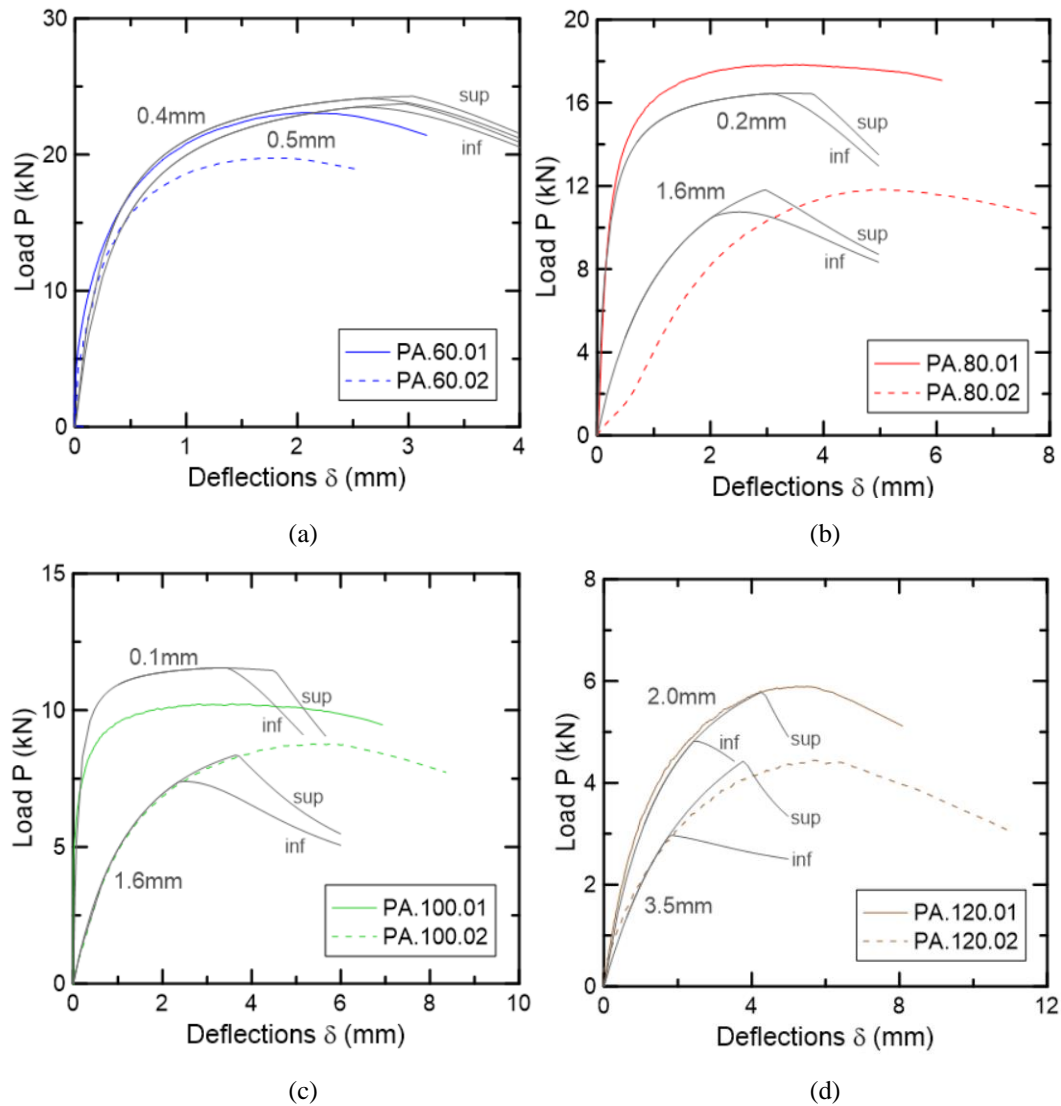


Figure 4.18 – Experimental and theoretical plots for each length tested: (a) 60 cm; (b) 80 cm; (c) 100 cm; (d) 120 cm.

As already explained, the numerical model adopted is a simpler alternative resulting in a single DOF model. This model only considers what happens in the cross-section with the increase in the load P and does not account for tension stiffening effect. Therefore, the behavior can be explained by the combination of two distinct $P\delta$ curves. The first, due to the instability effect, was obtained from Eq. (4.6). The second, corresponding to the load P necessary to form a crack, *i.e.* a stress equal to f_{ct} in the tension face, was obtained through Eq. (4.7). Figure 4.19 represents both curves for column PA.100.02, considering two values of f_{ct} (1.66 and 5.10 MPa).

$$\delta = \frac{\delta_0}{\frac{P_{cr}}{P} - 1} \quad (4.6)$$

$$\frac{P}{A} - \frac{P}{S} \frac{(\delta + \delta_0)}{2} = -f_{ct} \quad (4.7)$$

where S is the section modulus and number 2 in Eq. (4.7) comes from the clamped end condition.

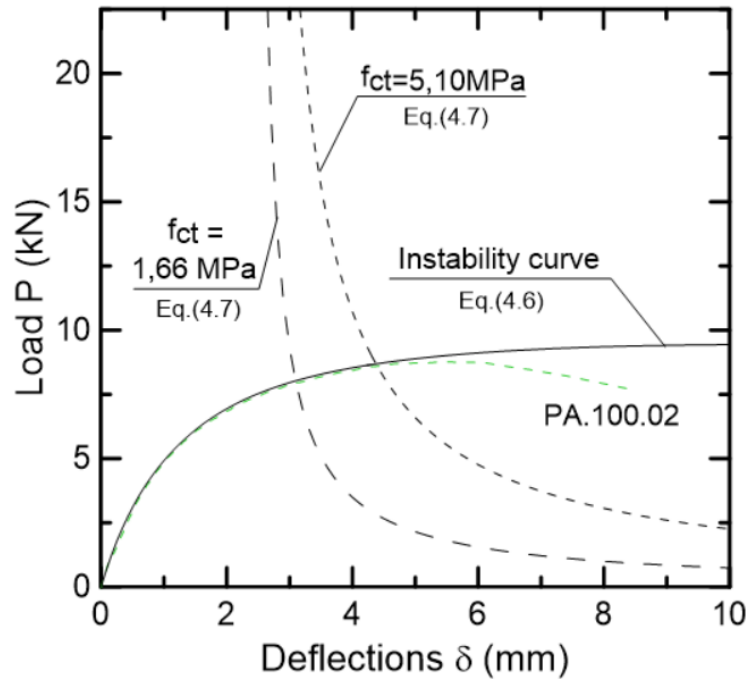


Figure 4.19 – $P\delta$ curves from PA.100.02 with δ_0 equal to 1.6mm: instability and tensile strength curves.

The initial imperfections obtained from the Southwell plots and the theoretical curves are presented in Table 4.9, along with the imperfection limits ($L/500$) for each length. As it can be seen, the results between the Southwell plots and the theoretical curves are of the same order of magnitude. Concerning the imperfection limits, only column PA.120.02 had a higher imperfection obtained from the theoretical curve.

Table 4.9 – Initial imperfections of columns by Southwell plot, theoretical curve and the imperfection limits.

Column	Initial imperfections (mm)		
	Southwell Plot	Theoretical Curve	Limit L/500
PA.60.01	0.24	0.40	1.20
PA.60.02	0.24	0.50	
PA.80.01	0.18	0.20	1.60
PA.80.02	1.65 (rotated)	1.60	
PA.100.01	0.07	0.10	2.00
PA.100.02	1.37	1.60	
PA.120.01	1.38	2.00	2.40
PA.120.02	1.99	3.50	

The experimental and theoretical maximum loads obtained for each column are presented in Table 4.10. Good agreement achieved leads to the conclusion that the maximum loads of these columns can be predicted adequately determine using numerical method adopted.

Table 4.10 – Experimental and theoretical maximum loads.

Column	Maximum loads (kN)	
	Experimental	Theoretical
PA.60.01	23.1	$24.1 \leq P_{\max} \leq 24.3$
PA.60.02	19.7	$23.5 \leq P_{\max} \leq 23.7$
PA.80.01	17.3	$16.4 \leq P_{\max} \leq 16.5$
PA.80.02	11.8	$10.7 \leq P_{\max} \leq 11.8$
PA.100.01	10.2	11.5
PA.100.02	8.76	$7.39 \leq P_{\max} \leq 8.35$
PA.120.01	5.90	$4.82 \leq P_{\max} \leq 5.78$
PA.120.02	4.44	$2.97 \leq P_{\max} \leq 4.43$

Figure 4.20 shows a normalized compressive strength curve for perfect columns with the experimental results for all analyzed eight columns. The critical loads used to obtain the values for the experimental non-dimensional slenderness

were obtained through the *GBTul* software and are presented in Table 4.11. As it can be seen, the 60-cm long columns have their non-dimensional slenderness closer to 1, value that marks the transition point between global buckling and crushing. Thus, an interaction between these individual modes may occur. The rest of the columns have higher slenderness and failed only by global buckling.

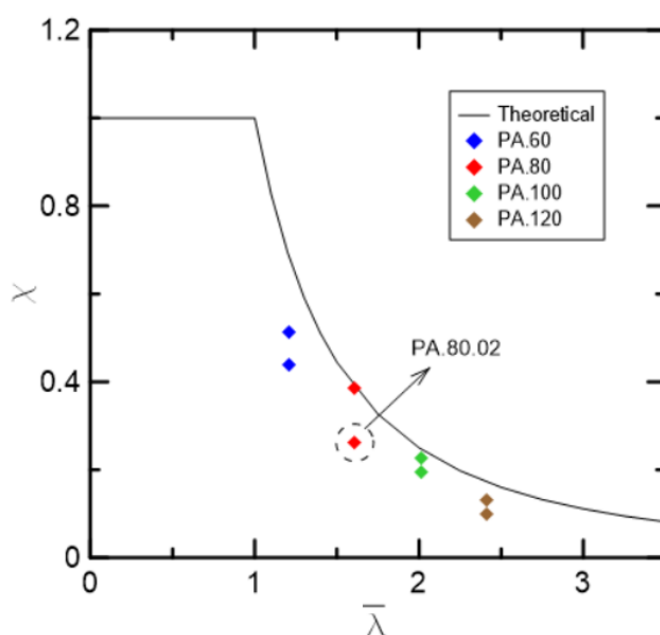


Figure 4.20 – Strength curve and experimental points.

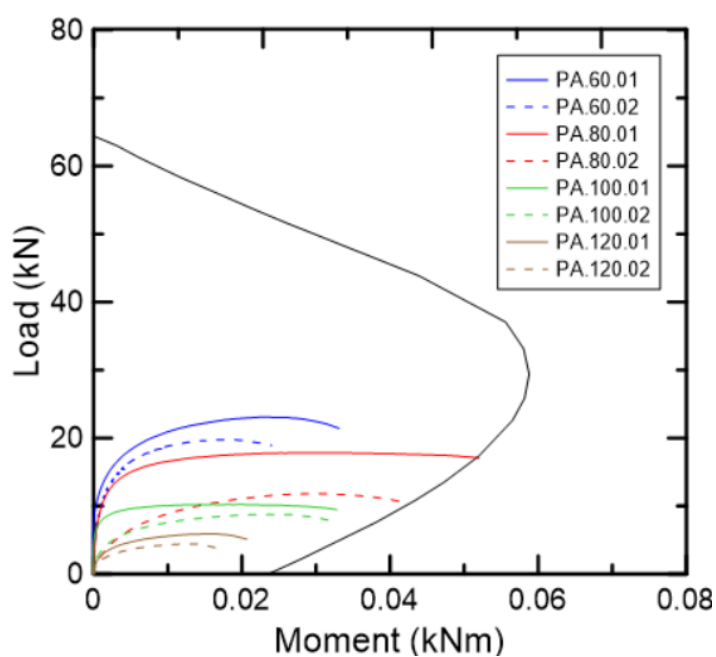


Figure 4.21 – Interaction diagram and experimental load-moment curves.

The global buckling behavior is also shown in Figure 4.21, which presents the interaction diagram for the studied section. It can be noticed that all columns reached a deflection where the value of the $\partial M / \partial P$ approaches infinity, as explained in section 2.2.3.3, and exhibited stability failure.

Table 4.11 presents the relationship between the experimental non-dimensional slenderness $\bar{\lambda}_{\text{exp}}$ and the theoretical one $\bar{\lambda}_{\text{theor}}$ for each column obtained from the strength curve, along with the critical loads obtained through the *GBTul* software. As it can be observed, the higher results happened for columns with lower initial imperfections: PA.80.01 and PA.100.01. PA.80.02 exhibited poor capacity with apparent large erosion due to the rotation of column explained previously. PA.120.02 obtained the lowest percentage due to the initial imperfection higher than the one established as a limit ($L/500$). PA.100.02 and PA.120.01 also had high initial imperfections and, for these very slender columns, the maximum load is reduced by the amplified bending moment caused by lateral deflection, attributed to the second-order effect. Additionally, they suffer loss of stability still far from the critical load, which may be associated with cracking that reduces the columns stiffness.

Table 4.11 – Critical loads and relationship between experimental and theoretical non-dimensional slenderness obtained from the strength curve.

Column	P_{cr} (kN)	$(\bar{\lambda}_{\text{exp}} / \bar{\lambda}_{\text{theor}})$ (%)
PA.60.01	30.9	74.8
PA.60.02		63.8
PA.80.01	17.4	99.4
PA.80.02		67.8
PA.100.01	11.1	91.9
PA.100.02		78.9
PA.120.01	7.71	76.5
PA.120.02		57.6

4.4. I-Section Column Tests

Four measurements of the web and flange thicknesses, t_w and t_f respectively, for the ten columns tested were taken with a digital caliper and their averages dimensions (\pm one standard deviation) are presented in Table 4.12, along with the column lengths. The flange width, b_f , and section depth, d , are 50 and 100 mm, respectively, for all columns. The I-section scheme is shown in Figure 4.22.

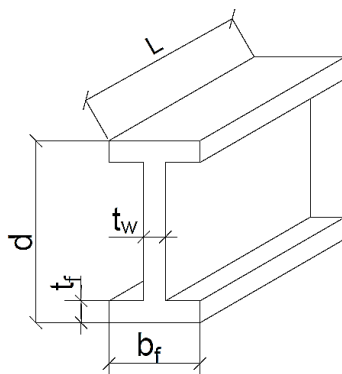


Figure 4.22 – I-section scheme.

Table 4.12 – Lengths and average cross-section dimensions of each I-section column.

Column	L (cm)	t_f (mm)	t_w (mm)
PI.40.01	40.2	12.9 ± 0.361	12.6 ± 2.26
PI.40.02	40.1	12.8 ± 0.614	13.4 ± 1.49
PI.60.01	59.9	12.9 ± 0.224	11.8 ± 0.921
PI.60.02	60.1	12.8 ± 0.153	12.0 ± 0.500
PI.80.01	79.9	12.9 ± 0.337	11.4 ± 0.283
PI.80.02	80.0	13.1 ± 0.300	11.8 ± 0.224
PI.100.01	100.0	12.7 ± 0.141	12.3 ± 1.20
PI.100.02	100.0	12.8 ± 0.224	11.4 ± 0.848
PI.120.01	120.0	12.8 ± 0.216	11.3 ± 0.100
PI.120.02	120.1	12.7 ± 0.440	11.4 ± 0.141

Figure 4.23 illustrates an overview of the typical failures modes for each column length tested.

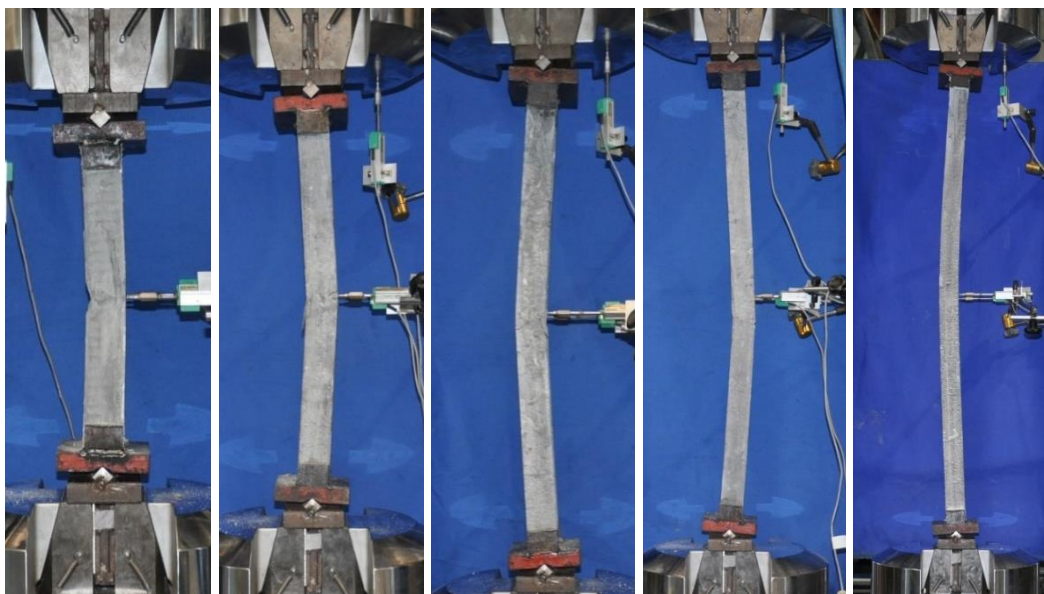


Figure 4.23 – Overview failure of columns: (a) PI.40.02; (b) PI.60.02; (c) PI.80.01; (d) PI.100.01; (e) PI.120.02.

The experimental curves for the compression load P versus out-of-plane deflections δ for all columns tested are presented in Figure 4.24. Column PI.40.02 did not have the expected behavior, which will be explained later.

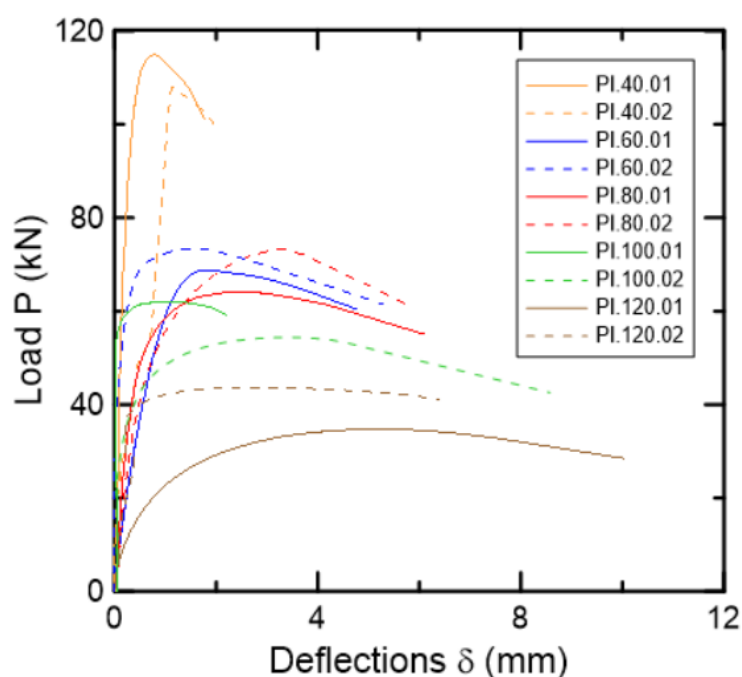


Figure 4.24 – Load-deflections plots for all columns tested.

Figure 4.25 present the displacement growth of column PI.120.01 on the plot load P versus out-of-plane deflections δ .

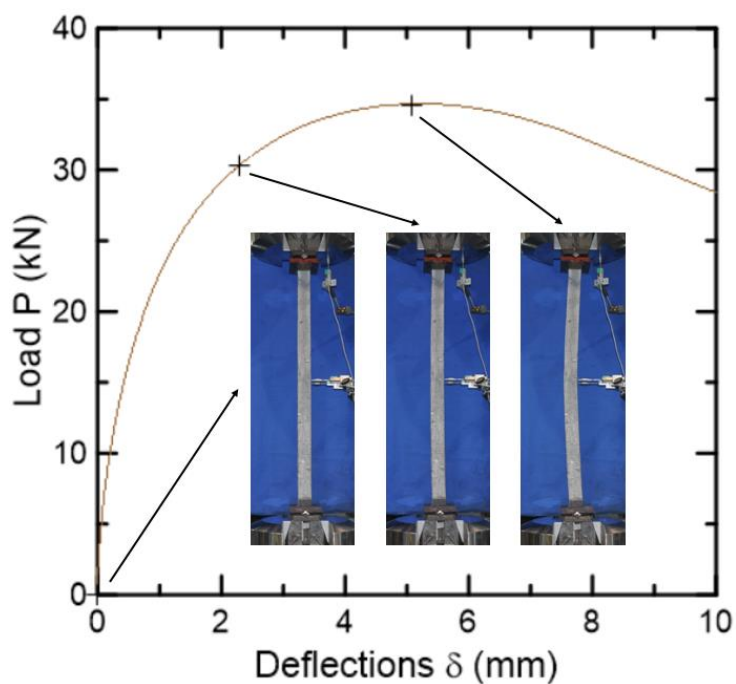


Figure 4.25 – Displacement growth of column PI.120.01.

Figure 4.26 illustrates a representative plot of the experimental curve for the compression load P versus shortening δ_s of column PI.100.01. As can be seen, the plot can be divided in three states, as explained in section 4.4. The plots for all tested columns are presented in Appendix C.

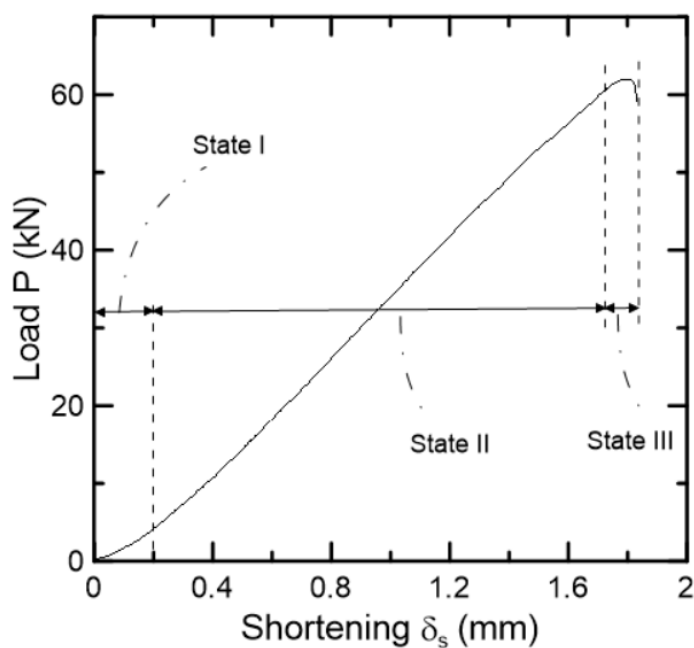


Figure 4.26 – Representative plot of load versus axial shortening of column PI.100.01.

For the I-section columns is even harder to obtain the total imperfection of each column. The misalignment of fibers inside the constituent walls does not play an important role in this case, but loading eccentricity usually increases with section size, despite the efforts in centering and aligning the specimen [36]. Table 4.13 (page 90) presents the initial imperfection of each column obtained with the Southwell plot and Figure 4.27 presents the Southwell plot of column PI.120.01. All the plots for the tested I-section columns are shown in Appendix C.

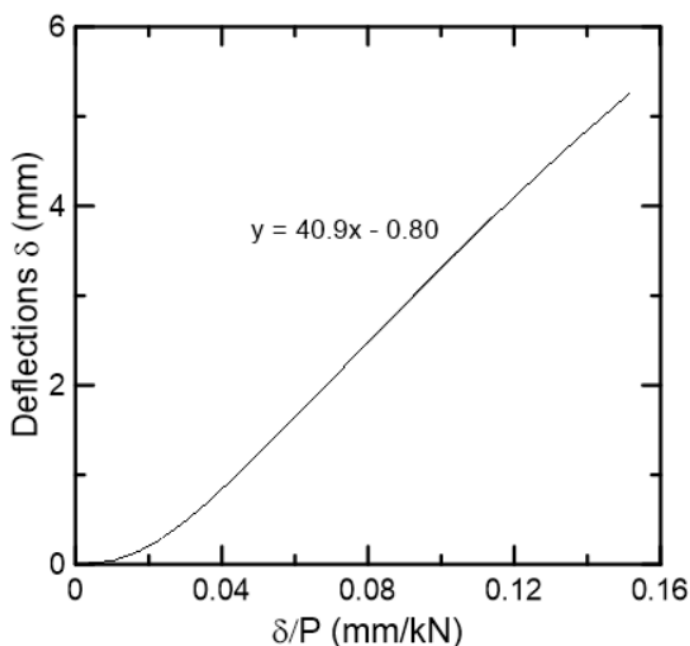


Figure 4.27 – Representative Southwell plot of column PI.120.01.

The theoretical force-displacement plots obtained from the equations presented in section 2.2.4.3 are presented in Figure 4.28, along with the experimental results. As explained before, a theoretical curve that best suited the initial part of the experimental curve, from zero to 40% of the experimental maximum load, represented each experimental behavior. In addition, the failure limits of tensile strength of concrete used are represented as “inf” (1.66 MPa) and “sup” (5.10 MPa).

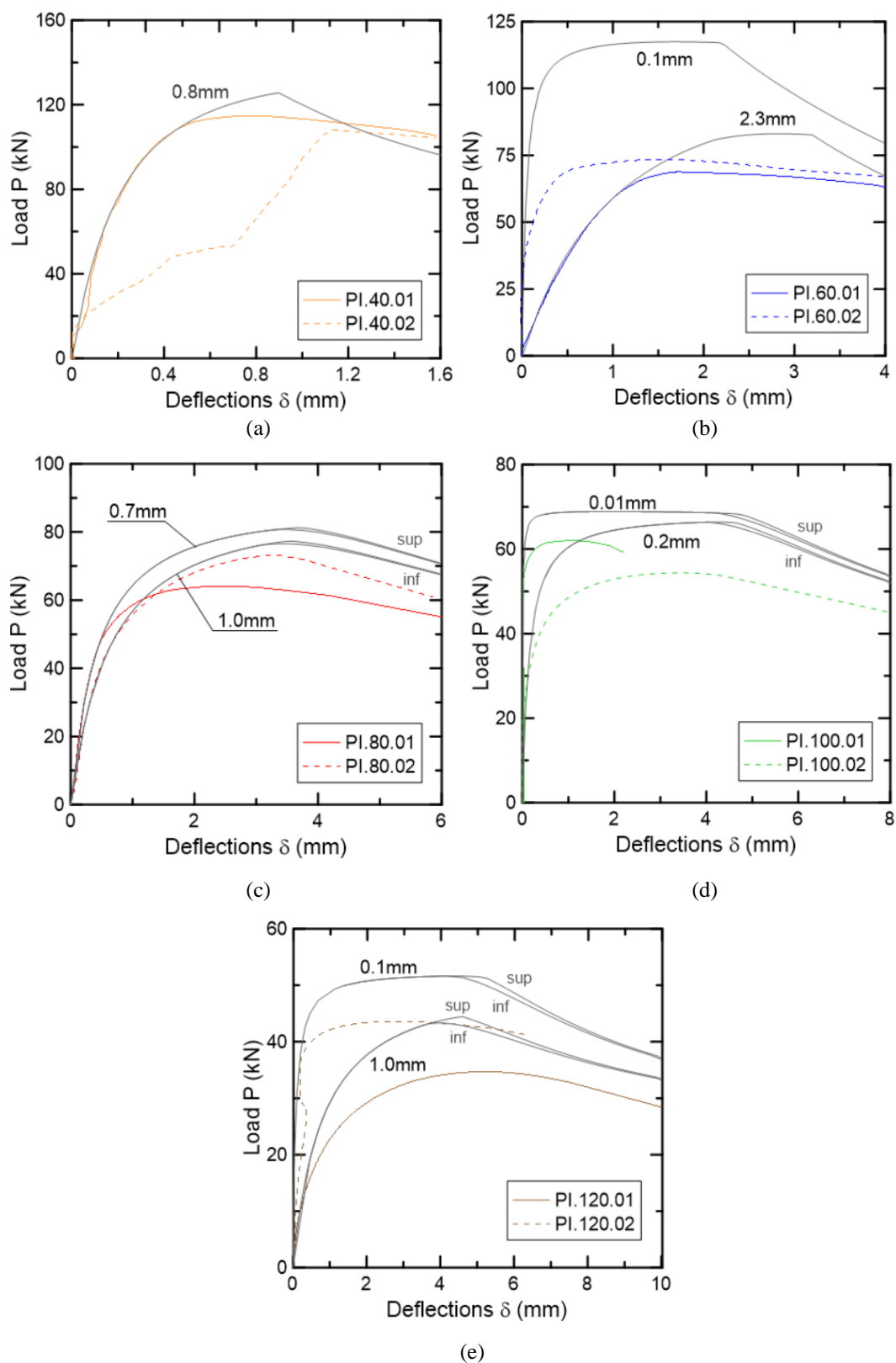


Figure 4.28 – Experimental and theoretical plots for each length tested: (a) 40 cm; (b) 60 cm; (c) 80 cm; (d) 100 cm; (e) 120 cm.

The behavior of the experimental curves was well represented by the theoretical curves until the established limit of 40% of the experimental maximum load. In general, all columns reached a maximum load lower than expected, which may be explained by deviations in modulus of elasticity. Column PI.40.02 exhibited a different behavior than expected, probably because it was not given enough time for the polyester-based body filler to set, resulting in accommodation of specimen and larger eccentricities. This is shown in Figure 4.29, where the increase in the deformation with a low increase in the load can be seen. Column PI.120.02 also presented this problem, however it did not disturb the overall behavior. As it can be seen, for these I-section columns, the influence of the tensile strength of concrete increases as the column length increases. The 40-cm and 60-cm long columns failed before the concrete cracking occurred. For the longer columns tested, the influence is still very small.

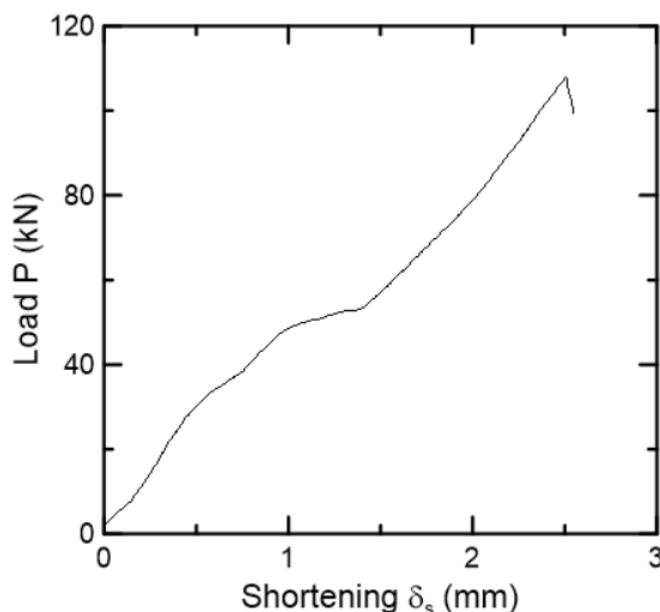


Figure 4.29 – Load *versus* shortening of column PI.40.02.

The column PI.60.02 presented the greatest difference between experimental results and theoretical model prediction. Analyzing the deflections provided by the two horizontal displacement transducers, as shown in Figure 4.30(a), it is possible to notice a column rotation, which may have been caused by an in-plane eccentricity (parallel to the web). For no in-plane eccentricity, the load is equally distributed for each half of the cross section (50%), making both flanges work equally thus allowing a higher failure load. On the other hand, this

distribution may change in the presence of these imperfections and premature failure may occur. The influence of this in-plane imperfection may be analyzed in a simplified way considering only half of cross-section loaded with a fraction of the total load P . Figure 4.30(b) shows plots for columns with half-sections loaded with 50% to 80% of the total load, considering an initial imperfection (perpendicular to the web) of 0.1 mm. As it can be seen, a good agreement between model and experiment was achieved for 80%, indicating that the eccentricity parallel to web direction produces the same effect as this load fraction being carried by half-section. A similar study could be carried out to achieved better agreement for other columns.

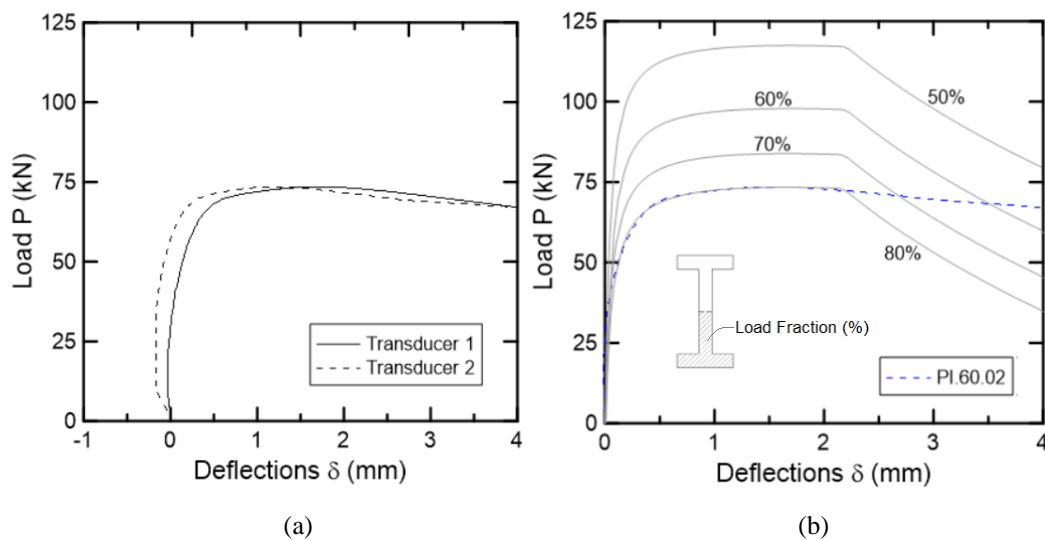


Figure 4.30 – Column PI.60.02: (a) P - δ experimental curves for the two horizontal displacement transducers; (b) P - δ curves presenting the theoretical plots for half-sections loaded with 50% to 80% of the total load considering an initial imperfection of 0.1 mm.

The initial imperfections obtained from the theoretical curves and the Southwell plots are presented in Table 4.13, along with the imperfection limits ($L/500$) for each length. The same order of magnitude was achieved between theoretical and experimental results. Only column PI.60.01 had an imperfection higher than the limit established ($L/500$), obtained from the theoretical curve.

Table 4.14 presents the maximum experimental and theoretical loads obtained for each column tested, showing results of the same order of magnitude.

Table 4.13 – Initial imperfections of columns by Southwell plot, theoretical curves and the imperfection limits.

Column	Initial imperfections (mm)		
	Southwell Plot	Theoretical Curve	Limit L/500
PI.40.01	0.22	0.80	0.8
PI.40.02	0.16	-	
PI.60.01	1.70	2.30	1.20
PI.60.02	0.02	0.10	
PI.80.01	0.26	0.70	1.60
PI.80.02	0.57	1.00	
PI.100.01	0.01	0.01	2.00
PI.100.02	0.20	0.20	
PI.120.01	0.80	1.00	2.40
PI.120.02	0.01	0.10	

Table 4.14 – Experimental and theoretical maximum loads.

Column	Maximum loads (kN)	
	Experimental	Theoretical
PI.40.01	115	126
PI.40.02	108	-
PI.60.01	68.8	83.1
PI.60.02	73.4	117
PI.80.01	64.0	$80.7 \leq P_{\max} \leq 81.2$
PI.80.02	73.1	$76.6 \leq P_{\max} \leq 77.3$
PI.100.01	62.0	68.9
PI.100.02	54.4	$66.3 \leq P_{\max} \leq 66.4$
PI.120.01	34.7	$43.3 \leq P_{\max} \leq 44.5$
PI.120.02	43.6	51.6

A normalized compressive strength curve is presented in Figure 4.31, representing the theoretical curve and the experimental points for all tested columns. Table 4.15 presents the critical loads used to obtain the non-dimensional

slenderness, obtained through the *GBTul* software. The 60 and 80 cm columns have their slenderness around the transition point between global buckling and crushing ($\lambda=1$), indicating that a greater interaction between these individual modes may occur.

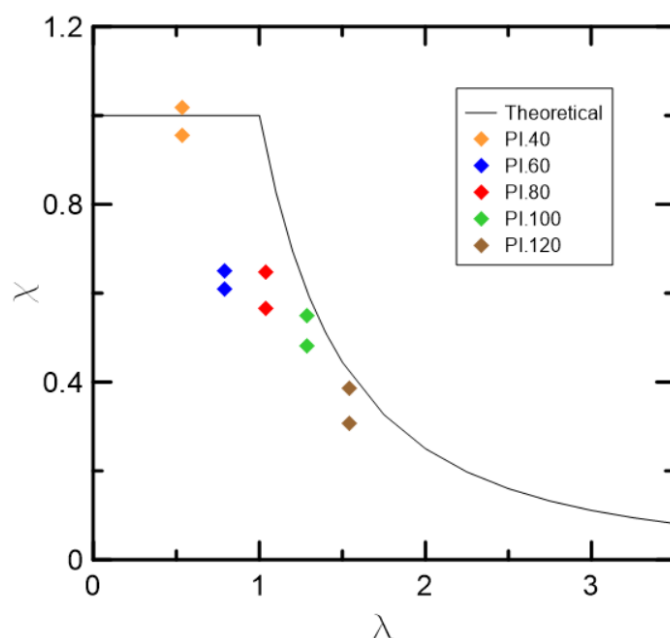


Figure 4.31 – Strength curve and experimental points.

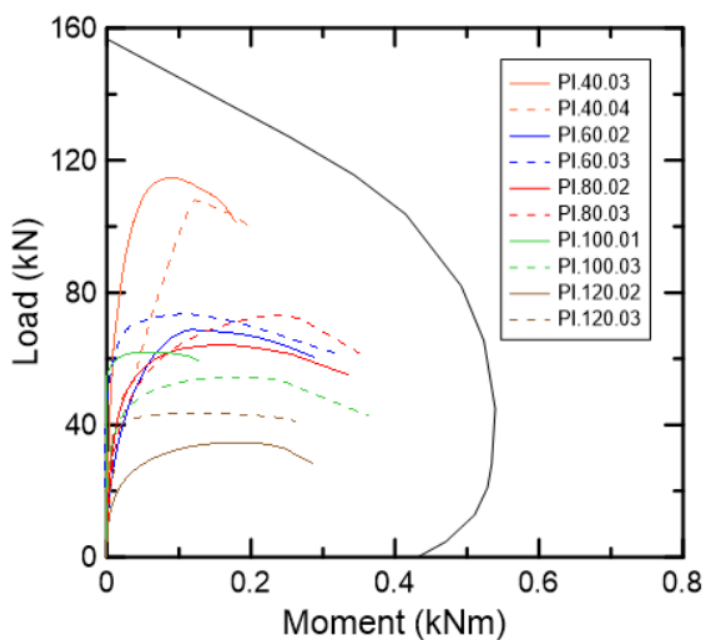


Figure 4.32 – Interaction diagram and experimental load-moment curves.

Analyzing Figure 4.32, which presents the interaction diagram, it can be noticed that all columns failed by stability failure (global buckling) because they have reached a deflection for which $\partial M / \partial P$ approaches infinity and did not crossed the failure envelope curve.

The relationship between the experimental non-dimensional slenderness $\bar{\lambda}_{exp}$ and the theoretical one $\bar{\lambda}_{theor}$ for each column obtained from the strength curve is shown in Table 4.15, along with the critical loads obtained through the *GBTul* software. PI.60.01 had the lowest percentage due to the initial imperfection higher than the one established as a limit. The other lower results happened for the 60 and 80 cm columns. For shorter columns, the greater stresses associated with imperfections in both directions caused a concrete plasticization in some regions. This lead to an apparent stiffness reduction which accelerates the instability process and cause the collapse for smaller loads than those expected for the perfect condition. Apart from these, all columns achieved a percentage higher than 70%, showing a good agreement with the theoretical curve.

Table 4.15 – Critical loads and relationship between experimental and theoretical non-dimensional slenderness obtained from the strength curve.

Column	P_{cr} (kN)	$(\bar{\lambda}_{exp} / \bar{\lambda}_{theor})$ (%)
PI.40.01	390	102
PI.40.02		95.6
PI.60.01	182	60.9
PI.60.02		65.0
PI.80.01	105	61.0
PI.80.02		69.6
PI.100.01	68.0	91.2
PI.100.02		80.0
PI.120.01	47.7	72.7
PI.120.02		91.4

5. Conclusions

5.1. Final Considerations

In this study, the performance of Textile Reinforced Concrete (TRC) columns subject to compression was studied. A literature review was presented and an experimental program was conducted in order to investigate TRC columns behavior. The conclusions from this study are:

- a. Although the difficulties in reproducing the CLC test for a composite made with a cementitious matrix, good results were achieved. Considering a perfect bond between matrix and reinforcement, it was possible to estimate the fiber contribution on the compressive strength of TRC. It is important to notice that no textile buckling was observed during test.
- b. Even though the values obtained for the TRC compressive strength were higher than the one obtained for the compressive strength of concrete, more CLC tests must be done in order to guarantee the consideration of the contribution of the fiber in compressed TRC members.
- c. A numerical method for predicting non-linear axial-force-moment-curvature relationships of TRC plates was proposed by using an iteratively routine in *Maple* software. The theoretical predictions and the experimental results showed a good agreement. In order to obtain more similar experimental results, a higher quality control in casting should be expected.
- d. In agreement with theory, it was observed that columns with greater slenderness presented greater out-of-plane deflections and lower maximum loads.
- e. The correct use of the polyester-based body filler (*Iberê*) is really important on the test results. If it is not given enough time for the filler

material to set, the soft mixture will not be able to restrain the rotation and accommodations may happen throughout the test.

- f. Even though the external dimensions of the columns were measured, it was very hard to predict the total imperfection of each column, especially for the I-section columns. The position of the fiber can vary along the length and the column should be perfectly positioned in the set-up to avoid a loading eccentricity.
- g. Numerical models were developed in order to calculate the load-deflections and the interaction diagram of the rectangular and I-section columns. A comparison between the numerical predictions and the experimental results showed good agreement in the axial force-lateral deflection relations, maximum loads and axial force-bending moment relations of the columns.
- h. The maximum load for each column is highly influenced by the tensile strength of concrete, especially for the rectangular columns, in which the experimental results indicated a greater apparent tensile strength of concrete. This influence is higher for columns with greater slenderness.
- i. The initial imperfections obtained from the Southwell plots and from the analytical models are of the same order of magnitude. It can be noticed that the control of the imperfections is crucial for the results of a compression test. The greater the imperfections, the lower the maximum loads obtained.
- j. The observed failure modes were all consistent with theoretical predictions. All columns failed by instability failure (global buckling).
- k. Imperfections in both directions may cause a concrete plasticization in some regions, leading to an accelerated instability process and a premature failure.

5.2. Future Works

In order to improve the study of the behavior of TRC columns subject to compression, several suggestions for further investigations are proposed:

- a. Perform CLC tests on the fine-grained concrete matrix in order to obtain a more accurate value for the compressive strength f_c and compressive modulus E_c of the concrete due to the scale factor;
- b. Ensure a higher quality control in all molding processes with more spacers along the column's length, in order to obtain lower initial imperfections;
- c. Conduct an experimental program on more specimens for each test realized and on columns with longer lengths with different cross-section geometry and end conditions;
- d. Develop a non-linear numerical analysis in order to calculate the load-deflections curve in a column, which do not assume as sinusoidal deflection shape and which consider the creep effects on concrete;
- e. Develop a method to determine the experimental critical loads of TRC columns.

6. References

- [1] J. Hegger and S. Voss, "Investigations on the bearing behaviour and application potential of textile reinforced concrete," *Engineering Structures*, vol. 30, no. 7, pp. 2050–2056, 2008.
- [2] A. Scholzen, R. Chudoba, and J. Hegger, "Thin-walled shell structures made of textile-reinforced concrete - Part I: Structural design and construction," *Structural Concrete*, vol. 16, no. 1, pp. 106–114, 2015.
- [3] J. Hegger, N. Will, A. Bentur, M. Curbach, F. Jesse, and B. Mobasher, "6.2. Mechanical behaviour of textile reinforced concrete," *Textile Reinforced Concrete - State-of-the-Art Report of RILEM*, pp. 133–186, 2006.
- [4] ACI 440.1R-15, *Guide for the Design and Construction of Structural Concrete Reinforced with Fiber-Reinforced Polymer (FRP) Bars*. American Concrete Institute, 2015.
- [5] A. Nanni, "North American design guidelines for concrete reinforcement and strengthening using FRP: Principles, applications and unresolved issues," *Construction and Building Materials*, vol. 17, no. 6–7, pp. 439–446, 2003.
- [6] M. Z. Afifi and B. Mohamed, H.M. Benmokrane, "Axial capacity of circular concrete columns reinforced with glass-FRP bars and spirals," *Journal of Composites for Construction*, vol. 18, no. 1, 2014.
- [7] N. S. Paramanantham, "Investigation of the Behavior of Concrete Columns Reinforced with Fiber Reinforced Plastic Rebars," MS thesis, Lamar University, Beaumont, Tex, 1993.
- [8] N. Kawaguchi, "Ultimate Strength and Deformation Characteristics of Concrete Members Reinforced with AFRP Rods under Combined Axial Tension or Compression and Bending," *Fiber-Reinforced-Plastic Reinforcement for Concrete Structures*, vol. 138, pp. 671–

684, 1993.

- [9] C. Choo, I. E. Harik, and H. Gesund, "Strength of Rectangular Concrete Columns Reinforced with Fiber-Reinforced Polymer Bars," *ACI Structural Journal*, vol. 103, no. 3, 2006.
- [10] T. Triantafillou, *Textile Fibre Composites in Civil Engineering*. Woodhead Publishing, 2016.
- [11] R. F. Zollo, "Fiber-reinforced concrete: an overview after 30 years of development," *Cement and Concrete Composites*, vol. 19, no. 2, pp. 107–122, 1997.
- [12] W. Bramehuber and T. Brockmann, "1. Introduction," *Textile Reinforced Concrete - State-of-the-Art Report of RILEM*, pp. 1–3, 2006.
- [13] A. Shams, M. Horstmann, and J. Hegger, "Experimental investigations on textile-reinforced concrete (TRC) sandwich sections," *Composite Structures*, vol. 118, no. 1, pp. 643–653, 2014.
- [14] J. Hegger, M. Horstmann, and M. Zell, "Textile Reinforced Concrete—Realization in applications," *Tailor Made Concrete Structures*, pp. 357–362, 2008.
- [15] M. Zoghi, *The international handbook of FRP composites in civil engineering*. CRC Press, 2013.
- [16] M. Butler, M. Lieboldt, and V. Mechtcherine, "Application of Textile-Reinforced Concrete (TRC) for structural strengthening and in prefabrication," *Advances in Cement-Based Materials*, pp. 127–136, 2010.
- [17] T. Brockmann and W. Bramehuber, *Mechanical and Fracture Mechanical Properties of Fine Grained Concrete for Textile Reinforced Composites*. Fakultät für Bauingenieurwesen, 2005.
- [18] B. Mobasher, *Mechanics of fiber and textile reinforced cement composites*. CRC Press, 2012.
- [19] T. Gries, A. Roye, P. Offermann, T. Engler, and A. Peled, "3. Textiles," *Textile Reinforced Concrete - State-of-the-Art Report of RILEM*, pp. 11–27, 2006.
- [20] A. Céline, S. Fréour, F. Jacquemin, and P. Casari, "The hygroscopic

- behavior of plant fibers: a review,” *Frontiers in Chemistry*, pp. 1–12, 2014.
- [21] A. Peled, A. Bentur, and D. Yankelevsky, “Effects of woven fabric geometry on the bonding performance of cementitious composites: mechanical performance,” *Advanced Cement Based Materials*, vol. 7, no. 1, pp. 20–27, 1998.
 - [22] A. Peled, A. Bentur, and D. Yankelevsky, “Flexural performance of cementitious composites reinforced with woven fabrics,” *Journal of materials in civil engineering*, vol. 11, no. 4, pp. 325–330, 1999.
 - [23] A. Peled, Z. Cohen, Y. Pasder, A. Roye, and T. Gries, “Influences of textile characteristics on the tensile properties of warp knitted cement based composites,” *Cement and Concrete Composites*, vol. 30, no. 3, pp. 174–183, 2008.
 - [24] C. Soranakom and B. Mobasher, “Geometrical and mechanical aspects of fabric bonding and pullout in cement composites,” *Materials and Structures*, vol. 42, no. 6, pp. 765–777, 2009.
 - [25] J. Donnini, V. Corinaldesi, and A. Nanni, “Mechanical properties of FRCM using carbon fabrics with different coating treatments,” *Composites Part B: Engineering*, vol. 88, no. C, pp. 220–228, 2016.
 - [26] L. Bähr, F. de A. Silva, and D. Roehl, “Mechanical Behavior and Numerical Modeling of Textile Reinforced Concrete,” MS thesis, PUC-Rio, 2016.
 - [27] J. Hegger and S. Voss, “Load-bearing behaviour of textile-reinforced concrete under 2-axial loading. Textile Reinforced Structures,” *Proceedings of the 2nd Colloquium on textile Reinforced Structures (CTRS2)*, pp. 313–324, 2003.
 - [28] F. Jesse, “Tragverhalten von Filamentgarnen in zementgebundener Matrix.,” MS thesis, Fakultät of Civil Engineering, Technische Universität Dresden, 2004.
 - [29] J. Hegger and S. Voss, “Textile Reinforced Concrete - Bearing Behaviour, Design, Application,” *Composites in Construction 1005 - Third International Conference*, pp. 1139–1146, 2005.
 - [30] J. G. MacGregor and J. K. Wight, *Reinforced concrete mechanics &*

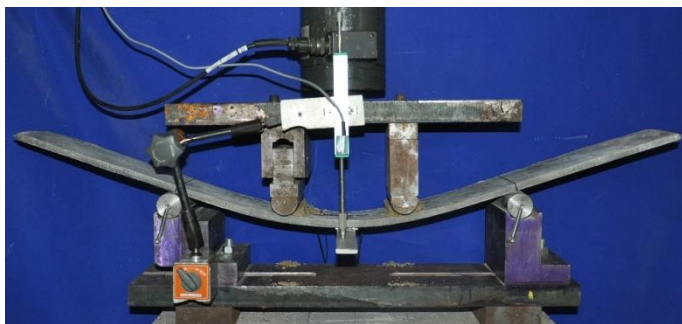
design. Pearson, 2012.

- [31] S. P. Timoshenko and J. M. Gere, "Theory of elastic stability." McGrawHill-Kogakusha Ltd, Tokyo, pp. 9–16, 1961.
- [32] R. D. Ziemian, *Guide to stability design criteria for metal structures*. John Wiley & Sons, 2010.
- [33] A. Reis and D. Camotim, *Estabilidade Estrutural*. Lisboa: McGrawHill, 2001.
- [34] R. Schardt, "Generalized beam theory - An adequate method for coupled stability problems," *Thin-Walled Structures*, vol. 19, no. 2–4, pp. 161–180, 1994.
- [35] R. Bebiano, N. Silvestre, and D. Camotim, "GBTul - A code for the buckling analysis of cold-formed steel members," *Proceedings of 19th International Specialty Conference on Recent Research and Developments in Cold-Formed Steel Design and Construction*, pp. 61–79, 2008.
- [36] D. C. T. Cardoso, K. A. Harries, and E. Batista, "Compressive strength of pultruded glass-fiber reinforced polymer (GFRP) columns," MS thesis, COPPE-UFRJ, 2014.
- [37] R. V. Southwell, "On the analysis of experimental observations in problems of elastic stability," *Proceedings of the Royal Society of London A: Mathematical, Physical and Engineering Sciences*, vol. 135, no. 828, 1932.
- [38] Z. P. Bazant, L. Cedolin, and J. W. Hutchinson, *Stability of Structures: Elastic, Inelastic, Fracture, and Damage Theories*. World Scientific, 2010.
- [39] E. Hognestad, "Study of combined bending and axial load in reinforced concrete members," University of Illinois at Urbana Champaign, College of Engineering. Engineering Experiment Station, 1951.
- [40] W. F. Chen and T. Atsuta, *Theory of Beam-Columns: Vol. 1 - In-Plane Behavior and Design*. McGrawHill, 1976.
- [41] I. E. Harik and H. Gesund, "Reinforced Concrete Column in Biaxial Bending," *Concrete Frame Structures—Stability and Strength*, pp.

- 111–132, 1986.
- [42] J. K. Kim and J. K. Yang, “Buckling behaviour of slender high-strength concrete columns,” *Engineering Structures*, vol. 17, no. 1, pp. 39–51, 1995.
 - [43] L. Pallares, J. L. Bonet, P. F. Miguel, and M. A. Fernandez, “Experimental research on high strength concrete slender columns subjected to compression and biaxial bending forces,” *Engineering Structures*, vol. 30, no. 7, pp. 1879–1894, 2008.
 - [44] F. de A. Silva, M. Butler, V. Mechtcherine, D. Zhu, and B. Mobasher, “Strain rate effect on the tensile behaviour of textile-reinforced concrete under static and dynamic loading,” *Materials Science and Engineering A*, vol. 528, no. 3, pp. 1727–1734, 2011.
 - [45] ASTM Standard C1611/C1611M-14, “Standard Test Method for Slump Flow of Self-Consolidating Concrete.” ASTM International, West Conshohocken, PA, 2014.
 - [46] ASTM Standard D6641/D6641M-16e1, “Standard Test Method for Compressive Properties of Polymer Matrix Composite Materials Using a Combined Loading Compression (CLC) Text Fixture.” ASTM International, West Conshohocken, PA, 2016.
 - [47] D. F. Adams, L. A. Carlsson, and R. B. Pipes, *Experimental characterization of advanced composite materials*. CRC Press, 2014.
 - [48] “Maple User Manual.” [Online]. Available: https://www.maplesoft.com/documentation_center/maple19/UserManual.pdf. [Accessed: 29-Aug-2017].
 - [49] J. M. de Araújo, *Curso de concreto armado*. Editora Dunas, 2003.
 - [50] A. Bentur and S. Mindess, *Fibre reinforced cementitious composites*. CRC Press, 2007.

7. Appendix A – Four-point Bending Tests Reports

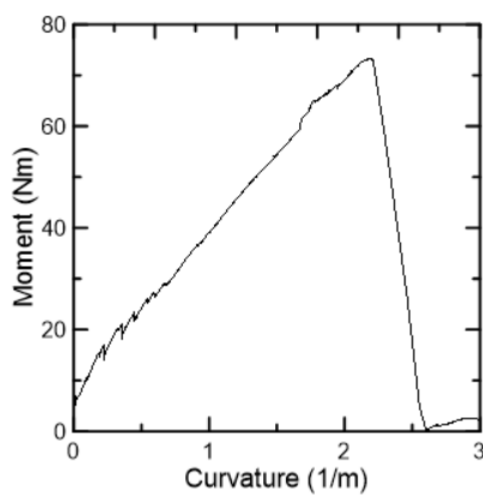
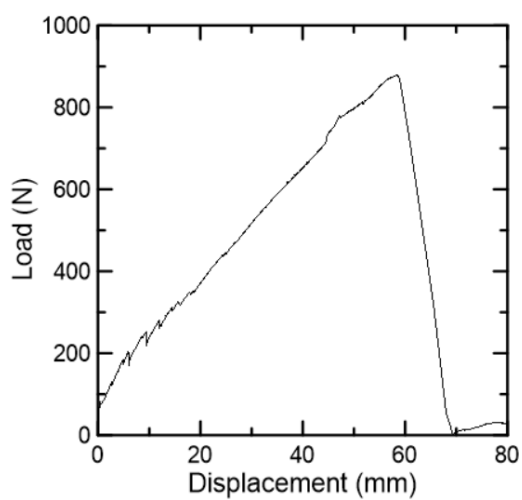
FP2A

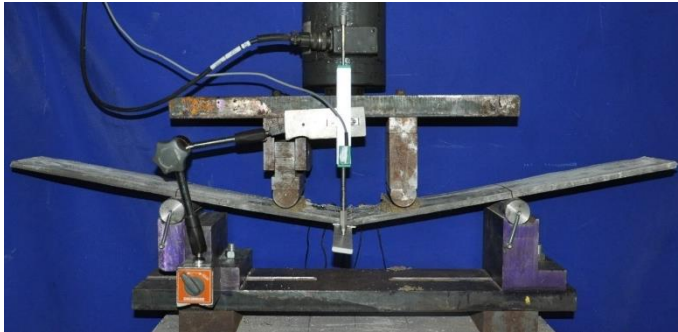


Date: August/2017

P_{max} : 879.5 N

M_u : 73.5 Nm

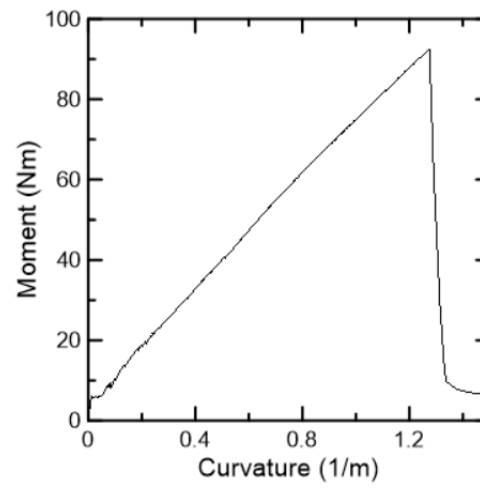
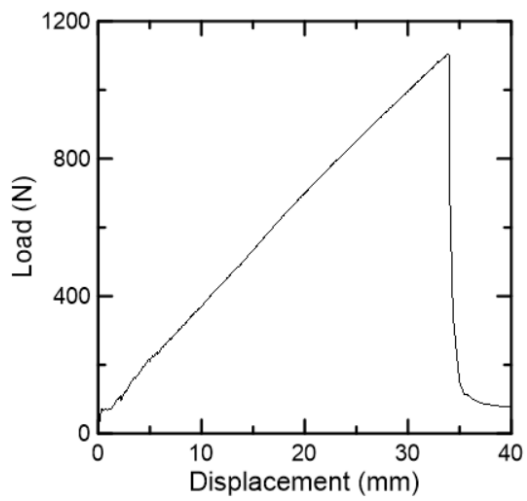


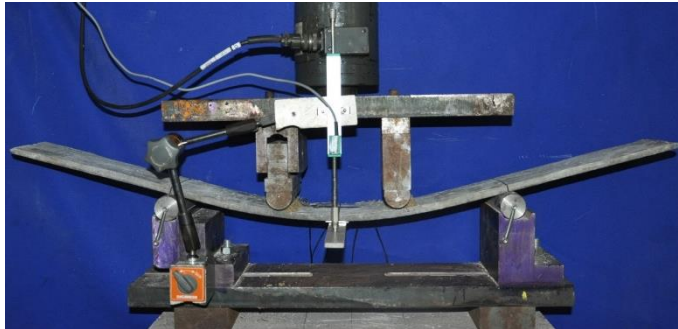
FP2B

Date: August/2017

P_{max} : 1105.7 N

M_u : 92.3 Nm

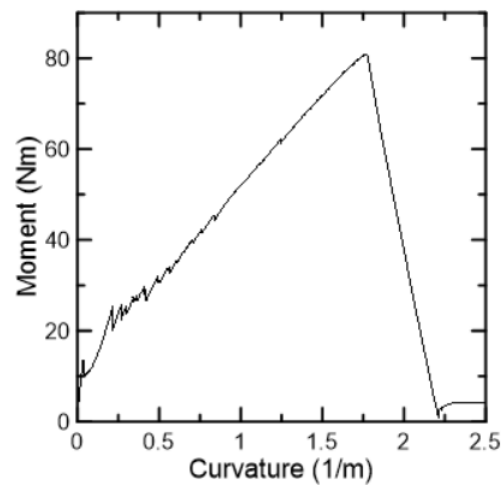
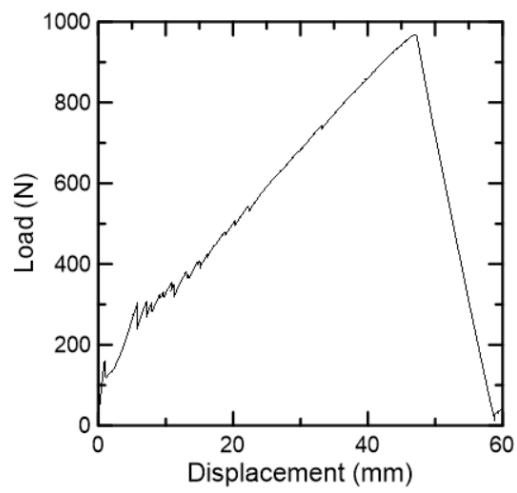


FP3A

Date: August/2017

P_{max} : 968.3 N

M_u : 80.9 Nm



8. Appendix B – Rectangular Column Tests Reports

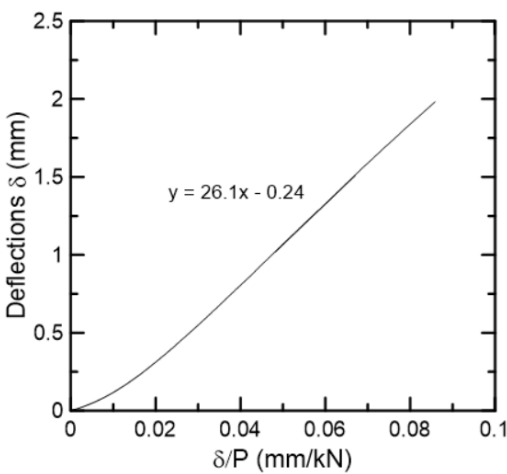
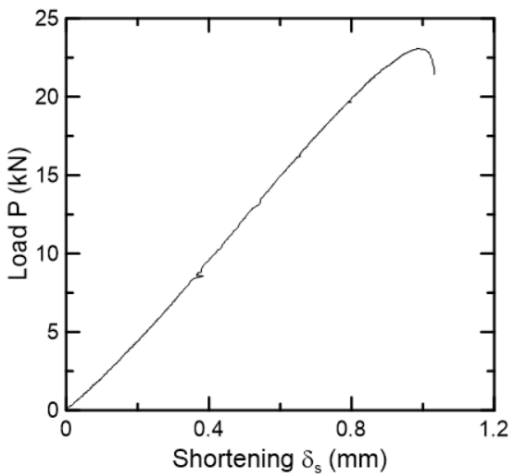
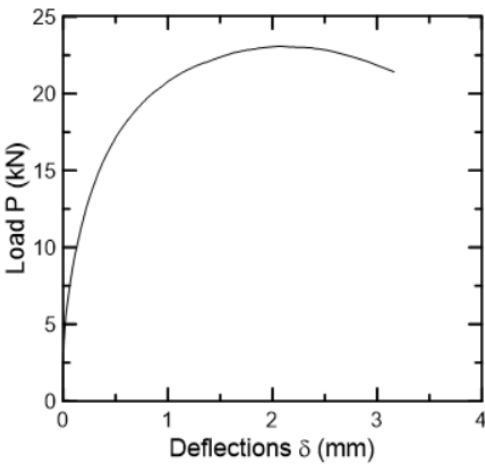
PA.60.01

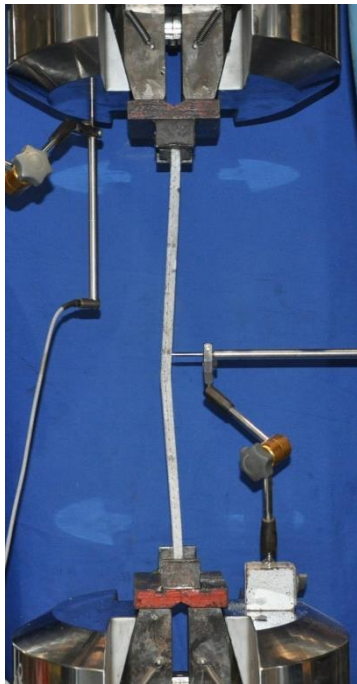


Date: Semptember/2017

P_{max} : 23.1 kN

δ_0 : 0.24 mm

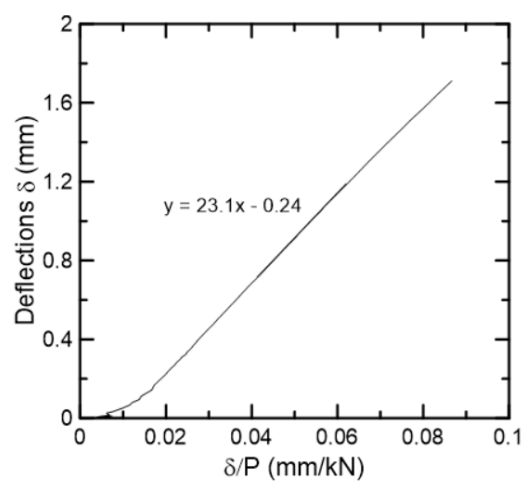
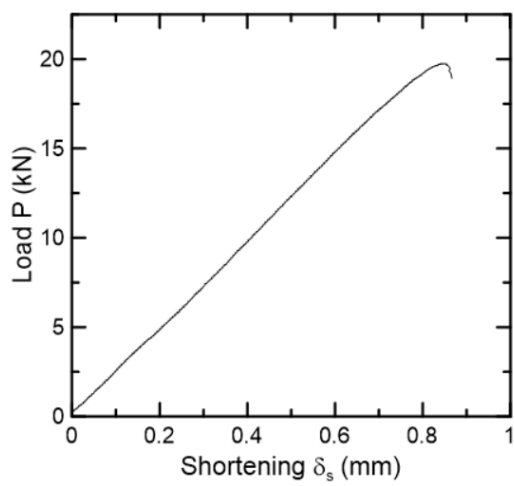
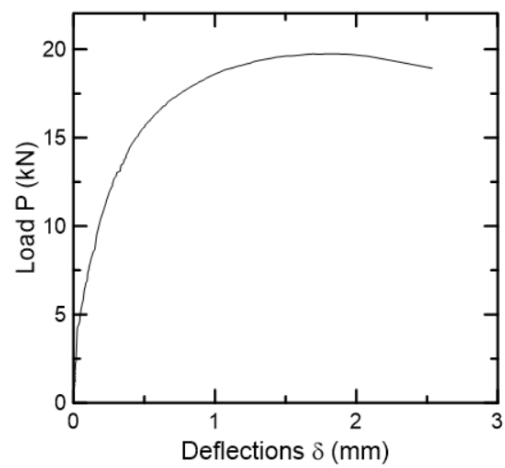


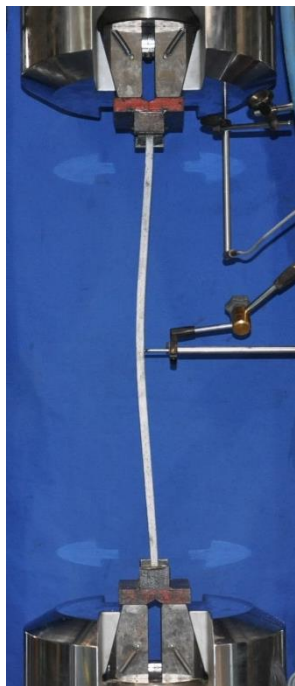
PA.60.02

Date: October/2017

P_{max} : 19.7 kN

δ_0 : 0.24 mm

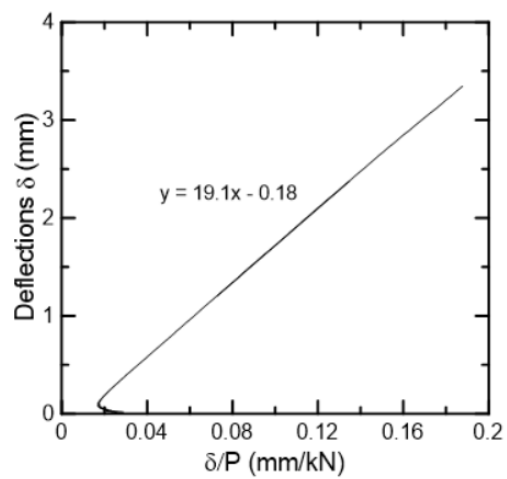
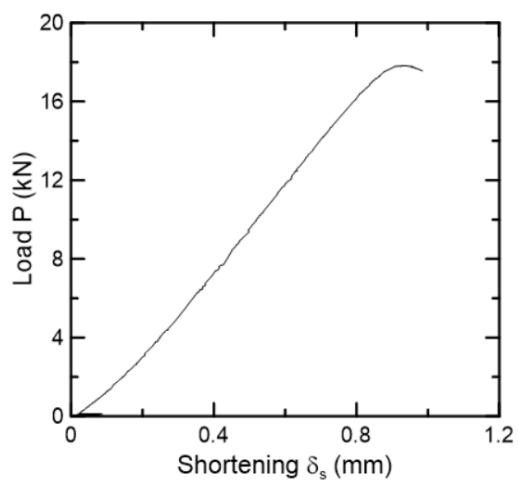
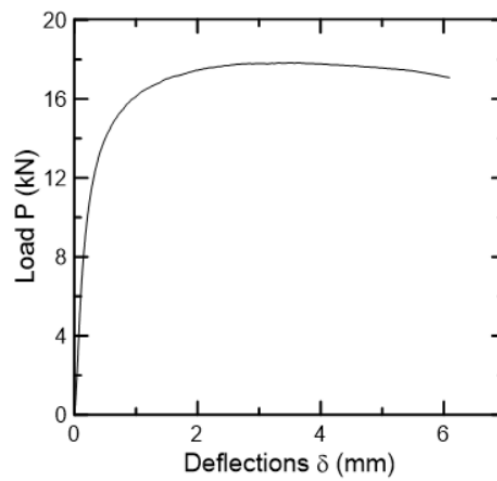


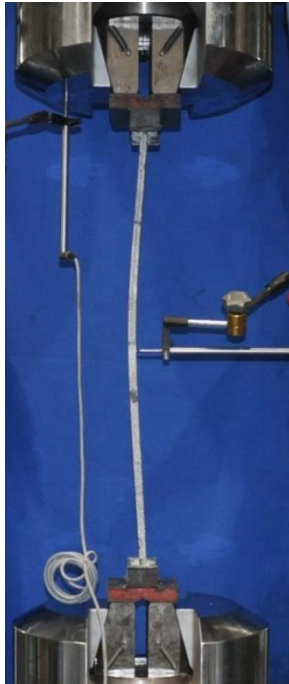
PA.80.01

Date: Semptember/2017

P_{max} : 17.3 kN

δ_0 : 0.18 mm

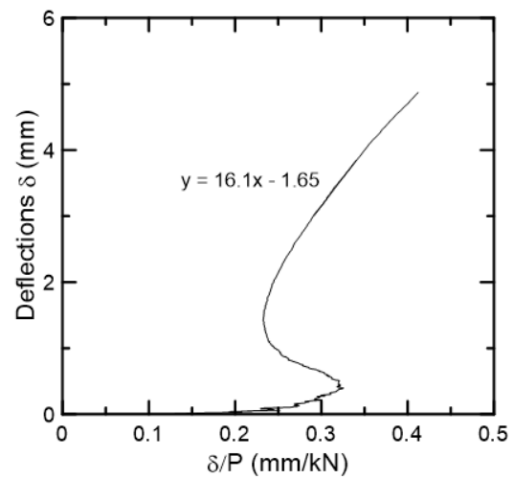
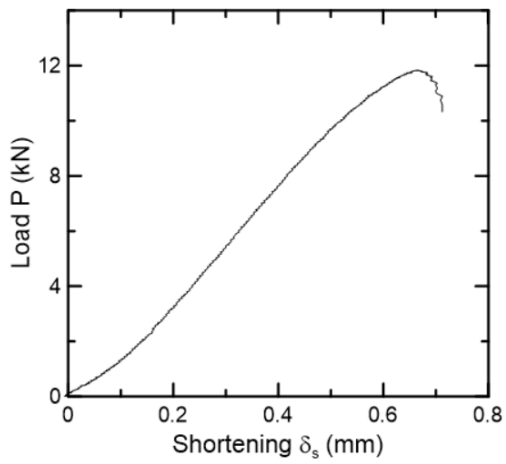
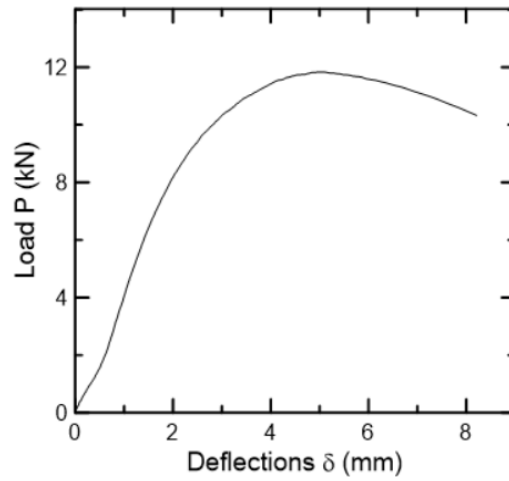


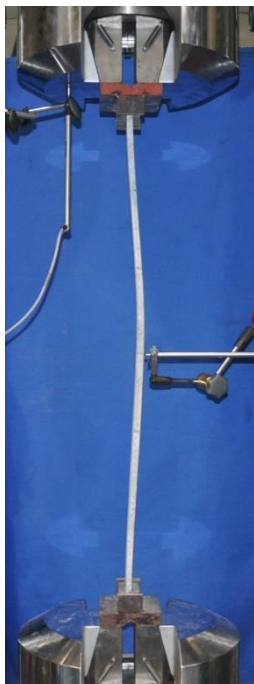
PA.80.02

Date: October/2017

P_{max} : 11.8 kN

δ_0 : 1.65 mm

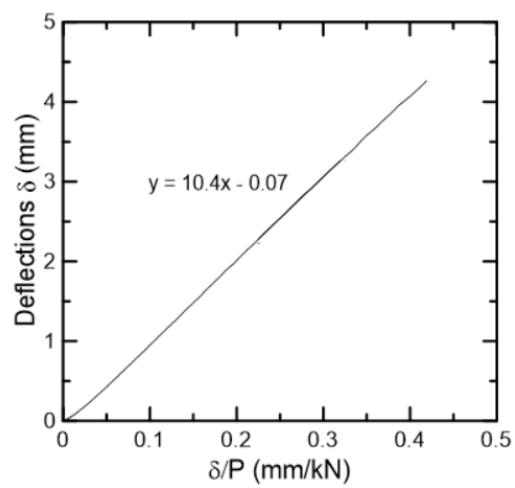
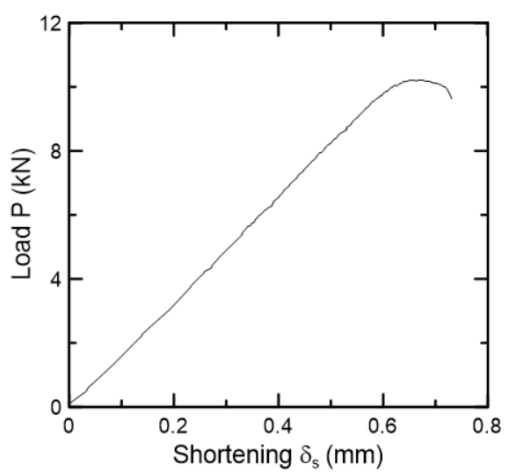
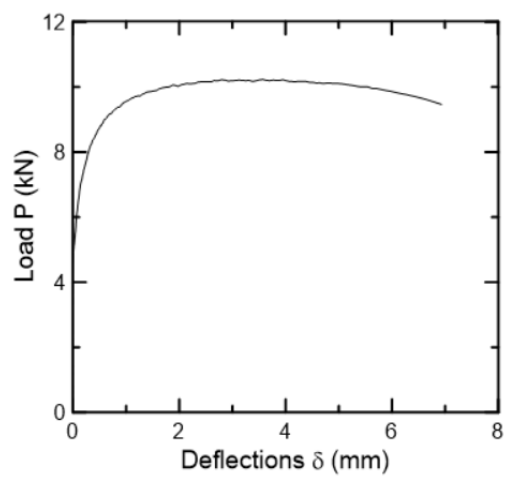


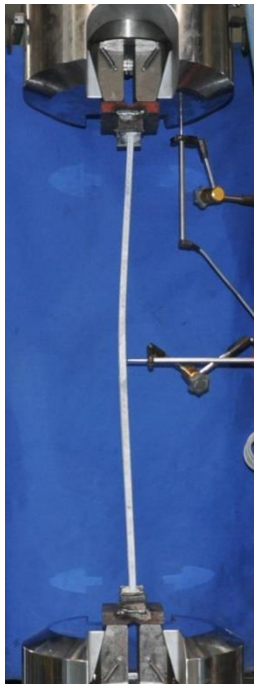
PA.100.01

Date: October/2017

P_{max} : 10.2 kN

δ_0 : 0.07 mm

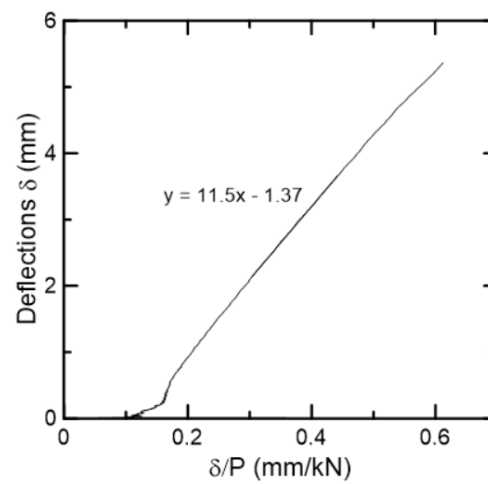
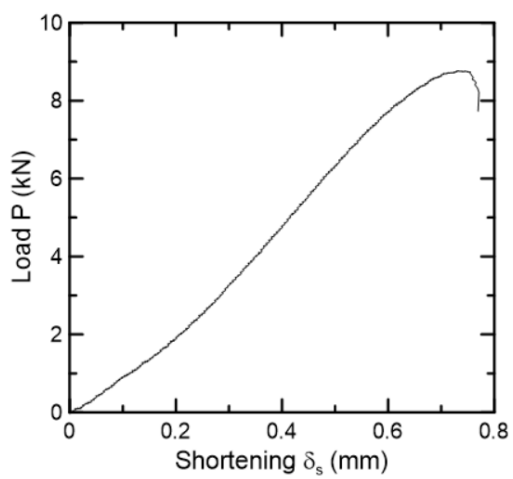
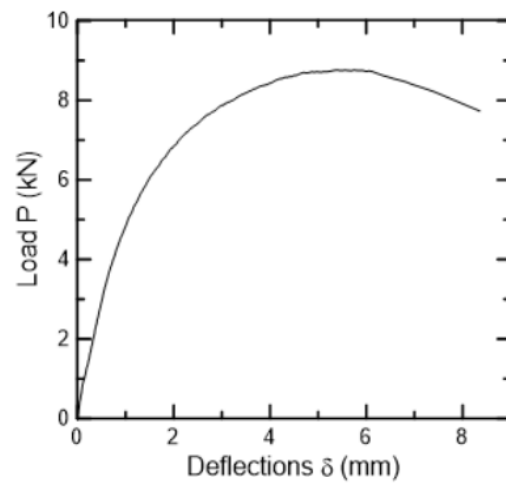


PA.100.02

Date: November/2017

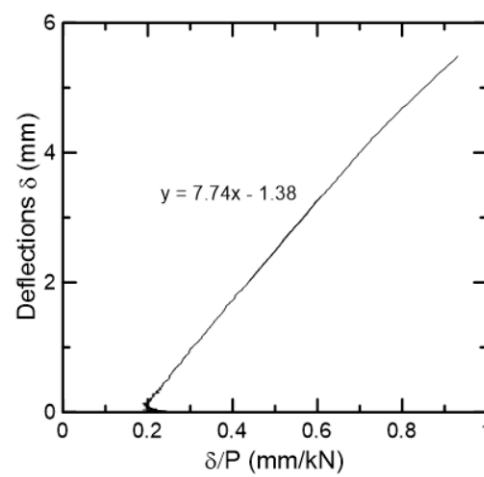
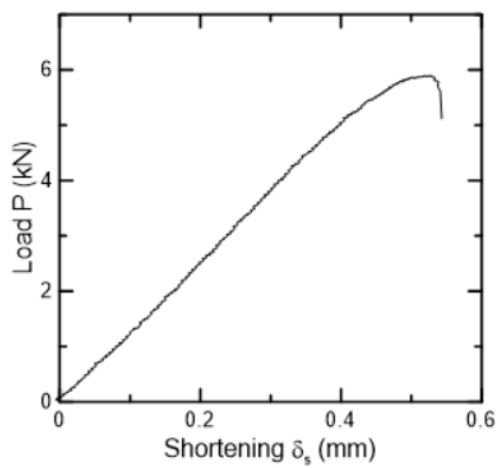
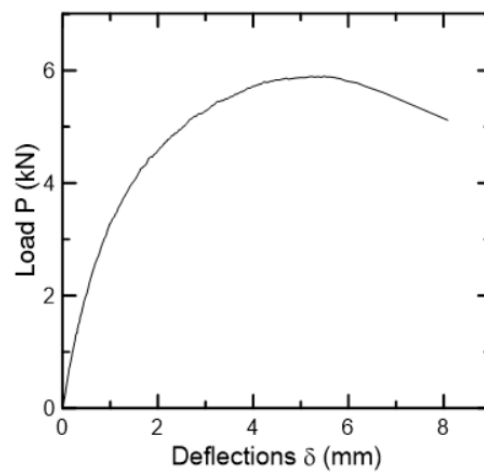
P_{max} : 8.76 kN

δ_0 : 1.37 mm



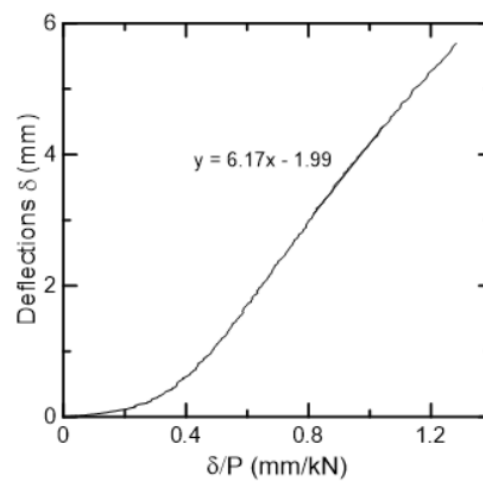
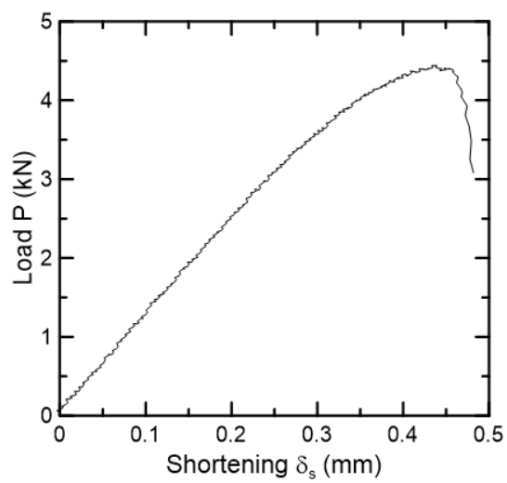
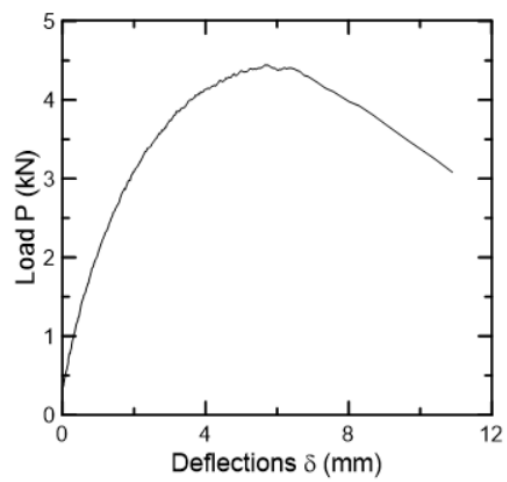
PA.120.01

Date: October/2017

 P_{max} : 5.90 kN δ_0 : 1.38 mm

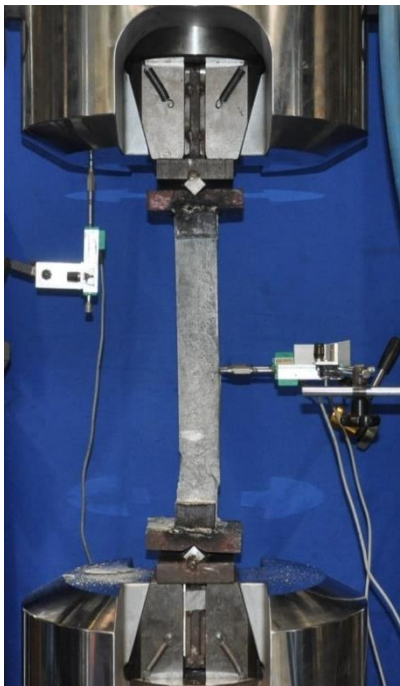
PA.120.02

Date: November/2017

 P_{max} : 4.44 kN δ_0 : 1.99 mm

9. Appendix C – I-Section Column Tests Reports

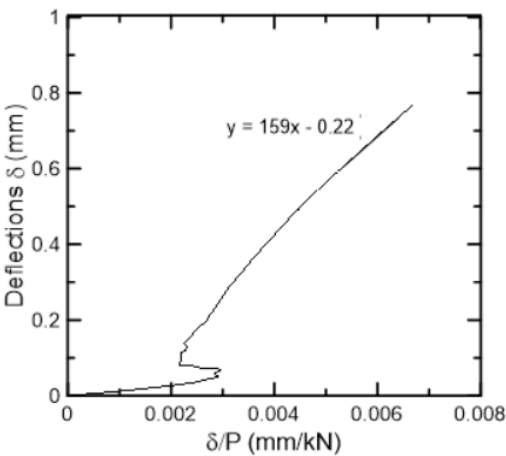
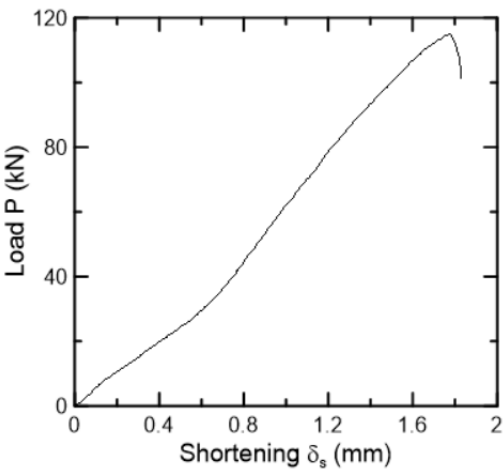
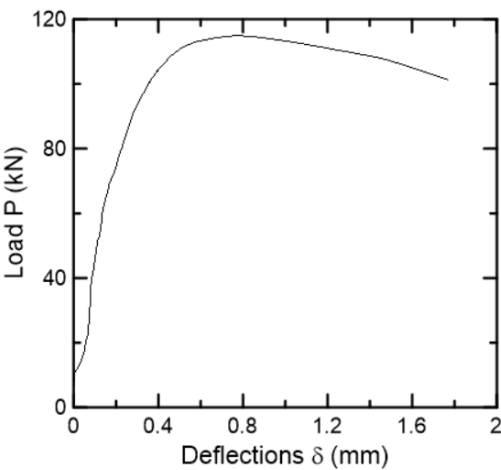
PL.40.01

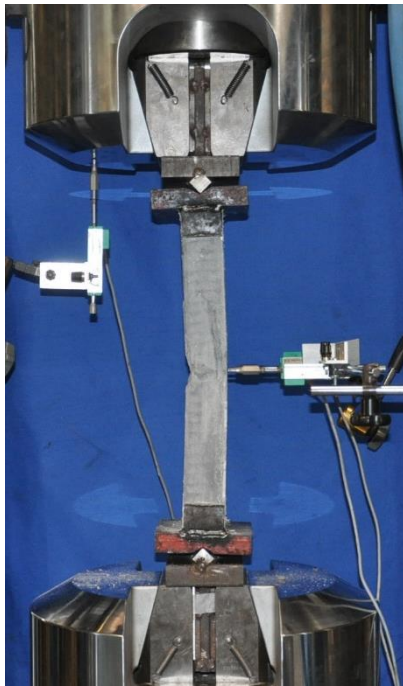


Date: November/2017

P_{max} : 115 kN

δ_0 : 0.22 mm

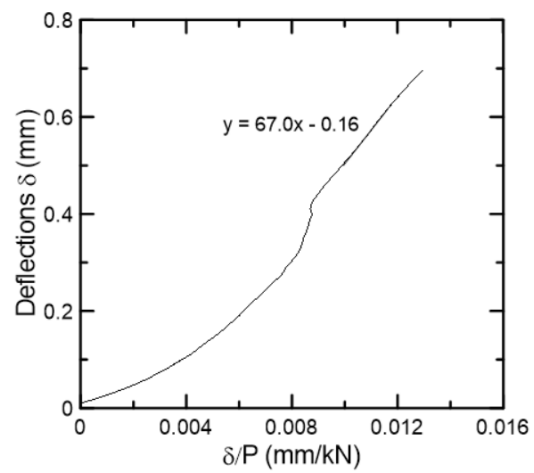
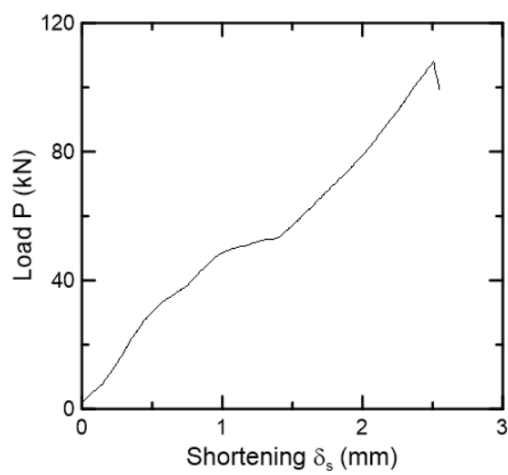
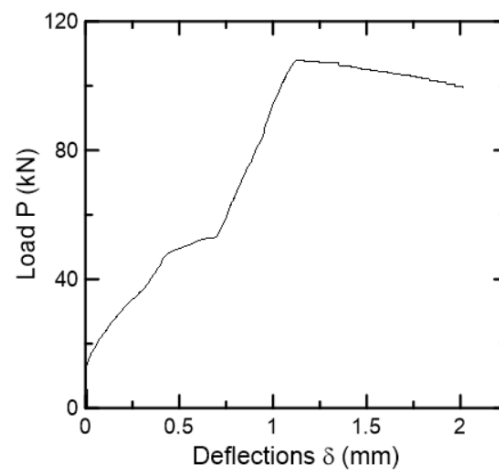


PL.40.02

Date: November/2017

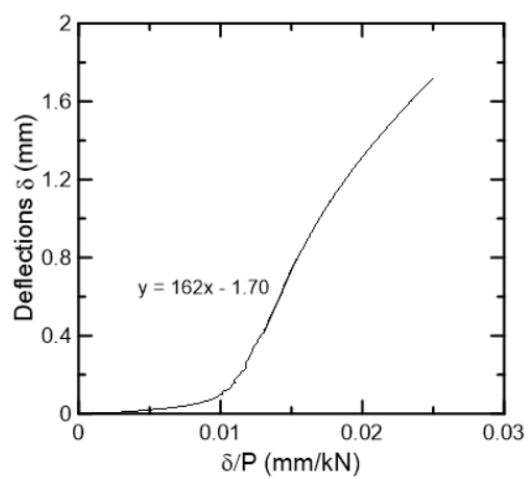
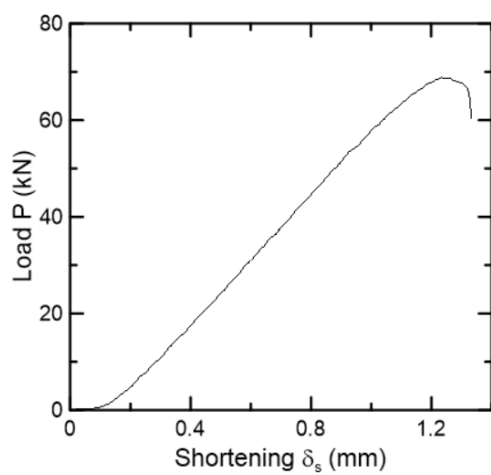
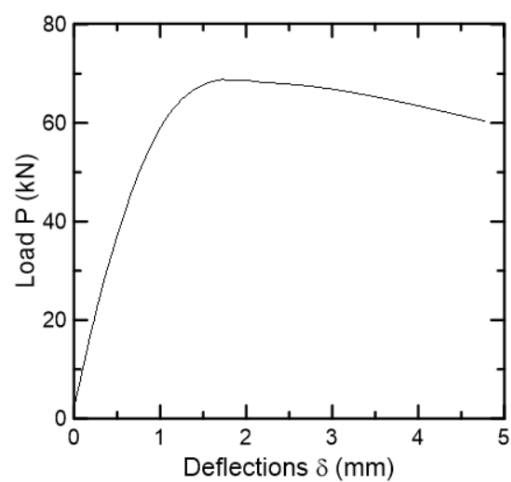
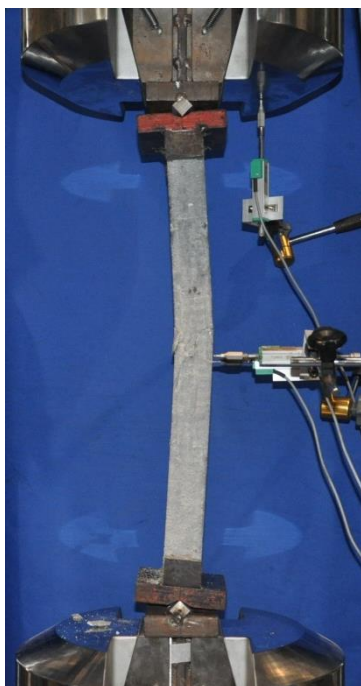
P_{max} : 108 kN

δ_0 : 0.16 mm



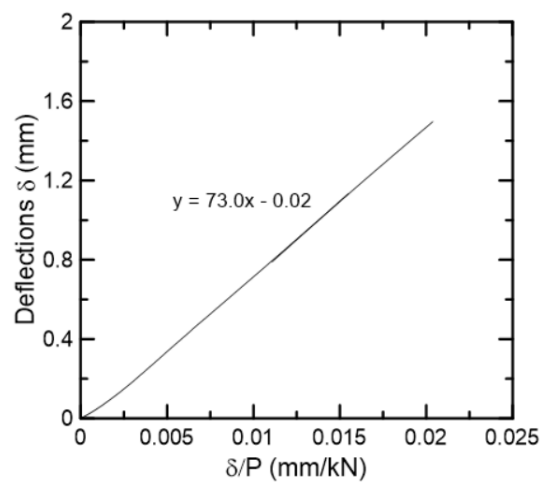
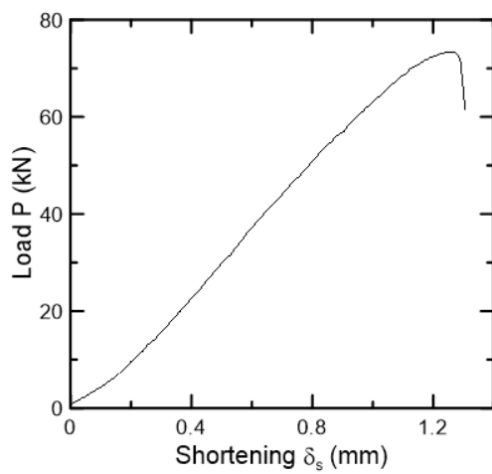
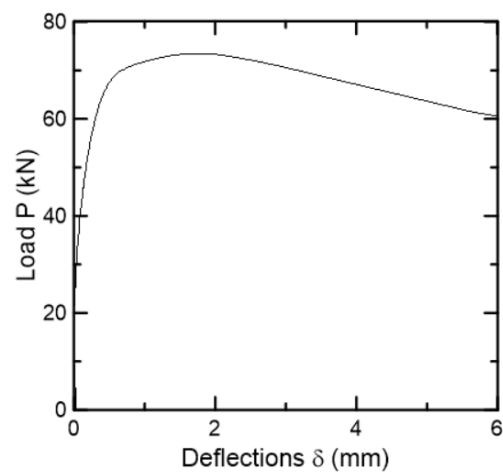
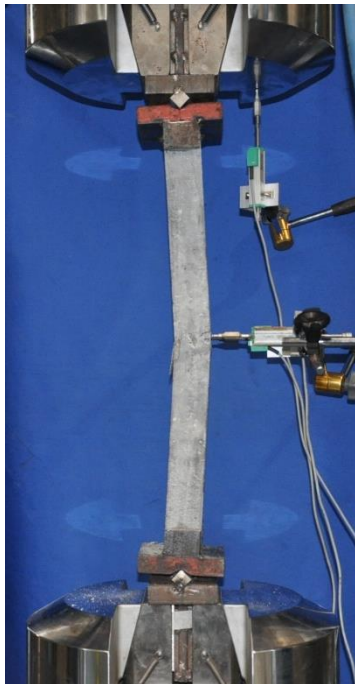
PL.60.01

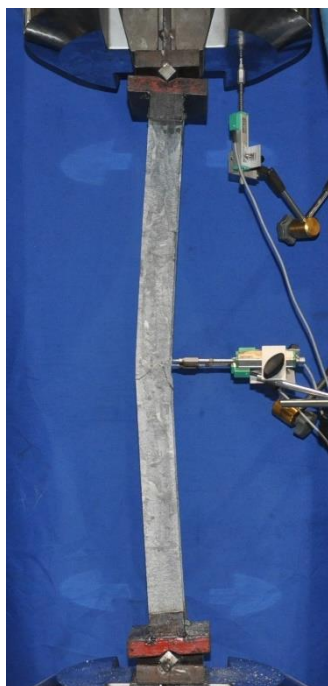
Date: September/2017

 P_{max} : 68.8 kN δ_0 : 1.70 mm

PL.60.02

Date: September/2017

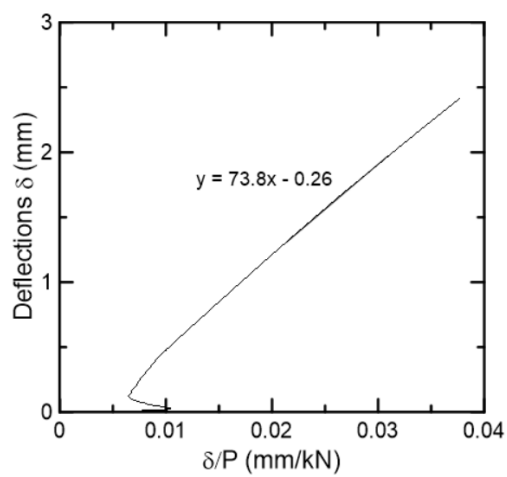
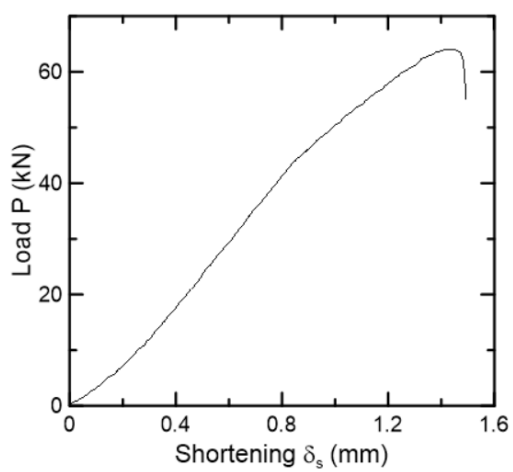
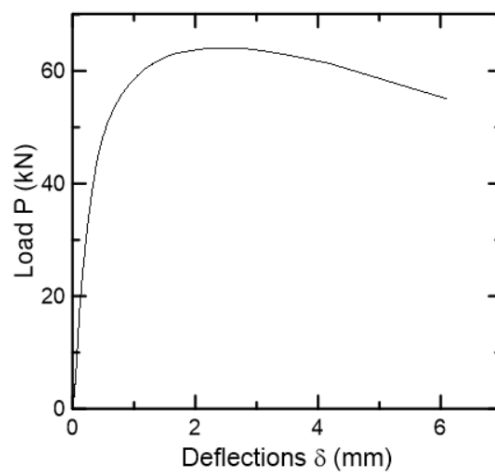
 P_{max} : 73.4 kN δ_0 : 0.02 mm

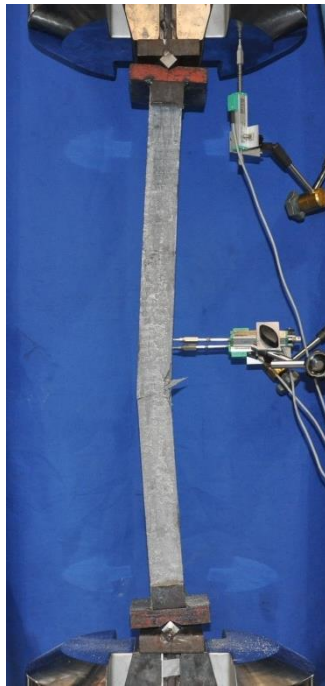
PL.80.01

Date: September/2017

P_{max} : 64.0 kN

δ_0 : 0.26 mm

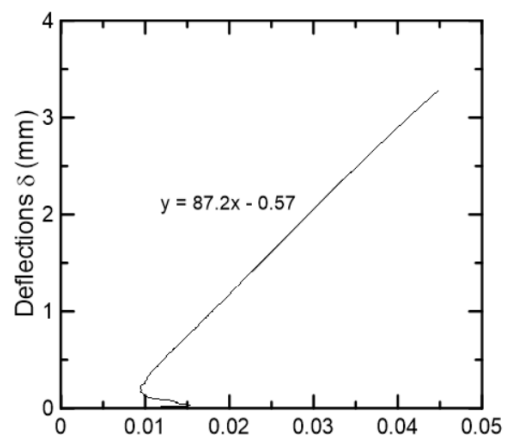
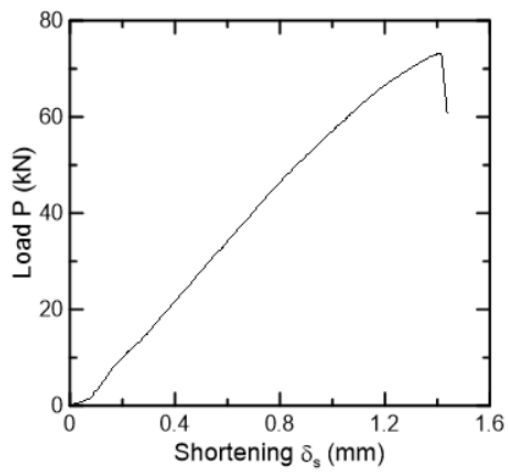
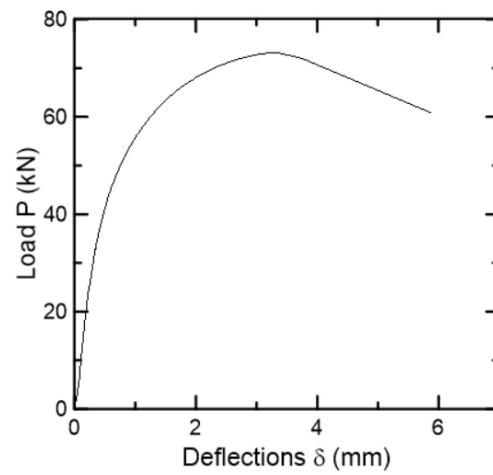


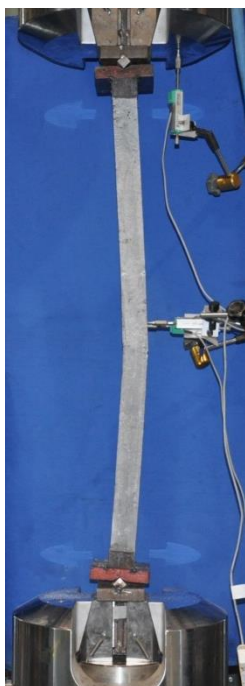
PL.80.02

Date: September/2017

P_{max} : 73.1 kN

δ_0 : 0.57 mm

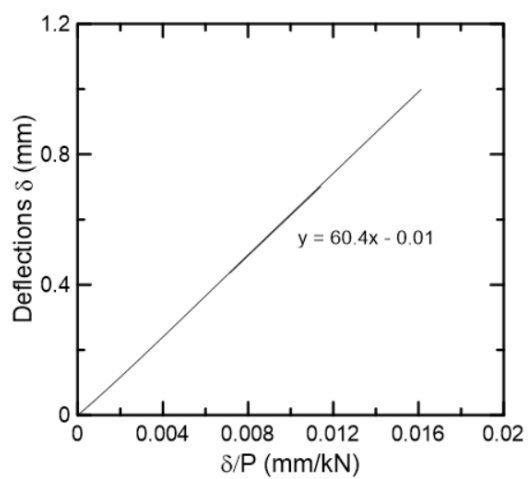
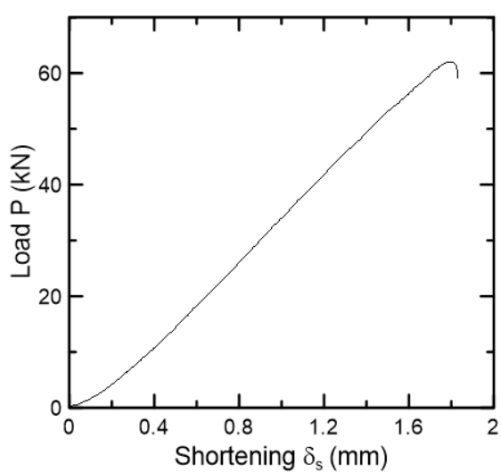
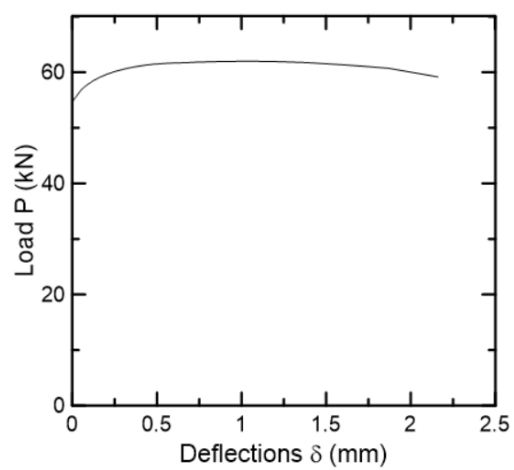


PL.100.01

Date: September/2017

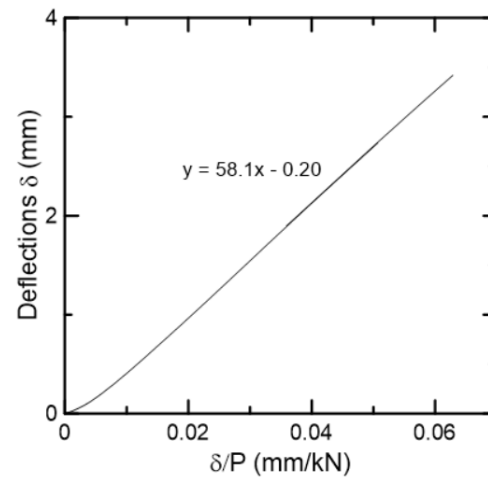
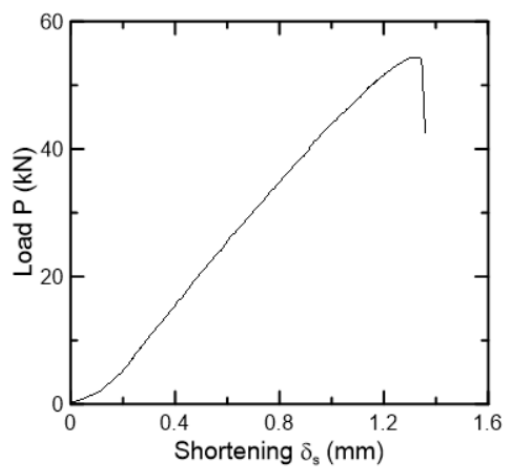
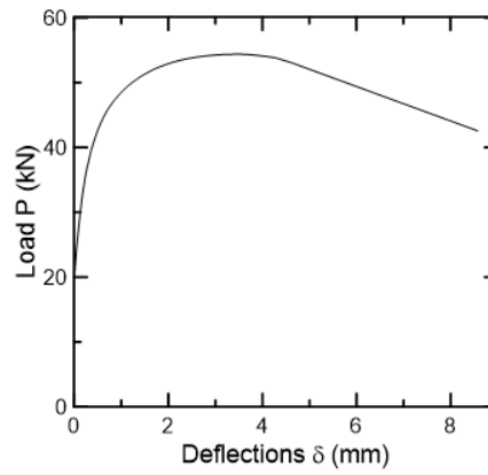
P_{max} : 62.0 kN

δ_0 : 0.01 mm



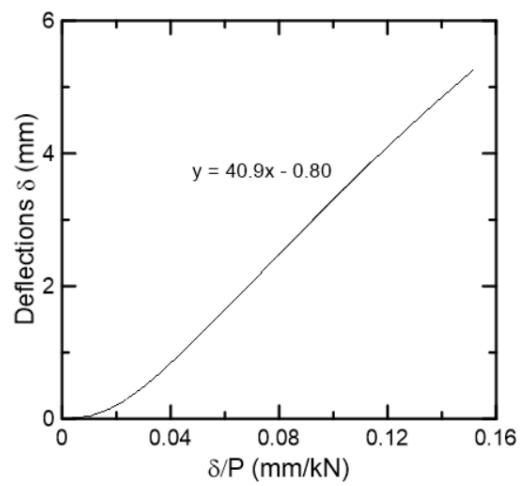
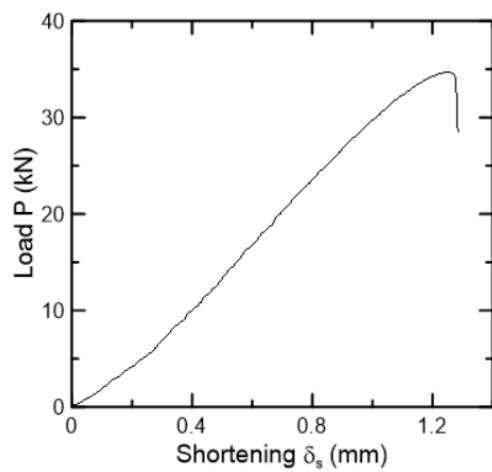
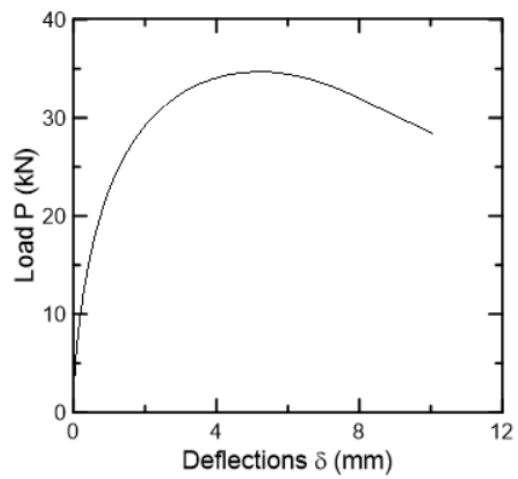
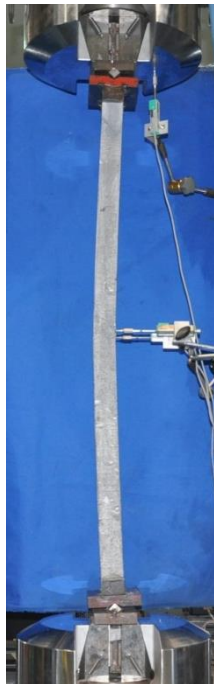
PL.100.02

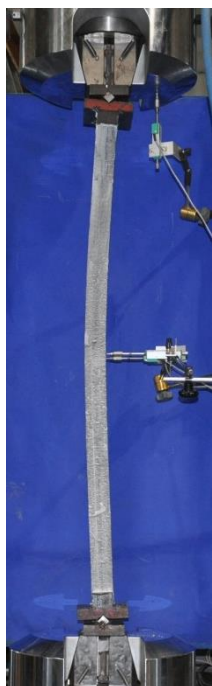
Date: September/2017

 P_{max} : 54.4 kN δ_0 : 0.20 mm

PL.120.01

Date: September/2017

 P_{max} : 34.7 kN δ_0 : 0.80 mm

PL.120.02

Date: October/2017

P_{max} : 43.6 kN

δ_0 : 0.01 mm

